Proximity Superconductivity in Indium Arsenide Two-Dimensional Electron Gas Devices

by

Fiona Thompson

A thesis
presented to the University of Waterloo
in fulfillment of the
thesis requirement for the degree of
Master of Science
in
Chemistry (Quantum Information)

Waterloo, Ontario, Canada, 2024

© Fiona Thompson 2024

Author's Declaration

This thesis consists of material all of which I authored or co-authored: see Statement of Contributions included in the thesis. This is a true copy of the thesis, including any required final revisions, as accepted by my examiners.

I understand that my thesis may be made electronically available to the public.

Statement of Contributions

This thesis was written in its entirety by Fiona Thompson. This thesis consists of original contributions by Fiona Thompson, with the following exceptions:

- Sections 4.2 and 5.2 include results and figures from the paper, High transparency induced superconductivity in field effect two-dimensional electron gases in undoped InAs/AlGaSb surface quantum wells [18] and its associated supplementary information. My contributions to this paper were obtaining many of the cryostat and dilution refrigerator measurements, producing multiple figures, and performing statistical analysis. This paper was an extremely collaborative effort; co-authors Annelise Bergeron, Francois Sfigakis, and Ahmed Elbaroudy are responsible for much of the project ideation, fabrication, measurements, and data analysis presented in these sections. A more detailed list of authors' contributions may be found in the paper. Section 4.2 additionally includes results presented here for the first time.

Abstract

Of the many theoretical proposals for quantum computers, topological quantum computing is unique in its resistance to decoherence and the reliability of its gate operations. One proposed method for achieving these topological qubits is to harness the unusual non-Abelian exchange statistics of quasiparticle excitations known as Majorana bound states. Historically, research devoted to realizing these states has primarily been in nanowires, but purely one-dimensional devices are limited in their applications. Two-dimensional electron gas devices are an alternative with the benefit of future scalability and increased options for device geometries. To this end, we developed InAs/AlGaSb surface quantum well devices compatible with the proximity-induced superconductivity required to realize a Majorana device.

Magnetotransport measurements investigating mobility-density relationships, I-V characteristics, the Shubnikov de Haas effect, and the quantum Hall effect confirm the very high quality of our dielectric deposition method and growths. Even with quantum wells so near the surface of the device, we achieve high mobilities and stable, reproducible gating characteristics. These devices have high spin-orbit coupling coefficients, confirming that we can simultaneously benefit from the inherent bulk properties of InAs and properties imparted by the rest of the growth and lithography steps. Analytical comparisons of devices with different quantum well widths, interface characters, and dielectric deposition methods reinforce the need for the rigorous optimization of numerous factors. From this analysis, we conclude that devices with smooth surface morphologies, SiO_2 dielectric deposited by atomic layer deposition, and InSb-like interfaces provide the ingredients necessary to achieve near-record mobilities and consistent gating properties.

On these same excellent wafers, we fabricated superconductor-normal-superconductor (SNS)-type devices of three different normal region dimensions with ex-situ deposited niobium as the proximitizing superconductor. The universally high quality of these devices challenges the long-held norm that epitaxial aluminum is the best choice for the superconductor in these types of devices. Specifically, we achieved figures of merit much higher than those previously reported in Nb-InAs-Nb devices and on par with those using epitaxial aluminum. Using two separate mathematical models, we found that our devices have very high transparencies, indicating high-quality interfaces. Detailed plans for future devices are also discussed in this thesis, including gated SNS devices, quantum point contacts, and an attempt at observing Majorana signatures.

Acknowledgements

So many people share the credit for the success of this work. My colleagues in and out of the laboratory were invaluable assets throughout my degree, and I owe them all acknowledgements. I would like to begin by thanking my supervisor, Jonathan Baugh, and the co-investigator on the Majorana Project, Zbig Wasilewski, for their leadership, support, and belief in this project! I would also like to thank Adam Wei Tsen for being a valuable member of my committee and for encouraging me to challenge myself. I am also so thankful to the other members of this project: Ahmed Elbaroudy, Andrew Jordan, Peyton Shi, and especially Annelise Bergeron, who spearheaded so much of this work and was such a great mentor. Thank you to George Nichols and the QNC and RAC cleanroom laboratory staff for their support and patience. I would also like to thank Laura Ingram, Sue Stathopulos, and John Donohue for fostering my teaching skills and giving me so many amazing opportunities throughout my degree. Perhaps my most significant professional "thank you" goes to Franois Sfigakis, without whom no part of this work could have happened. If I ended this degree having absorbed even a tiny fraction of your knowledge, work ethic, or tolerance, my time here was worthwhile.

On a personal note, thank you so much to my friends and family! Special acknowledgement goes to Bobbi Rotolo for always providing a comfortable space and a home-cooked meal when needed. To Jack deGooyer, whose daily presence in my life is the greatest gift Waterloo and IQC could have given me: thank you for always being my biggest cheerleader. Finally, my parents, Zac and Cara, are owed the ultimate acknowledgements for somehow raising me into someone capable of writing a master's thesis. I cant believe you pulled that off.

Dedication

This work is dedicated to my beloved cat, Keir, who cannot read.

Table of Contents

Author's Declaration ii

Statement of Contributions iii

Abstract iv

Acknowledgements v

Dedication vi

List of Figures xi

List of Tables xvii

Acronyms xviii

1 Introduction 1

1.1 Majorana Origins 1

1.2 Majorana Bound States 3

1.3 The Kitaev Chain 4

1.4 Topological Qubits 6

1.5 The Ingredients 8

1.5.1 Proximity-Induced Superconductivity 8

1.5.2 Axially-Applied Zeeman Field . . . 10
1.5.3 Spin-Orbit Coupling . . . 11
1.5.4 Theoretical Device Designs . . . 12
1.6 Majorana Signatures . . . 14
1.6.1 Zero Bias Conductance Peaks . . . 14
1.6.2 Other Signatures . . . 16
1.6.3 Braiding Experiments . . . 17
1.7 Josephson Junctions . . . 18
1.8 Indium Arsenide and Indium Antimonide . . . 20

2 2DEG Quantum Well Devices from the Bottom-Up 23
2.1 Introduction . . . 23
2.2 Epitaxial Growth . . . 25
2.2.1 Substrate . . . 25
2.2.2 Buffer . . . 27
2.2.3 Bottom Barrier . . . 27
2.2.4 Interface . . . 28
2.2.5 Quantum Well . . . 28
2.2.6 Cap Layer . . . 29
2.3 Nanofabrication . . . 29
2.3.1 Mesa . . . 30
2.3.2 Ohmic Contacts . . . 31
2.3.3 Gate Dielectric & Vias . . . 32
2.3.4 Top Gate and Bond Pads . . . 33
2.3.5 Superconducting Devices . . . 35
2.3.6 Sulphur Passivation . . . 36

3 Characterization **38**

3.1 Measurement Apparatuses . . . 38

3.1.1 Cryostat . . . 38

3.1.2 Dilution Refrigerator . . . 38

3.1.3 Electronic Setups . . . 40

3.2 Magnetotransport . . . 40

3.2.1 Hall Effect, Mobility, and Density . . . 40

3.2.2 Landau Levels & the Shubnikov-de Haas Effect . . . 42

3.2.3 Weak Anti-Localization . . . 45

3.3 Superconductivity . . . 47

3.3.1 Multiple Andreev Reflections . . . 47

3.3.2 Transparency . . . 48

3.3.3 Hard and Soft Gaps . . . 48

4 Two-dimensional electron gases in InAs/AlGaSb surface quantum wells **50**

4.1 Introduction . . . 50

4.2 24 nm Quantum Wells . . . 51

4.2.1 Optimizing the Gate Dielectric . . . 51

4.2.2 Magnetotransport of G743 & G782 . . . 58

4.3 15 nm Quantum Wells . . . 61

5 Proximitized superconducting devices on InAs/AlGaSb surface quantum wells **66**

5.1 Introduction . . . 66

5.2 Ungated SNS Devices . . . 67

5.3 Gated SNS Devices . . . 75

5.4 Quantum Point Contacts . . . 75

6 Fraunhofer Diffraction Patterns **79**
6.1 Introduction . . . 79
6.2 Interpretation . . . 82
6.2.1 Sources of Anomalous Fraunhofer Patterns . . . 83
6.2.2 In Pursuit of Majorana Bound States . . . 84
6.3 Simulations . . . 85
6.4 Measurements . . . 92

7 Outlook & Conclusion **94**
7.1 Majorana Devices . . . 94
7.2 Other Applications . . . 95
7.3 Conclusions . . . 95

Letters of Copyright Permission **96**

References **102**

APPENDICES **121**

A Code **122**
A.1 Weak anti-localization fits . . . 122
A.1.1 HLN model . . . 122
A.1.2 ILP model . . . 124
A.2 Fraunhofer simulations . . . 127

List of Figures

1.1 The Kitaev chain. 5

1.2 The trivial phase. 5

1.3 The topological phase. 5

1.4 A depiction of the exchange of two MBSs in a nanowire with a junction. A *braid* is visible in the centre, representing the unitary operation U_{23}. 7

1.5 Andreev reflection. It is worth noting that this process can also be reversed, i.e. a hole incident on the interface will be converted into a Cooper pair and a retroreflected electron. 9

1.6 Simplified representation of a conductance band diagram with structural inversion symmetry (left) vs asymmetry (right). SIA may also arise from asymmetrical doping. 11

1.7 Simple conduction band diagrams for electrons in a nanowire at each stage of the "recipe:" (a) With proximity superconductivity, (b) and with SOC, and (c) and with an external perpendicular Zeeman field. Reproduced from [128] with permission from Springer Nature. 12

1.8 Our Majorana device design based on the work of Hell et al. [65] 14

1.9 A planar Josephson junction device of the type measured later in this thesis. The semiconducting region between the two superconducting electrodes is made superconducting via the proximity effect. 19

1.10 The bandgaps and lattice constants of some common elemental and compound semiconductors. Reproduced from [110] with permission from Springer Nature. 21

2.1 Generic conduction bandstructure for a surface quantum well with a cap layer designed for proximity effect applications. The dotted horizontal line represents the Fermi level. The 2DEG wavefunction is not entirely confined to the QW; it is also partially localized in the cap layer. The extent of this wavefunction penetration depends on the well's size and the materials of its neighbouring layers. 24

2.2 The layout file of a gated Hall bar device after only the mesa is patterned. Crosses are used as alignment marks, and arrows are used to ensure the sample remains upright. 30

2.3 The layout file of a gated Hall bar device after the mesa and the ohmic contacts are patterned. 32

2.4 The layout file of a gated Hall bar device after the mesa, ohmic contacts, and vias are patterned. 33

2.5 The layout file of a gated Hall bar device after the mesa, ohmic contacts, vias, top gate (black), and bond pads (light green) are patterned. 34

2.6 Schematic of (a) metal deposition procedure for ungated SNS devices, and (b) metal deposition procedure for future superconducting devices. 35

3.1 Phase diagram of a liquid helium mixture. Dilution refrigerator cooling occurs in the phase separation region. Reproduced from [76] with permission from Springer Nature. 39

3.2 Typical measurement setups on a Hall bar geometry. The magnetic field is applied out of the plane of the images. (a) Constant current (100 nA) 4-terminal circuit setup for measuring Hall density and mobility. (b) Constant voltage (100 μV) 4-terminal circuit setup for measuring pinch-off characteristics. Triangles represent current/voltage pre-amplifiers whose voltage output is fed into an SR-830 lock-in (not shown). Reproduced from [18] with permission from AIP Publishing. 41

3.3 Data from our group's previous publication on InSb surface quantum wells. (a) Well-quantized Hall plateaus and clear SdH oscillations reaching zero at filling factors $\nu = 4, 3, 2, 1$ at $n_{2D} = 3.4 \times 10^{11}$ cm^{-2}. (b) Landau fan diagram: a magnetic field sweep measuring longitudinal resistivity at each gate voltage. Reproduced from [19] with permission from AIP Publishing. . 45

3.4 A qualitative comparison between a hard superconducting gap (red) and a soft superconducting gap (blue). Based on a figure from Reference [32] and experimental data from Reference [79]. 49

4.1 Pinch-off curves at 100 μV ac excitation for gated Hall bars with gate dielectrics (a) SiO_2 and (b) HfO_2. Four traces in each direction are shown in (a), while two in each direction are shown in (b). Reproduced from [18] with permission from AIP Publishing. 52

4.2 Hall density vs top gate voltage (a,b) and mobility vs 2DEG density (c,d) of devices fabricated with SiO_2. Reproduced from [18] with permission from AIP Publishing. 53

4.3 Hall density vs top gate voltage (a,b) and mobility vs 2DEG density (c,d) of devices fabricated with HfO_2. Reproduced from [18] with permission from AIP Publishing. 54

4.4 Mobility vs 2DEG density of gated Hall bars at 1.6 K on (a) G782, comparing ALD processes using HfO_2 and SiO_2 and (b) G837, comparing the ALD process using HfO_2 and the SiO_2 deposited with the PCVD process at 300°C. 56

4.5 Four-terminal pinch-off curve for G837PCVDTGHBC8. Four sweeps "up" (from -20 to 0 V) are shown in orange. Four sweeps "down" (from 0 to -20 V) are shown in blue. 56

4.6 (a) SdH and quantum Hall measurements at $V_g = -10.0$ V ($n_{2D} = 1.6 \times 10^{12}$ cm^{-2}) on G837PCVDTGHBC8. Note the very small range of the oscillations (0.01 kΩ/sq.) and the lack of quantized Hall plateaus. 57

4.7 (a) SdH oscillations and quantum Hall plateaus at $V_g = -8.0$ V ($n_{2D} = 8.57 \times 10^{11}$ cm^{-2}); (b) Landau fan of SdH oscillations. The indicated filling factors were calculated from the Hall resistance. The dashed white lines indicate where the second subband populates the 2DEG. Reproduced from [18] with permission from AIP Publishing. 58

4.8 (a) Experimental WAL data (orange) fit to the ILP model (black). The 2DEG density ($\times 10^{12}$ cm^{-2}) for each plot is shown in the upper right. (b) Spin-orbit coefficient, extracted from both the HLN and ILP models, as a function of n_{2D}. The dotted line is where second-subband occupation is suspected to begin. Reproduced from [18] with permission from AIP Publishing. 59

4.9 Our experimental WAL data compared to other values across the literature. Reproduced from [18] with permission from AIP Publishing. 60

4.10 Pinch-off curve for G1120TG1C3. Three sweeps "up" (from -9 to -5 V) are shown in orange. Three sweeps "down" (from -5 to -9 V) are shown in blue. 62

4.11 (a) Hall density vs top gate voltage and (b) mobility vs 2DEG density of all Hall bars at 1.6 K. C3 is the sample that was selected for further measurements on the dilution fridge. 63

4.12 (a) Hall density vs top gate voltage and (b) mobility vs 2DEG density of device G1120TG1C3 at 22 mK. The mobility peak in (b) is 2.11×10^4 cm^2/Vs at 0.849×10^{12}/cm^2. 64

4.13 SdH oscillations and quantum Hall plateaus for device G1120TG1C3 at $Vg = -4.1$ V, corresponding to $n_{2D} = 0.908 \times 10^{12}$/cm^2. Measurements taken at 1.6 K. 65

5.1 Four-terminal measurement setup for ungated SNS devices. The length L and width W are labelled. Adapted from [18] with permission from AIP Publishing. 68

5.2 Data at 15 mK for devices: (a)-(b) SNS-1, (c)-(d) SNS-2, and (e)-(f) SNS-3. All panels on the left show DC four-terminal I-V traces of SNS junctions. All panels on the right show normalized AC four-terminal differential conductance dI/dV and MAR peaks. Reproduced from [18] with permission from AIP Publishing. 70

5.3 Data at 15 mK for devices: (a)-(b) SNS-4, (c)-(d) SNS-5, and (e)-(f) SNS-6. All panels on the left show DC four-terminal I-V traces of SNS junctions. All panels on the right show normalized AC four-terminal differential conductance dI/dV and MAR peaks. Reproduced from [18] with permission from AIP Publishing. 71

5.4 Fig. 5.3(b) with position of MAR peaks shown. Reproduced from [18] with permission from AIP Publishing. 72

5.5 MAR peak positions (red circles) fit to $V_n = 2\Delta_{MAR}/e_n$, with individual fits (dashed lines) shown for the device: (a) SNS-1, (b) SNS-2, (c) SNS-3, (d) SNS-4, (e) SNS-5, and (f) SNS-6. The fit analysis determines the respective Δ_{MAR}. Reproduced from [18] with permission from AIP Publishing. 73

5.6 Temperature dependence of the critical current in SNS-1. The data was fit to multiple $\mathcal{T}$ (transparencies) to determine the most accurate value. Reproduced from [18] with permission from AIP Publishing. 74

5.7 Schematic of the planned QPC devices. Not to scale. The width W and length L of the QPC are indicated in the figure. 76

5.8 Simulation of the saddle-shape of the electrostatic potential V (here, U) in a GaAs/AlGaAs QPC with $L = 200$ nm and $W = 350$ nm. Reproduced from [74] with permission from AIP Publishing. 77

5.9 The dependence of the conductance through a QPC on $(E - V_0)/\hbar\omega_x$ at different values of ω_y/ω_x. The conductance is well-quantized at the larger values of ω_y/ω_x but decreases until there is no quantization when $\omega_y = 0$. Based on the work of Reference [26]. 78

6.1 A comparison of the Fraunhofer-like JJ pattern in Equation 6.2 (blue) and the true Fraunhofer curve in Equation 6.5 (red). 80

6.2 A JJ with insulating barrier of length L, width W, and thickness t. Here, the magnetic field is represented by H. Reproduced from [38] under Creative Commons license. 81

6.3 Superconducting quantum interference (SQI) measurements where (a) the Fermi level is in one of the bulk bands, (c) the Fermi level is in the topological gap, and (e) the Fermi level is in the valence band. Reproduced from [126] with permission from Springer Nature. 85

6.4 The SNS device with a correction to the effective magnetic field, or effective area of the normal region. The red dotted area represents the flux-focusing correction proposed in Reference [11]. 87

6.5 Simulation of the Fraunhofer diffraction pattern for SNS-1 and SNS-2 with various adjustments: (1) with $d = L + 2\lambda$; (2) with $d = L + 2\lambda_z$; and (3) with $A = A_{eff}$. 89

6.6 Simulation of the Fraunhofer diffraction pattern for SNS-3 and SNS-4 with various adjustments: (1) with $d = L + 2\lambda$; (2) with $d = L + 2\lambda_z$; and (3) with $A = A_{eff}$. 90

6.7 Simulation of the Fraunhofer diffraction pattern for SNS-5 and SNS-6 with various adjustments: (1) with $d = L + 2\lambda$; (2) with $d = L + 2\lambda_z$; and (3) with $A = A_{eff}$. 91

6.8 Measured dependence of V_{sd} versus V_{ac} on magnetic field. 93

7.1 Reuse permission for Fig. 1.7. 97
7.2 Reuse permission for Fig. 1.10. 98
7.3 Reuse permission for Fig. 3.1. 99
7.4 Reuse permission for Figs. 3.2, 4.1, 4.2, 4.3, 4.7, 4.8, 4.9, 5.1, 5.2, 5.3, 5.4, 5.5, & 5.6. 99
7.5 Reuse permission for Fig. 5.7. 100
7.6 Reuse permission for Fig. 6.3. 101

List of Tables

1.1 Desirable material properties for Majorana devices and their respective values for bulk InAs and InSb. 22

4.1 Summary of wafers with 24 nm wide InAs SQWs. 51

4.2 Mobilities at $V_g = 0$ V and peak mobilities for various gated Hall bars. All measurements were taken at 1.6 K. 55

4.3 Summary of wafers with 15 nm wide InAs SQWs. 61

4.4 Mobilities measured on ungated Hall bars and one gated Hall bar on G1120 at $V_g = 0$. All measurements were taken at 1.6 K. 62

4.5 Peak mobilities measured on gated Hall bars at 1.6 K. 63

5.1 List of wafer properties used to determine the regimes of each device. . . . 67

5.2 List of SNS devices, and their dimensions and measured properties. $\mathcal{T}$, the transparency, for each device was calculated using the OTBK model. . . . 68

5.3 Planned dimensions of QPC devices. 75

6.1 Constants used for Fraunhofer simulations. Values sourced from [124] (rows 1-4) or calculated (rows 5-8). 88

6.2 Periodicity of the Fraunhofer pattern for each device geometry under each adjustment; accurate to two decimal places. 88

Acronyms

1D one-dimensional. 4, 13, 14, 16, 18, 20, 23, 94

2D two-dimensional. 3, 18, 23, 24

2DEG two-dimensional electron gas. xii–xiv, 11, 14, 23, 24, 27–29, 34, 41–44, 50, 51, 53–56, 58–64, 95

ABS Andreev bound state. 15, 16, 83

ALD atomic layer deposition. xiii, 33, 51, 55, 56, 58, 62

BCS Bardeen, Cooper, and Schrieffer. 8

BOE buffered oxide etch. 30, 36

FET field-effect transistor. 95

FQH fractional quantum Hall. 7, 17

HLN Hikami-Larkin-Nagaoka. 46, 59, 60

ILP Iordanskii-Lyanda-Geller-Pikus. 46, 59, 60

JJ Josephson junction. xv, 18, 19, 75, 79–86, 95

MAR multiple Andreev reflections. xiv, 47, 48, 67, 68, 72

MBE molecular beam epitaxy. 25, 26, 28, 51, 61

MBS Majorana bound state. xi, 3, 4, 6–8, 10, 12, 13, 15–18, 20, 22, 24, 47, 83–85, 94

MD misfit dislocation. 26, 27

MISFET metal-insulator-semiconductor field-effect transistor. 95

MOSFET metal-oxide-semiconductor field-effect transistor. 95

MZM Majorana zero mode. 3

PCVD plasma-activated chemical vapour deposition. xiii, 55, 56

PVD physical vapour deposition. 31

QD quantum dot. 7

QEC quantum error correction. 6

QHE quantum Hall effect. 43, 44

QPC quantum point contact. xv, xvii, 75–78, 96

QW quantum well. xii, 11, 23, 24, 27–29, 59–62, 64

SdH Shubnikov-de Haas. xii–xiv, 44, 45, 55, 57–59, 64, 65

SIA structural inversion asymmetry. 11, 60

SIS superconductor-insulator-superconductor. 80, 84

SMU source measure unit. 40

SNS superconductor-normal-superconductor. xv, 14, 29, 47, 66–68, 75, 79, 84, 87, 95, 96

SOC spin-orbit coupling. xi, 11–13, 15, 20–22, 46, 47, 60, 83–85

SQI superconducting quantum interference. xv, 84, 85

SQUID superconducting quantum interference device. 13, 18, 84

SQW surface quantum well. xvii, 23, 28, 50, 51, 61, 75, 95

TD threading dislocation. 26, 27

TGP topological gap protocol. 94, 95

TI topological insulator. 24, 84

UHV ultra-high vacuum. 25, 37

WAL weak anti-localization. xiv, 46, 59, 60, 64

WL weak localization. 45, 46

ZBCP zero-bias conductance peak. 14–17, 21, 47, 76, 94

Chapter 1

Introduction

1.1 Majorana Origins

The story of quantum mechanics is one of both monumental successes and seemingly insurmountable challenges. After a period of slow progress, a "quantum revolution" began in the early twentieth century, launching a field of research that would redefine our understanding of physics. Armed with knowledge of classical and statistical mechanics, physicists began developing models of quantum phenomena, writing a "rule book for the microscopic world."[1] One of these seminal models was published by Paul Dirac, a British physicist, in 1928. He derived the Dirac equation, a concise and relativistic representation of the parity symmetry of spin-1/2 particles [40].

Dirac's publication threatened to slow the momentum of the quantum revolution. Initially, the equation's implication that negative energy states are accessible to electrons was problematic for scientists working in the field; according to Werner Heisenberg, "Dirac's paper threw [them] out into the open sea again" [64] after a period of rapid development in quantum theory. Dirac addressed this dilemma by proposing that the vacancies in the negative energy states behaved like spin-1/2, positively charged particles with masses identical to electrons. Experimental observations of these "anti-electrons," now commonly referred to as "positrons," were made by Carl David Anderson in 1932 [7] and resulted in him winning the Nobel Prize in Physics in 1936. Though the Dirac equation has many important implications, this theory of a matter-antimatter relationship is the remarkable idea that established the work presented in this thesis.

[1] This conception of quantum mechanics is one I learned from John Donohue, the outreach coordinator at the Institute for Quantum Computing.

In 1937, theoretical physicist Ettore Majorana encountered a mathematical curiosity based on Dirac's work. The original equation involved complex numbers, but Majorana wondered if they were necessary or only the result of basing the model on electron behaviour. Indeed, Majorana discovered that this need not be the case and that it was possible to write a purely real spin-1/2 relativistic wave equation [99]. The Dirac equation for a free particle may be written as follows [166]:

$$(i\gamma^{\mu}\delta_{\mu} - m)\psi = 0 \tag{1.1}$$

where m is the mass of the particle, ψ is its particle field, $\mu = 0, 1, 2, 3$, δ_{μ} is the four-gradient, and γ^{μ} are four 4×4 matrices that obey the following relationship (governed by Clifford algebra) [166]:

$$(\gamma^0)^2 = -(\gamma^1)^2 = -(\gamma^2)^2 = -(\gamma^3)^2 = 1 \tag{1.2}$$

In Dirac's mathematical representation, ψ must, unsurprisingly, be complex; a complex field is required to describe charged particles. The matrices γ^{μ} contain both real and imaginary entries. Majorana wondered if an uncharged particle – one with a real field – could still be described by the Dirac equation. He determined that the following purely imaginary γ^{μ} could reflect such a system [166]:

$$\tilde{\gamma}^0 = \sigma_y \otimes \sigma_x \tag{1.3}$$

$$\tilde{\gamma}^1 = i\sigma_x \otimes I \tag{1.4}$$

$$\tilde{\gamma}^2 = i\sigma_z \otimes I \tag{1.5}$$

$$\tilde{\gamma}^3 = i\sigma_y \otimes \sigma_y \tag{1.6}$$

where σ_x, σ_y, and σ_z are the Pauli matrices. This leads to the following representation of the Majorana equation:

$$(i\tilde{\gamma}^{\mu}\delta_{\mu} - m)\tilde{\psi} = 0 \tag{1.7}$$

where $\tilde{\psi}$ is real. The physical implication is a fundamental, uncharged particle that is its own antiparticle. The practical applications of this result were not immediately apparent; Majorana hypothesized that neutrinos might fit the theory given their lack of charge, but this was a purely speculative suggestion [99].

To date, the potential existence of the Majorana fermion remains mysterious. Majorana's neutrino suggestion remains a topic of research nearly a century later, as neutrinos' minuscule masses make them very difficult to detect, let alone study their behaviour. To conclusively classify two particles as a particle-antiparticle pair, they must collide, resulting

in their annihilation and creating other energetic particles like photons, mesons, or bosons. "Neutrinoless double-β decay," the phenomenon by which two antineutrinos annihilate each other, would be the unmistakable evidence that neutrinos are Majorana particles [9]. Scientists have yet to observe this unique type of decay. Until then, or until another hallmark of Majorana behaviour arises, Majorana's original question remains open.

1.2 Majorana Bound States

Though the Majorana fermion remains elusive, Majorana's ideas are increasingly crucial to condensed matter physics [166]. When quasiparticles – collective excitations with particle-like properties – arise in superconductors, they are often called "Bogoliubov quasiparticles." Nikolay Bogoliubov, whose name the quasiparticles bear, was a mathematician and theoretical physicist whose theories about electron-lattice interactions underpin much of the modern understanding of superconductivity [23]. These quasiparticles have many interesting properties, the most noteworthy of which is that they can annihilate each other, meaning they are their own antiparticles. Additionally, much like how the Majorana equation is a real representation of the Dirac equation, the Bogoliubov-de Gennes wave equation representing these quasiparticles can similarly be written in a real form [137]. This analysis led to a natural conclusion: Bogoliubov quasiparticles are Majorana fermions, in the sense that they are spin-1/2 excitations with fermionic statistics [15].

Bogoliubov quasiparticles are only the beginning of Majorana's importance to superconductivity. Majorana bound states (MBSs), also known as Majorana zero modes (MZMs), are quasiparticle excitations at zero energy and are also his namesake. MBSs fall under the "anyon" umbrella: quasiparticles arising in two-dimensional (2D) systems that obey neither fermionic nor bosonic statistics [36]. Specifically, these quasiparticles exhibit non-Abelian statistics, meaning that physically exchanging the position of two identical MBSs results in a fundamentally different quantum state [153]. As the "Majorana" title implies, MBS operators are entirely real [36].

It is useful to represent these exchange statistics mathematically and to compare them to bosonic or fermionic exchanges, which follow Abelian statistics, where particle exchange only imparts a phase difference:

$$|\Psi\rangle \rightarrow \pm |\Psi\rangle \tag{1.8}$$

Majorana operators may be represented as pairs ("half-fermions") to form fermionic modes, where the fermionic creation and annihilation operators can be defined as:

$$c_n^\dagger = \frac{1}{2}(\gamma_{2n-1} + i\gamma_{2n}) \tag{1.9}$$

$$c_n = \frac{1}{2}(\gamma_{2n-1} - i\gamma_{2n}) \tag{1.10}$$

In the adiabatic limit, two Majoranas can be exchanged without the wavefunction leaving the ground state manifold of $|\Psi\rangle$. For N pairs of Majoranas (or N fermions), the ground state manifold has 2^N states. The following represents the exchange of two Majoranas γ_n and γ_m [3]:

$$|\Psi\rangle \to U_{nm} |\Psi\rangle \tag{1.11}$$

where U_{nm} is a $2^N \times 2^N$ unitary matrix with the form

$$U_{nm} = e^{\pm\frac{\pi}{4}\gamma_n\gamma_m} = \frac{1}{\sqrt{2}}(1 \pm \gamma_n\gamma_m). \tag{1.12}$$

For example, for a clockwise exchange of two Majoranas γ_2 and γ_3 with initial quantum state $|00\rangle$,

$$|00\rangle \to U_{23} |00\rangle = \frac{1}{\sqrt{2}}(|00\rangle - i |11\rangle). \tag{1.13}$$

Importantly, these matrices U_{nm} are non-commutative [3]:

$$U_{23}U_{12} \neq U_{12}U_{23} \tag{1.14}$$

1.3 The Kitaev Chain

Toy models help develop an understanding of how to practically generate unpaired, exchangeable MBSs in the laboratory. In 2000, the physicist Alexei Kitaev conceptualized a quasi-one-dimensional (1D) "quantum wire" of electrons atop a superconductor [86]. Kitaev admits his model is "rather unrealistic"; not only does it assume only one spin direction, but it requires breaking electric charge conservation, likely requiring a p-wave (triplet) superconductor. Under these exceptional circumstances, he explains the two possible ways to "pair" the Majorana operators: those from the same or adjacent sites. In the latter case, an unpaired MBS at zero energy would arise at each end of the wire. An additional requirement unique to the second case is the presence of a gapped bulk excitation spectrum; there must be a superconducting gap. Kitaev does speculate about possible physical realizations of this set of properties, mentioning both spin-orbit interaction and a strong magnetic field to separate particles with opposite spins [103]. While only a couple of lines were devoted to these ideas in his original paper, later research reveals the prescience of Kitaev's work.

The Hamiltonian for a chain consisting of $L \gg 1$ electrons, in terms of Majorana operators, is as follows:

$$H = \frac{i}{2} \sum_{n} \left[-\mu \gamma_{2n-1} \gamma_{2n} + (w + |\Delta|) \gamma_{2n} \gamma_{2n+1} + (-w + |\Delta|) \gamma_{2n-1} \gamma_{2n+2} \right] \tag{1.15}$$

where w is the hopping amplitude (the term related to the kinetic energy of particle tunnelling), μ is the chemical potential, and $\Delta = |\Delta| e^{i\theta}$ is the induced superconducting gap.

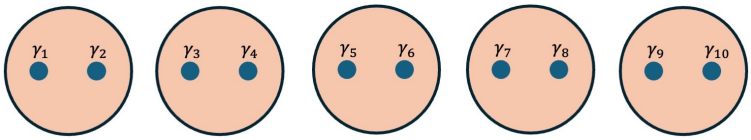


Figure 1.1: The Kitaev chain.

In the *trivial* case, Majoranas from the same site n are paired together. Here, $|\Delta| = w = 0$, $\mu < 0$:

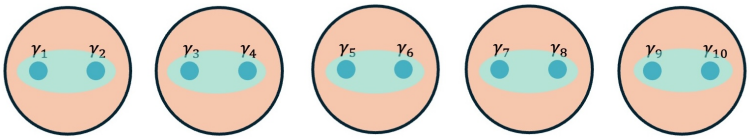


Figure 1.2: The trivial phase.

$$H = \frac{i}{2}(-\mu) \sum_{n} \gamma_{2n-1} \gamma_{2n} \tag{1.16}$$

In the *topological* case, Majoranas from adjacent sites are paired together. Here, $|\Delta| = w > 0$, $\mu = 0$:

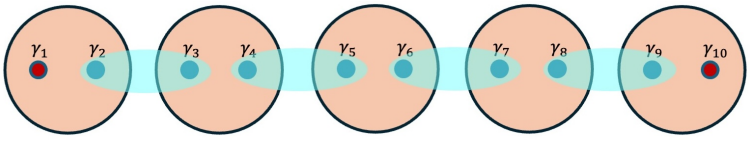


Figure 1.3: The topological phase.

$$H = iw \sum_n \gamma_{2n}\gamma_{2n+1} \tag{1.17}$$

Note that the operators corresponding to the unpaired Majoranas do not appear in this Hamiltonian; they are at zero energy. This state is protected by particle-hole symmetry and a lack of zero-energy excitations elsewhere in the wire and is robust until $|\mu| = 2w$, or until the gap closes.

1.4 Topological Qubits

In 1997, three years before the publication of his toy model, Kitaev made a tantalizing suggestion: scientists could use anyons to construct a quantum computer with inherent fault tolerance [85]. Decoherence, the loss of quantum information to the environment, remains a significant challenge when constructing quantum bits (qubits). Though qubit devices theoretically promise to perform more efficient and reliable computations than classical computers, the practical difficulty of isolating these systems from the environment hinders their potential [132]. In 1995, the first quantum error correction (QEC) code was introduced by Peter Shor, proving that it is indeed possible to protect qubits from decoherence at the algorithmic level [144]. Since then, QEC has seen many advances, but the progress of quantum technology limits this approach to achieving fault tolerance. Current qubit platforms cannot support the amount of QEC needed to eliminate the loss of quantum information to the environment [139]; thus, decoherence still imposes a ceiling on the computations we can perform. Pursuing other avenues toward fault tolerance remains valuable, and Kitaev's suggestion to use non-Abelian anyons to encode quantum information is a compelling option.

The statistical properties of MBSs render them tolerant to environmental perturbations. Exchanges of the type depicted in Fig. 1.4 form representations of the braid group, a class of topological objects depicted as intertwining strands with fixed endpoints [161]. The exchange process can store quantum information nonlocally by "braiding" non-Abelian anyons. Recall that the adiabatic exchange of two MBSs results in a fundamentally different quantum state. The quantum information encoded in the braid is inaccessible to and unaffected by local perturbations and measurements [60]. Additionally, the operations performed via exchange are independent of trajectory or time, allowing for reliable measurements [3].

Unfortunately, topological qubits – like those harnessing the non-Abelian statistics of MBSs – are certainly not without their obstacles. Despite their resistance to decoherence,

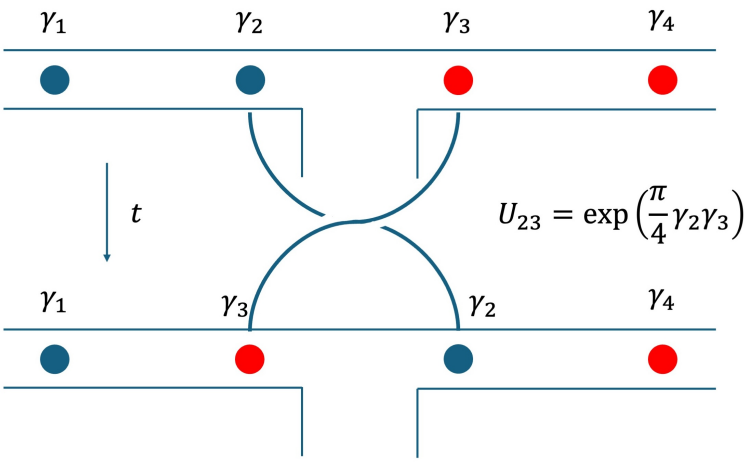


Figure 1.4: A depiction of the exchange of two MBSs in a nanowire with a junction. A *braid* is visible in the centre, representing the unitary operation U_{23}.

they are not entirely immune to errors [2]; for example, quasiparticle poisoning, where a stray electron enters the system and flips its fermion parity, challenges information protection and the ability to make accurate measurements [81]. Additionally, Majorana-based qubit operations are not universal for quantum computation. While braiding MBSs can allow many gate operations, non-topological phase gates are needed to augment these operations to achieve universality [176].

Charge parity readouts are the primary method proposed for measuring these topological operations. In the example depicted in Fig. 1.4, the measurement would be performed by combining MBSs and conducting a local measurement, interpreting the fermion charge parity as the qubit's basis states [36]. However, this action directly threatens the state's stability; performing a local measurement means that the quantum information is no longer topologically protected. Other potential methods to create topological qubits, such as vortices in cold atom superfluids [154] or measurement-only schemes using ν=5/2 fractional quantum Hall (FQH) states [24], may eliminate this challenge but introduce many of their own. One exciting proposal involves a hybrid quantum dot (QD)-Majorana architecture wherein controlling the QD can enact a controlled-NOT gate [173]. If scientists and engineers can extend this premise to other quantum circuits, similar structures could perform universal quantum computation while retaining some benefits of a purely topological qubit. While this thesis mainly focuses on semiconductor-superconductor heterostructures, many other topological quantum computing approaches deserve analysis and attention.

1.5 The Ingredients

Despite Kitaev's speculations about ways to physically realize MBSs, years passed before the publication of further proposals. The subject of this section is to explain the physical "ingredients" necessary and some of the theoretical "recipes" developed to create MBSs. This section follows the same logical progression set out in Reference [3].

1.5.1 Proximity-Induced Superconductivity

A *superconductor* is a material that conducts without resistance under a specific temperature (known as the critical temperature T_c). The first discovered superconductors in the 1910s were elemental (mercury, lead, and tin) [159]; however, in recent years, considerable research has been devoted to developing composite materials with higher critical temperatures. The mechanism of superconductivity was not fully elucidated until the publication of "Microscopic Theory of Superconductivity" in 1957 by Bardeen, Cooper, and Schrieffer. Their explanation, aptly referred to as "Bardeen, Cooper, and Schrieffer (BCS) theory", describes the pairing of electrons near the Fermi level into "Cooper pairs" via electron-phonon interactions in an ion lattice. In simple terms, these pairs – somewhat bosonic in nature and no longer needing to obey the Pauli exclusion principle – form a collective state akin to a Bose-Einstein condensate, all occupying the same ground state. This state is resistant to small excitations, leading to collective superconducting behaviour. A *superconducting gap* (Δ) appears as a consequence of the binding energy of Cooper pairs and their condensation to the ground state and is defined as the difference between the energy of the highest occupied and lowest unoccupied single-particle state [20].

Hybrid structures, or those that place a non-superconducting material in proximity with a superconducting metal, reveal some of the more interesting properties of Cooper pairs. Charge transfer at a normal-superconductor interface is mediated by *Andreev reflection* (see Fig. 1.5), where an electron in a normal metal incident on the interface is converted into a Cooper pair in the superconductor. A hole of identical wavevector is then retroreflected into the normal metal, conserving charge and momentum. In the opposite direction (though still mediated by Andreev reflection [160]), the *proximity effect* describes the phenomenon where supercurrent "leaks" into a neighbouring non-superconducting material and induces in it a superconducting gap [69]. The magnitude of this effect relies on numerous factors in superconductor-semiconductor heterostructures, including electron-electron and electron-phonon interactions in the semiconductor [145] and the transparency of the interface. The proximity effect is the same phenomenon responsible for Cooper pair tunnelling across a Josephson junction (see Section 1.7).

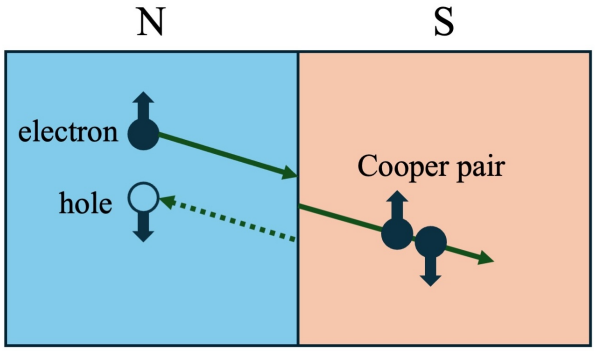


Figure 1.5: Andreev reflection. It is worth noting that this process can also be reversed, i.e. a hole incident on the interface will be converted into a Cooper pair and a retroreflected electron.

In the context of Majorana devices, proximity-induced superconductivity is required to create superconducting pairing while maintaining the necessary control and desirable qualities (as discussed later) afforded by using a semiconductor. Unfortunately, superconductivity alone does not create the adjacent pairing necessary for unpaired Majoranas. The Kitaev chain Hamiltonian (Equation 1.15) reveals the issue when written in momentum space [3]:

$$H = \left(\frac{k^2}{2m} - \mu\right)\tau_z + 2\Delta\tau_y \sin k \tag{1.18}$$

where k is momentum and τ are the Pauli matrices in the Nambu (particle-hole) basis. The superconducting pairing here is proportional to k, meaning it is momentum-dependent. In the original chain model, Kitaev suggested that p-wave superconductivity would address this issue [86]. In p-wave superconductors, electrons are paired in triplets with Cooper pair angular momentum $L = 1$, unlike the singlet pairing in the s-wave variety. As a concept, p-wave superconductivity is not new; Balian and Werthamer proposed the idea in 1963 to explain unique nuclear magnetic resonance shifts in paramagnetic species [12]. However, at the time of Kitaev's publication, the existence of p-wave superconductors had yet to be proven. More recent work suggests some iron-based superconductors demonstrate p-wave superconductivity [152], but they are certainly not commonplace. Until researchers found an alternative, realizing the Kitaev chain seemed impossible.

1.5.2 Axially-Applied Zeeman Field

Though Kitaev proposed using p-wave superconductivity as an avenue towards experimental realization, the actual Hamiltonian as written in Equation 1.18 is *spinless*. Real systems, however, are made up of electrons with definite spin. It is necessary to incorporate spin somehow, but it must be done carefully without introducing an extra spin degeneracy (Kramer's degeneracy) that would render the Majoranas unpaired.

In 2008, Fu and Kane proposed the first MBS device to address the superconductivity obstacle directly [51]. Instead of employing an elusive p-wave superconductor, Fu and Kane looked to something more "ordinary": s-wave superconductivity. While s-wave superconductivity is ordinary in the sense that it is more common in nature, proposing its use in an MBS device was a significant leap. The key to facilitating this unconventional use of s-wave superconductivity is a strong Zeeman field to orient the spins in a specific direction.

Mathematically, this Zeeman "trick" can be described as incorporating a Zeeman coupling term to the Hamiltonian such that $\mu < 0$ corresponds to spin-down particles and $\mu > 0$ corresponds to spin-up. Recall that the topological phase of the Kitaev chain is defined by $\mu > 0$ (see Section 1.3); therefore, the topological phase will only have spin-up species. This aligns well with the theoretical proposal of using a triplet-paired superconductor. The Hamiltonian is now

$$H = \left(\frac{k^2}{2m} - \mu - B\sigma_z\right)\tau_z + 2\Delta\tau_y k \tag{1.19}$$

where σ_z is the Pauli matrix. This Hamiltonian can be simplified further by acknowledging that the Zeeman field in an s-wave superconductor changes sign under time-reversal symmetry, meaning that it is independent of τ_z.

$$H = \left(\frac{k^2}{2m} - \mu\right)\tau_z + B\sigma_z + 2\Delta\tau_y k \tag{1.20}$$

This formulation also introduces a convenient definition for where the system is in the topological phase: $B^2 > \Delta^2 + \mu^2$. The magnitude of the Zeeman field required depends on the material's Landé g-factor, or how susceptible the spin degeneracy is to changes in the field. A larger g-factor means that a smaller B is necessary.

Though introducing the Zeeman field adds spin to the system while lifting Kramer's degeneracy, it alone does not achieve the effectively spinless system needed to create MBSs. In an s-wave superconductor, spin is conserved, and the introduction of the Zeeman field does not break this spin conservation; therefore, a system with proximity s-wave superconductivity and an applied Zeeman field cannot create spinless MBSs. Effectively, since

Majoranas cannot form, the Zeeman field has oriented the spins but destroyed the induced superconducting gap. Another phenomenon must be introduced to break spin degeneracy and reopen the gap: spin-orbit coupling.

1.5.3 Spin-Orbit Coupling

Spin-orbit coupling (SOC) describes the relativistic interaction between a particle's spin and orbital angular momentum as it moves around a nucleus. The Hamiltonian describing spin-orbit coupling, as derived from the Dirac equation for an electron with mass m and charge $-e < 0$ in an electric field $E(r) = \nabla\phi(r)$, is as follows [100]:

$$H_{SO} = \frac{e\hbar}{4m^2c^2}\hat{\sigma} \cdot \left[E\left(\overrightarrow{r}\right) \times \overrightarrow{P}\right] \tag{1.21}$$

In a non-centrosymmetric system, such as a III-V semiconductor 2DEG, some solutions to the Schrödinger equation will give allowed band structure energies that are products of spin and momentum terms [47]. This asymmetry leads to the Rashba effect:

$$H_{SO} = \alpha\sigma_y k \tag{1.22}$$

Specifically, the Rashba effect results from structural inversion asymmetry (SIA) (asymmetrical electron confinement; see Fig. 1.6), as opposed to the Dresselhaus effect arising from bulk inversion asymmetry. In other words, at high net electric fields across the QW (E_z), the degree of Rashba SOC should be high.

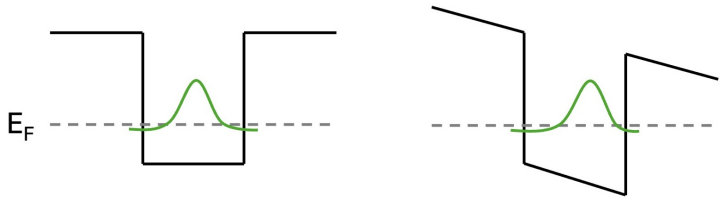


Figure 1.6: Simplified representation of a conductance band diagram with structural inversion symmetry (left) vs asymmetry (right). SIA may also arise from asymmetrical doping.

In the Kitaev chain model, adding SOC results in the final Hamiltonian:

$$H = \left(\frac{k^2}{2m} + \alpha\sigma_y k - \mu\right)\tau_z + B\sigma_z + 2\Delta\tau_y k \tag{1.23}$$

The cumulative effect of these ingredients is most clearly visible in conduction band structure diagrams in momentum space (see Fig. 1.7). The Zeeman field introduces a superconducting gap, but only in tandem with strong, perpendicular SOC. The SOC itself results in spin splitting along the momentum axis into separate spin-polarized bands. The result

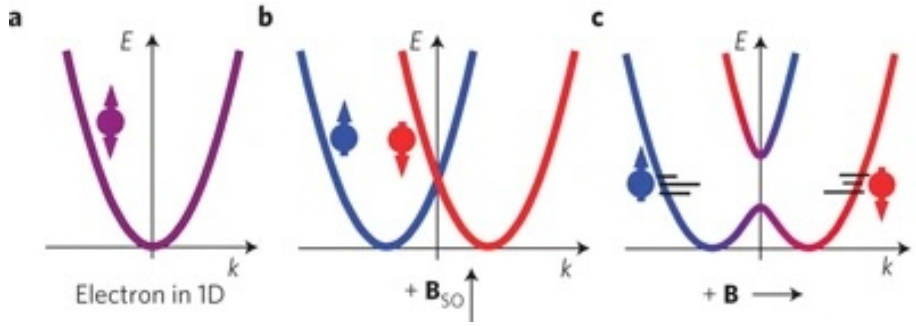


Figure 1.7: Simple conduction band diagrams for electrons in a nanowire at each stage of the "recipe:" (a) With proximity superconductivity, (b) and with SOC, and (c) and with an external perpendicular Zeeman field. Reproduced from [128] with permission from Springer Nature.

is a one-dimensional system where one can control the chemical potential, that has spinless superconductivity, and is gapped. This system accounts for every theoretical requirement of the Kitaev chain.

1.5.4 Theoretical Device Designs

After Fu and Kane's 2008 paper, the new decade brought a wave of theoretical proposals for MBS devices. The first was by Sau et al., published in early 2010, and suggested a structure comprising a semiconducting quantum well, an s-wave superconductor, and a ferromagnetic insulator [134]. As Jason Alicea would later remark, the main benefit of this proposal over Fu and Kane's was the use of a semiconductor in place of a TI [5]. Significant research in the late 1990s and early 2000s was devoted to III-V semiconductors, while TIs were comparatively new and poorly understood. Specifically, indium arsenide (InAs) had already exhibited s-wave proximity superconductivity [30] and strong Rashba SOC [112] and was thus proposed as their semiconductor of choice. Due to these properties, InAs is still extremely common in both theoretical and practical MBS devices. Creating a sufficiently high-quality interface between the semiconductor and superconductor poses an experimental challenge, but recent advances in molecular beam epitaxy have made these heterostructures more realistic [28].

Though Sau et al.'s model represented substantial progress toward a realistic MBS device, Alicea thought it possible to simplify their proposal further [5]. After thoroughly examining Sau et al.'s model, Alicea theorized that a ferromagnetic insulator might not be required to create MBSs and proposed using an in-plane magnetic field instead. Alicea's resulting structure is a tunable device composed of an s-wave superconductor and a semiconductor with Rashba and Dresselhaus SOC. Beyond its relative simplicity, Alicea boasts a few significant improvements of this two-part model over the prior three-part system. For example, it eliminates a major practical obstacle of Sau's earlier model: the necessity of a good interface between the semiconductor and ferromagnetic insulator. Most importantly, replacing the ferromagnetic insulator with an in-plane magnetic field facilitates the precise manipulation of the Zeeman field to survey the trivial-topological phase boundary. This increased control allows for a better quantum behaviour analysis and an accurate determination of the topological phase.

While Alicea's model was essential in conceptualizing Majorana devices, it contains some critical experimental limitations. Sau's proposal benefits from flexibility with the Zeeman field; however, in Alicea's theoretical device, a Zeeman field significantly larger than the proximity-induced pair field would destroy the topological phase [5]. Such a dire limitation confines the range of possible observations and restricts the choice of semiconducting material. Practical realizations required a more flexible model with fewer experimental restraints.

Lutchyn et al., the same researchers whose model preceded Alicea's, presented an alternate Majorana device model later in the same year [98]. They proposed a heterostructure composed of an infinite semiconducting quasi-1D nanowire and a SQUID (Fig. 3). Though SQUIDs are used primarily for measuring slight changes in magnetic fields, their dual Josephson junction structure means they serve as an accessible mathematical analogue for any superconductor in a theoretical MBS device. This quasi-1D structure echoes the Kitaev chain and its associated accessibility. Forming Majorana states at the end of semiconducting nanowires does not require the presence of vortices, bypassing the associated increased likelihood of decoherence [116]. Due to the experimental simplicity of quasi-1D nanowire devices, researchers continue to devote further attention to developing and improving similar models. Additionally, SQUID-based devices find additional relevance in proposals for measurement-only topological qubits [70].

A critical paper by Oreg et al. [116] examines helical electron liquid and Majorana behaviour in a similar nanowire system. The paper's most crucial contribution to the field is its mathematical analysis of how researchers can use chemical potential gates to manipulate helical liquid and Majorana activity. Though Lutchyn et al. mention the possibility of using a top gate to manipulate the chemical potential in their device, facilitating investigations of

magnetic flux effects on the system [98], Oreg et al. conceptualize sending pulses through networks of these gates as a braiding mechanism. Braiding experiments remain to be performed, but this paper by Oreg et al. may be integral to their experimental realization.

The work in this thesis is geared toward eventually realizing a particular Majorana device architecture in a 2DEG system. This design is based on work by Hell et al. [65] and Pientka et al. [122] (see Fig. 1.8), and comprises a 1D channel defined by two superconducting electrodes, much like in an SNS device. Quantum point contacts at each end of the channel serve as tunnel gates to probe local and non-local conductance effects via tunnelling spectroscopy. An external magnetic field will be applied along the 1D channel to satisfy the requirements discussed in Section 1.5.2.

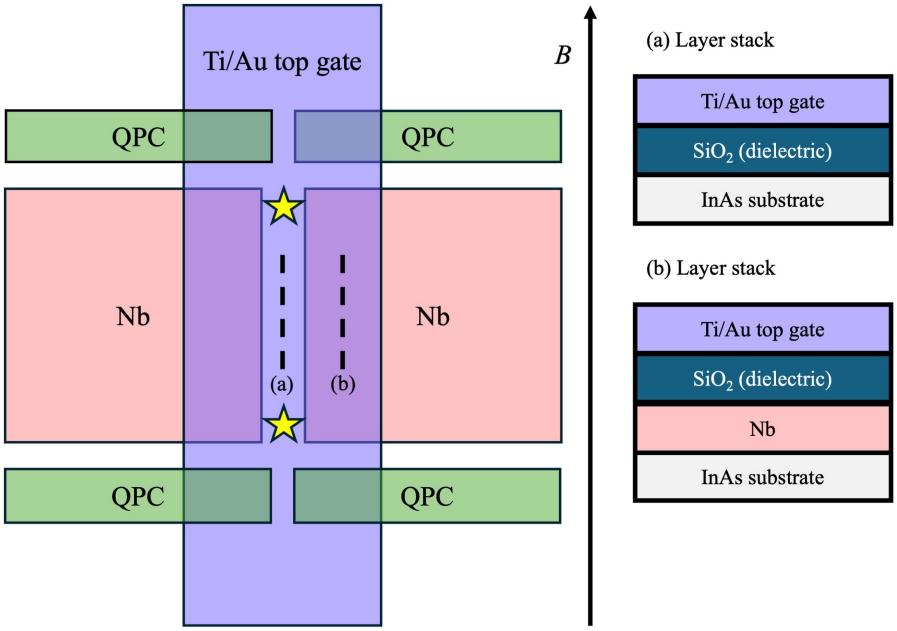


Figure 1.8: Our Majorana device design based on the work of Hell et al. [65]

1.6 Majorana Signatures

1.6.1 Zero Bias Conductance Peaks

The structure of this subsection is based on many of Sergey Frolov's talks and publications. The five properties of zero-bias conductance peaks (ZBCPs) discussed below are relatively

straightforward to measure in nanowire configurations.

The presence of magnetic-field induced ZBCPs in systems containing MBSs follows theoretically from the Kitaev chain toy model. If two phases – one trivial, the other topological and hosting MBSs – are adjacent, a zero-energy mode arises at their domain wall where the MBS is localized [3]. Perfect Andreev reflection should occur at the normal-superconductor interface, producing a resonant peak at zero energy with $2e^2/h$ quantization [174]. Mourik et al. first observed this signature in an InSb nanowire [103]. This paper concluded that the presence of these ZBCPs, and the fact that they remained stable over a range of magnetic fields but disappeared at zero field, indicated they had created MBSs. While their conclusions were sound given the scientific understanding at the time, more recent research has systematically shown that this signature alone is insufficient to prove the presence of a MBS or the topological phase. Even $2e^2/h$ quantization, once considered unique to MBSs, has recently been observed in trivial subgap bound states [93]. Despite their ubiquity in the literature, ZBCPs remain only potential reflections of MBS behaviour, not decisive confirmations.

For a ZBCP to possibly indicate the presence of a MBS, it must also be "sticky" to account for the possibility that a crossing at zero conductance may happen incidentally at some magnetic fields. Varying the magnetic field and ascertaining the stability of these peaks across a range of fields is necessary. Similarly, the width of the peak must be less than the magnetic field extent ($e\delta V < \delta E_z = g\mu\delta B$) [48]. However, even a "sticky" ZBCP is not enough; many papers have demonstrated that non-topological phenomena, such as ABSs [29, 39, 94], the Kondo effect [103], and smooth end confinement [83], can appear very similar to those caused by MBSs and may all be present in the same systems.

Spin-orbit anisotropy is another critical feature of a system with ZBCPs resulting from MBSs. In a system with spin-orbit coupling (SOC) – required for a system to elicit MBSs (see Section 1.5.3) – there is a crucial point at which the ZBCP will disappear: when the magnetic field is oriented along the spin-orbit field [48]. *Anisotropy* refers to a non-uniformity in a physical property across different measurement directions. Here, MBSs only arise when the Zeeman field is applied perpendicular to the SOC.

The last three necessary features of ZBCPs, as suggested by Sergey Frolov [48], are more straightforward to explain. Firstly, a unique and essential feature of MBSs, arising from their nature as particle-antiparticle pairs, is that they annihilate when overlapped (or *fused*). The discrete ZBCP only appears when the MBSs are sufficiently well-separated that their wavefunctions do not overlap; if they are brought closer together, the ZBCP will begin to split. Therefore, one proposed detection method is examining the ZBCPs at different distances between MBSs. Similarly, all phenomena must be measured at both

ends of the 1D channel, as MBSs always form in pairs. Finally, MBSs cannot form at arbitrary electric and magnetic fields; instead, they only appear in a specific region of phase space. The limits on field magnitudes are explained in more detail in the original theoretical papers discussed in Section 1.5.4. Ultimately, the key message of this section is that, to ascertain and claim the presence of MBSs based on a ZBCP, all these signatures – sticking to zero bias, spin-orbit anisotropy, existing over a reasonable range of electric and magnetic fields, peak splitting, and doubling – should be observed and reported.

There may be other methods to distinguish between ZBCPs caused by trivial and topological phenomena. In 2020, Haining Pan and Sankar das Sarma published a clever and catchy classification method for ZBCPs in quasi-1D semiconductor-superconductor heterostructures [119]. "Good" ZBCPs are those created by topological MBSs as predicted theoretically, free of disorder and completely non-trivial. Trivial phenomena create "bad" ZBCPs; for example, two ABSs may produce a ZBCP that appears stable and near zero energy. Finally, an "ugly" ZBCP may be created entirely by disorder; surprisingly, these peaks may be "well-correlated", appearing superficially like the "good" variety in the authors' simulations. The implications of these simulations are concerning: if ZBCPs arising from disorder or ABSs are so similar to those arising from topology, can they still be used to demonstrate the presence of MBSs?

Unfortunately, this classification method does not propose a strategy to distinguish between the different types of ZBCPs after measurement. Lai et al. addressed this challenge by introducing a dimensionless quality factor F to reflect the degree of conductance quantization [93]. The authors determined that F values higher than 80 indicate measurements in the topological phase, quantifying the critical distinction between topological and trivial ZBCPs. The major limitation of the quality-factor approach is its inherent ambiguity, as the authors cite many numerical ranges of F that could indicate multiple ZBCP sources. However, these approaches represent a positive change in the field's attitude towards ZBCPs, suggesting a scientific skepticism that will hopefully lead to more thorough analyses of potential MBS devices.

1.6.2 Other Signatures

Rather than analyzing only local phenomena like ZBCPs, ancillary measurements of bulk properties might allow more conclusive identification of MBSs. For example, Coulomb blockade spectroscopy can facilitate the precise analysis of nonlocal transport phenomena [123]. Albrecht et al. observed increasing exponential protection of ZBCPs with increasing nanowire length in a Majorana island device, simultaneously demonstrating the presence

of zero-energy end modes and how their separation impacts their degree of protection [4]. This experiment is a counterpart to the short-wire resonances discussed by Das Sarma et al. [37], completing the picture of how wire length impacts MBSs' energy profiles. Though experiments like these require very precise voltage manipulation [123], a definite engineering challenge, they provide an opportunity to build upon current experiments without reinventing their theoretical foundation.

Similarly, a protocol suggested by Pikulin et al. may help eliminate "bad" and "ugly" ZBCPs by probing topological transitions [123]. They provide a scheme for a three-terminal device comprised of a wire, one superconducting contact and two normal contacts. Plunger and cutter gates control chemical potential and tunnelling, respectively. The phase transition of a stable topological phase appears as the closing and reopening of the bulk energy gap. This phenomenon can be measured using broad radio-frequency scans and subsequent measurements of nonlocal conductance. The authors claim three main benefits of their approach: objectivity due to a specific protocol, high standards for declaring the presence of a ZBCP, and efficient identification of zero modes. Quantitative protocols like this one may help scientists measure and analyze ZBCPs without prematurely claiming that they have produced MBSs. Section 7.1 includes more detail about the outlook of this protocol and its relevance to our work.

1.6.3 Braiding Experiments

The search for a foolproof method of distinguishing trivial and topological ZBCPs is ongoing, but achieving successful braiding experiments is the field's ultimate goal [16]. Optimism about achieving braiding experiments with Majorana quasiparticles received a boon in 2020 with the publication of *Nature Physics* vol. 16; it included two papers about braiding experiments. The first discusses braiding vortices in arrays of photonic waveguides and observes a geometric phase π induced when the photonic vortices undergo a rotation of 2π [113]. The second employs an electronic Fabry-Perot interferometer to braid backscattered quasiparticles in a $\nu = 1/3$ fractional quantum Hall (FQH) state (see Section 3.2), observing a phase of $2\pi/3$, which is mathematically consistent with the first result [105]. None of these anyons are MBSs, which are needed to perform this type of quantum computing (involving charge-parity readouts) due to their nature as interacting particle-antiparticle pairs. However, these material platforms may provide a valuable avenue for studying braiding itself, augmenting current efforts toward MBS braiding. Numerical simulations and mathematical theory papers are also critical in this respect and are a very active area of research [84, 97, 178].

There are numerous experimental challenges to bypass before Majorana braiding becomes a reality. The bulk of Majorana research is devoted to quasi-1D nanowire systems; however, by definition, 2D braiding operations cannot be performed in one dimension. Nanowire research continues to enrich the collective understanding of Majorana states, test new material systems, and support research like Lai et al.'s [93]. Still, it may not ultimately be able to bring the field to its goal of topological quantum computing. Some recent work challenges this supposition, proposing the use of quasi-1D systems with auxiliary qubits [107] or using 1D exchange statistics that are representations of the *traid* (rather than braid) group [104]. The realistic outlook of these suggestions remains to be seen.

Nanowire networks, an extension of the Kitaev chain model, are among many proposals for 2D MBS devices. If MBSs exist at the ends of nanowires, introducing junctions or stacking multiple wires may allow for braiding without requiring the presence of vortices. For example, Kraus et al. [92] proposed implementing the Deutsch-Jozsa algorithm, a standard and essential quantum-mechanical algorithm, by braiding Majoranas in two adjacent wires. This paper is only one of many proposals involving wire networks, others involving T- or Y-shaped connections [118] and many different gate setups. Still, even the most straightforward of these braiding experiments have yet to be performed in a laboratory.

Realizing non-Abelian statistics independent of Majorana physics is beyond the scope of this thesis, but it is worth mentioning that there is ongoing research on other methods of topological quantum computing. Some recent examples include the entanglement of trapped ions to create non-Abelian anyons [75] and work involving quantum anomalous Hall insulators to create topological Dirac fermionic modes [172].

1.7 Josephson Junctions

The Josephson junction (JJ) is one of the most fundamental building blocks of superconducting qubits and experimental systems investigating behaviour at superconductor interfaces. JJs comprise a non-superconducting material between two superconductors; this material may be an insulator, "normal" (non-superconducting) metal, or ferromagnet. Cooper pairs tunnel through the junction, producing a supercurrent at zero applied voltage. This phenomenon is known as the Josephson effect and is harnessed in many devices, such as superconducting quantum interference devices (SQUIDs) [55].

The two Josephson equations describe the behaviour of a JJ:

$$I = I_c \sin \phi \tag{1.24}$$

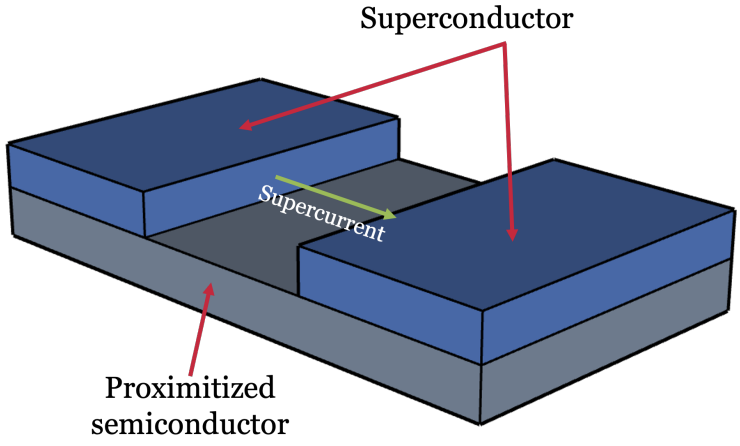


Figure 1.9: A planar Josephson junction device of the type measured later in this thesis. The semiconducting region between the two superconducting electrodes is made superconducting via the proximity effect.

$$\frac{\delta\phi}{\delta t} = \frac{2eV}{\hbar} \tag{1.25}$$

where I is the current through the junction, I_c is the critical current, ϕ is the Josephson phase (the difference in Ginzburg-Landau phase between the two electrodes), and V is the voltage across the junction. *Critical current* is an important parameter: it quantifies the maximum supercurrent through the JJ. It depends on the superconductor's intrinsic properties and changes in temperature and magnetic field [6] and is discussed in more detail in Chapter 6.

A JJ may fall into different *transport regimes* depending on the device geometry. A few key material properties determine the boundaries of each regime. The first is the coherence length in the ballistic regime in the proximitized gap,

$$\xi_b = \frac{\hbar v_F}{2\Delta} \tag{1.26}$$

where

$$v_F = \frac{\hbar k_F}{m^*} \tag{1.27}$$

is the Fermi velocity, and

$$\Delta = 1.76 k_b T_c \tag{1.28}$$

is the superconducting energy gap, and T_c is the critical temperature. The mean free path l_e is

$$l_e = \frac{\hbar \mu k_F}{e} \tag{1.29}$$

where

$$k_F = \sqrt{2\pi n_{2D}} \tag{1.30}$$

is the Fermi wavevector. A junction is *dirty* (versus *clean*) when

$$l_e \lessapprox \xi_b, \tag{1.31}$$

short (versus *long*) when

$$L < \xi_b, \tag{1.32}$$

and *diffusive* (versus *quasi-ballistic*) when

$$l_e < L. \tag{1.33}$$

In the diffusive transport regime, particles are subject to numerous scattering events, meaning their movement is randomized. On the other hand, ballistic transport occurs when the particle's movement is unobstructed. Quasi-ballistic transport is (unsurprisingly) largely ballistic, but the particle will still undergo some degree of scattering. It is worth clarifying that ballistic transport does not necessarily guarantee the maintenance of phase coherence. To achieve genuinely ballistic transport, L would need to be much smaller than the mean free path, which is much more challenging in planar devices than in nanowires. Studying all transport regimes is beneficial in determining the ideal dimensions for a device depending on its desired applications.

1.8 Indium Arsenide and Indium Antimonide

There are many potential candidates for materials that can fulfill the requirements for topological effects, including II-V semiconductors like Cd_3As_2, layered chalcogenides like $ZrTe_5$, and rare-earth pyrochlore iridates like $Eu_2Ir_2O_7$ [96]; however, InAs and InSb have emerged as two of the most promising. These two III-V semiconductors have small band gaps, allowing for the creation of quantum wells confining 2DEGs via band gap engineering (see Section 2.2.3). Additionally, they both have small electron effective masses, allowing for higher carrier mobilities; a large degree of SOC, a requirement for the 1D MBS "recipe;" and large Landé g-factors, which means a smaller Zeeman field would be required to push

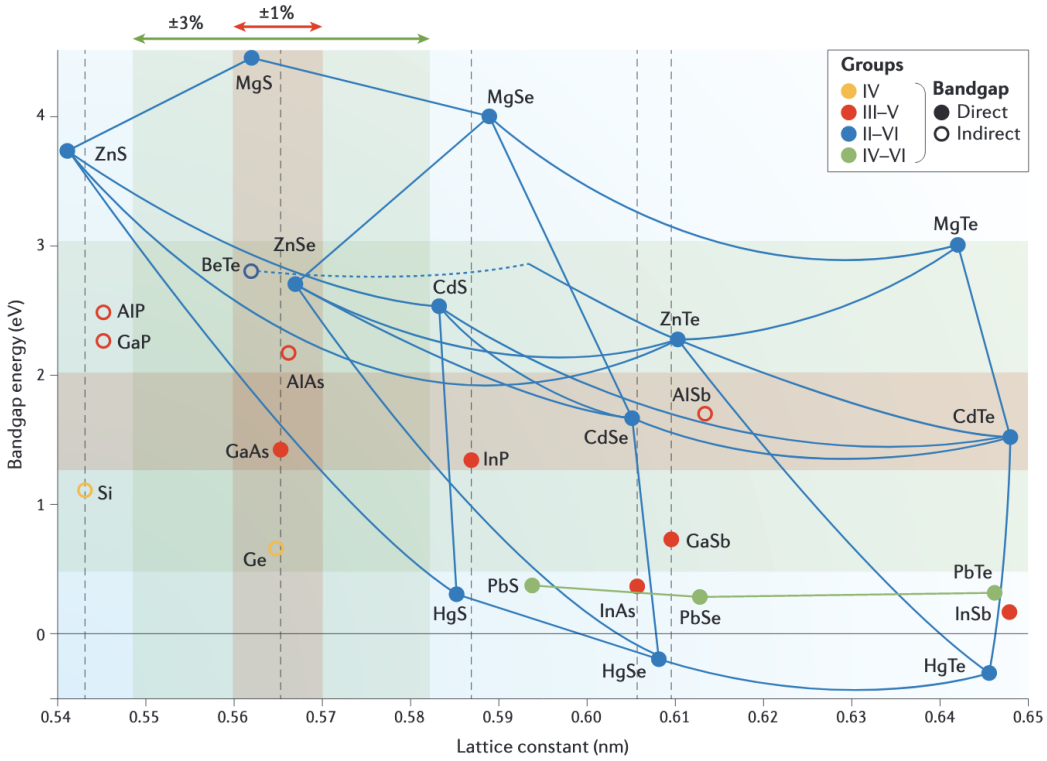


Figure 1.10: The bandgaps and lattice constants of some common elemental and compound semiconductors. Reproduced from [110] with permission from Springer Nature.

a Majorana device into the topological phase (see Table 1.1). High electron mobility is desirable for topological quantum computing applications as it increases the stability of superconductivity and facilitates better qubit correlation [95].

On the surface, InSb seems the better choice due to its stronger SOC and smaller effective mass; unfortunately, it is the surface of InSb that causes so many difficulties. Though the first papers to observe ZBCPs were in InSb nanowires, Das et al. adopted InAs in 2012 [35], motivating this decision by the fact that InAs nanowires have no *Schottky barrier* between them and the metallic electrodes. An InSb device must overcome a Schottky barrier to achieve *ohmic contact*, conducting current in both directions across the junction. On the other hand, InAs benefits from Fermi-level pinning in the conduction band, facilitating relatively easy ohmic contact formation. Ohmic contacts are required to maintain superconductivity in Majorana devices. Additionally, InAs has a lattice constant more similar to other III-V semiconductors [135], allowing for more straightforward strain engi-

Property	InAs	InSb
Small electron effective mass	$0.023m_e^*$ [106]	$0.014m_e^*$ [72]
Large Rashba SOC coefficient	117.1 eÅ^2 [169]	523.0 eÅ^2 [169]
Large Landé g-factor	$\|g\| = 14.7$ [91]	$\|g\| = 51$ [127]

Table 1.1: Desirable material properties for Majorana devices and their respective values for bulk InAs and InSb.

neering to reduce strain-induced dislocations in devices involving multiple semiconductor layers (see Fig. 1.10). On a practical basis, InSb growths have historically been plagued by high densities of structural defects. Our group recently addressed this challenge and created high-quality InSb surface quantum wells (in Reference [19]), but this work – which is geared towards ultimately forming MBSs – is instead focused on InAs for the reasons above.

Chapter 2

2DEG Quantum Well Devices from the Bottom-Up

2.1 Introduction

Two-dimensional electron gases (2DEGs) are Fermi gases with free movement in two dimensions and tight confinement in the third. These 2D ensembles may be formed on surfaces, in atomically thin materials, or – most commonly – in QWs formed at heterojunctions. The difference in band gaps between two epitaxially grown materials leads to a sharp change in conduction band energy at their interface and forms a quantum well. If the Fermi level is higher than the conduction band energy of the lower-bandgap material, the well will be populated by charges. Ideally, only one conduction subband will be under the Fermi level; otherwise, intersubband interactions may cause parasitic parallel conduction and increased scattering, leading to decreased carrier mobility. Careful growth engineering and electrostatic gating control the subband population. Importantly, when a QW containing a 2DEG is at the surface of a device, it is compatible with proximity-induced superconductivity. This renders the material system capable of being used for future Majorana devices and other superconducting applications. However, the necessity of using a surface quantum well (SQW) comes at the cost of mobility due to increased scattering from surface states and defects [95]. These properties must be balanced to create the most efficient and effective device.

Devices involving a quantum well containing a two-dimensional electron gas (2DEG) and quasi-1D channel are a class of device platforms with the distinct benefit of future scalability [65]. The use of 2DEGs follows naturally from proposals involving TIs; according

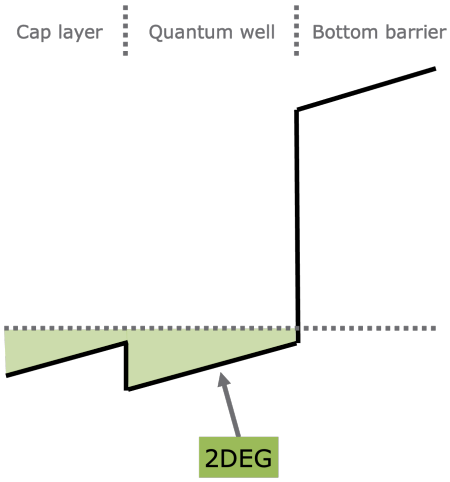


Figure 2.1: Generic conduction bandstructure for a surface quantum well with a cap layer designed for proximity effect applications. The dotted horizontal line represents the Fermi level. The 2DEG wavefunction is not entirely confined to the QW; it is also partially localized in the cap layer. The extent of this wavefunction penetration depends on the well's size and the materials of its neighbouring layers.

to Fu and Kane, the metallic surface of a TI is "essentially half of an ordinary 2D electron gas" [51]. However, the introduction of a second dimension and 2DEGs comes with more challenging fabrication and increased opportunities for error. Thus far, researchers have demonstrated that these systems exhibit some behaviour indicative of topological protection, such as half-integer quantization of thermal Hall conductance [82]. This phenomenon supports the presence of chiral Majorana edge modes. Furthermore, O'Farrell et al. constructed a 2D InAs-epitaxial Al Coulomb island device and observed interesting oscillatory effects "consistent with" Majorana behaviour but did not venture to conclude that MBSs were present [114]. Producing a substantiated claim that MBSs have been observed in 2DEG devices is a very active area of research and is one of the primary motivations behind this work.

This chapter addresses the methods used to create the devices described and analyzed in this thesis and the chemical and physical motivations of the many choices made along the way. All the processes described here must be optimized to achieve high-quality proximitized devices with characteristics ideal for applications in topological quantum computing. This chapter is heavily focused on III/V materials systems and InAs in particular.

2.2 Epitaxial Growth

Molecular beam epitaxy (MBE) is the current state-of-the-art approach to manufacture high-quality semiconductor devices. In this process, crystalline layers are adsorbed on a substrate under ultra-high vacuum (UHV) [46]. This UHV environment is necessary to control the deposition rate and purity of the surfaces. The flux of the gas molecules impinging on the substrate can be roughly modelled by the Hertz-Knudsen equation, governed by Langmuirian adsorption:

$$\phi = \frac{N_A p}{\sqrt{2\pi M R T}} \tag{2.1}$$

where N_A is Avogadro's number, M is molar mass, and p is pressure [90]. This flux can be more accurately determined by

$$\phi = \frac{\alpha}{\sqrt{T}} \exp\left(-\frac{\beta}{T}\right) \tag{2.2}$$

where α and β are experimentally determined constants [142].

Impingement flux is not the only influence on growth rate; the sticking coefficient s, the fraction of particles incorporated into the growth layer, is a significant factor [142]. This value is near 1 for group III elements around 500°C, whereas it is often much lower for group V elements [162]. For the growth of III-V semiconductors like InAs and InSb, the In flux is, therefore, the rate-limiting factor, provided the V/III ratio is kept above 1:1 [142].

The MBE system is a complex machine comprising many parts, all of which have unique purposes. The University of Waterloo MBE Laboratory specifically uses a Veeco GEN10™ machine with four isolated modules: a load lock for loading and unloading wafers; a cluster tool for wafer movement and storage; a preparation module for outgassing, heating, and plasma cleaning; and a growth module, where the growth occurs [142].

2.2.1 Substrate

The substrate is the starting point for the MBE growth; all other layers are adsorbed onto this material. These substrates are typically obtained as thin (< 1 mm) wafers and can be used in full (up to 3") or as fractional pieces. For example, two of the growths used in this research, G743 and G782, were grown on 1/4 of a 2" wafer and a whole 2" wafer respectively.

The choice of the substrate material is one of the first important decisions made in the growth process. There is a limited pool of options from which to choose, as a substrate must be well-suited to being used for MBE. Standard options include sapphire (Al_2O_3), silicon, and the III-V semiconductors GaAs and GaSb. Generally, the substrate is chosen to minimize lattice strain, as devices grown with lattice-mismatched substrates are more likely to have rough surfaces and lower mobilities [95]. Additionally, substrate layers may be either conducting or insulating. A conductive substrate may be used as a back gate, while an insulating one may decrease the likelihood of parallel conduction. Crystal orientation, defined by Miller indices, is also an important consideration. For example, differences in surface orientation can change the concentration of dangling bonds, requiring different growth temperatures [78]. GaSb (001) is used in all devices reported in this thesis due to its lattice mismatch of only 0.6% to InAs [95] and the availability of high-quality material.

Using a high-quality substrate is integral to avoid *threading dislocations* (TDs). TDs occur in strained systems and may permeate through many layers of a device and further create misfit dislocations (MDs) [77]: missing bonds at the interface of two epitaxial layers with different lattice constants [121]. If these defects reach the active portion of a device, they may drastically impact device efficiency. Thankfully, it is possible to obtain substrates with threading dislocation densities as low as 1×10^5 cm^{-2} [142]; however, these are not the only potential source of TDs, as any lattice mismatch throughout the device can propagate dislocations. Even despite the importance of minimizing TDs, practical concerns such as availability and quality can lead researchers to select poorly matched substrates and compensate with a buffer layer (see Section 2.2.2). Adding a *nucleation layer* made of the same material as the substrate also helps prevent the propagation of defects into the active area of a device by encouraging them to terminate within the lattice-matched layer.

After the substrate is loaded into the MBE system, it must be processed before any epitaxial growth. For this project, after being placed in the load-lock chamber, the substrate is heated to approximately 200°C and vacuum-pumped to remove moisture. Then, in the preparation module, a much higher temperature – 800°C – can be achieved, eliminating further contamination. The preparation module also facilitates plasma cleaning if necessary. During growth, the substrate may be rotated by a substrate manipulator to ensure even growth. The temperature of the substrate during further steps also impacts the process and its efficacy; for example, at low growth temperatures, the sticking coefficient s is higher for Sb than for As, requiring unique considerations. [142] Our group has found that this temperature difference is also a significant factor in the success of the growth of the subsequent buffer layer [18].

2.2.2 Buffer

As discussed in the last section and mentioned in Section 1.8, lattice mismatches between epitaxial layers can contribute to strain-induced dislocations like TDs and MDs. Including a buffer layer with an appropriate lattice constant is a common strategy to reduce the incidence of dislocations. The buffer layer can also separate a conductive substrate and active region to prevent alternative conductive pathways and resulting parasitic parallel conduction [143].

There are a few different approaches to growing these metamorphic buffers [141]. One type of buffer layer often used in these 2DEG devices is a *step-graded* buffer layer. In these layers, the lattice constant is carefully iterated from one closer to the substrate to one more closely matching the QW material. Another type is the *superlattice*, where multiple materials are grown in alternating layers. Finally, a thick single-layer buffer – provided its lattice constant is sufficiently well-matched to its neighbouring layers – may be sufficient to decrease the impact of dislocations as they become less likely to propagate into the device's active region. Using the latter buffer type simplifies the growth optimization process, though it is not viable for all devices.

Optimizing the growth parameters for these buffer layers is an integral step in the epitaxial growth process. Temperature can, once again, play a significant role in the success of the buffer. For example, researchers in our group [20, 142] previously found that increasing the growth temperature of a GaSb buffer from 400 to 510°C decreased the density of dislocations but reduced the resistance below the threshold for electrical isolation. This issue would likely lead to parallel conduction. Similarly, it isn't easy to generalize the impact of factors like III/V ratio and alloy composition on the success of a buffer layer. In the same investigation, our group determined that an increased aluminum composition increases resistivity but could not reach conclusions about the impact of increasing the band gap [20, 142]. The only path forward is to carefully optimize these factors for each growth.

2.2.3 Bottom Barrier

The difference between the band gap of the bottom barrier layer and the quantum well is the variable that creates quantum confinement. A higher difference is preferential, creating larger 2DEG carrier densities and stronger confinement. The bottom barrier must also be insulating to prevent parallel conduction, and it also must be lattice-matched to avoid the propagation of dislocations.

2.2.4 Interface

The character of the interface between the bottom barrier and the quantum well can be controlled by changing the shutter sequence in the MBE system. For example, our devices have an AlGaSb bottom barrier and an InAs QW. If the bottom barrier growth sequence is terminated with Al and the QW growth begins with As, the interface is deemed "AlAs-like"; conversely, an "InSb-like" interface is created by ending the bottom barrier growth with Sb and starting the QW growth with In.

The interface's impact on transport properties involves a tradeoff between electron density and mobility. An otherwise-identical device with an AlAs-like interface will likely have higher electron densities than its InSb-like counterpart due to antisite defects where As replaces Al atoms and becomes ionized [157]. Unfortunately, this increased density comes at the cost of mobility since the interface roughness thus increases [18]. Looking ahead to our goal of a Majorana device, higher mobility is more important than higher density; therefore, the later generations of devices described in this work will be fabricated with InSb-like interfaces, though many of the Hall bars and the ungated SNS devices still use AlAs-like interfaces.

2.2.5 Quantum Well

In keeping with the considerations for the other layers, the material of the quantum well layer is vital to its function. Even among III/V semiconductors, different materials contribute their inherent properties to cause differences in mobility and density. The QW must be lattice matched to its neighbouring layers and have a sufficiently different bandgap to ensure confinement. As always, there are exceptions; for example, strained quantum wells (those with lattice mismatches) can be used for photonic devices like lasers [1] and solar cells [164].

Decreasing the SQW size – practically speaking, reducing the thickness of the QW epitaxial layer – is theoretically anticipated to both reduce multisubband occupation and reduce the magnitude of the voltage needed to reach *pinch-off*. The pinch-off voltage refers to the gate voltage at which the 2DEG is no longer populated. This effect can be explained from the fundamental quantum mechanical model of an infinite potential well; a decrease in QW width leads to a larger difference in energy between each energy level. In the case of strained QWs, the width of the QW must be less than some critical thickness dependent on the difference in lattice constant to avoid excess dislocations [45]. Necessarily, however, a narrower well will also have a lower density of states and the 2DEG wavefunction may not be as strongly localized in the QW.

2.2.6 Cap Layer

The primary purpose of the cap layer is to protect the QW from surface damage, but it also controls the extent of the proximity effect in the case of SNS devices. As shown in Fig. 2.1, the cap layer may be conductive depending on bandgap offsets and the size of the QW. The cap layer material has been demonstrated to significantly impact carrier mobility. For example, a study by Lee et al. [95] compared the mobilities of devices with 10 nm $Al_{0.9}Ga_{0.1}Sb$ and $In_{0.75}Ga_{0.25}As$ cap layers. The latter was found to have much lower mobility (the values were 65×10^4 and 2.4×10^4 cm^2/Vs respectively) due to the presence of charged dislocations, alloy scattering, and interface roughness scattering, especially at higher densities where the electron wavefunction is closer to the surface [18]. This reduction may also be explained by the larger penetration of the 2DEG wavefunction into the InGaAs, as it has a smaller conduction band offset than AlGaSb [18]. This increased wavefunction penetration is precisely why InGaAs is an ideal cap layer for proximity superconductivity applications. Lee et al. also point out another benefit to using InGaAs as a cap layer: its resilience against nanofabrication processing techniques [95].

2.3 Nanofabrication

All the devices described in this thesis were fabricated in the Quantum-Nano Fabrication and Characterization Facility at the University of Waterloo. This facility is a cleanroom environment with ISO 4, 5, and 6 certified areas. In our laboratory, the patterning for lithography exposures is done in KLayout and exported as GDS files for use on the maskless aligner. We also sometimes use a mask aligner for our Hall bar devices. Screenshots from these GDS files are included to demonstrate the main lithography steps involved in our fabrication processes.

Significant effort was devoted to optimizing our nanofabrication techniques, and this process is ever-ongoing. My involvement in the nanofabrication process was minimal and only in a supportive capacity, so the optimization processes are not documented here; however, Emma Annelise Bergeron's doctoral thesis [20] details many of the challenges leading up to the fabrication of these devices. More detailed, step-by-step fabrication recipes are included in the appendices of her thesis.

2.3.1 Mesa

After chip cleaving and cleaning via sonication in acetone and isopropanol, one of the first steps in the nanofabrication process is to define the *mesa*. Much like the land formation, a mesa is a flat, raised area on which other fabrication steps are performed. The shape of the mesa is the first step in defining the shape of the device.

A layer of Shipley 1811 photoresist is spin coated on the sample and baked at 120°C for 90 seconds before the mesa pattern is exposed with a mask or maskless aligner. The photoresist is then developed in MF319 for 1 minute and 30 seconds. All the resists used in our processes are *positive* resists; that is, exposure to light will weaken the resist, allowing it to be removed during later processes. The unexposed areas will remain. Next, areas surrounding the mesa must be etched. In our process, this is done by using a Plasma asher for 20 s to remove the residual resist, submerging the chip in a buffered oxide etch (BOE) solution (1:10 HF:NH_4F by volume) to remove the native oxide, and then placing it in a targeted mesa etch solution (3:4:9:44 H_2O_2:H_3PO_4:$C_6H_8O_7$:H_2O by volume). The ideal etch depth is into the buffer layer. Etch depths are confirmed throughout using a profilometer.

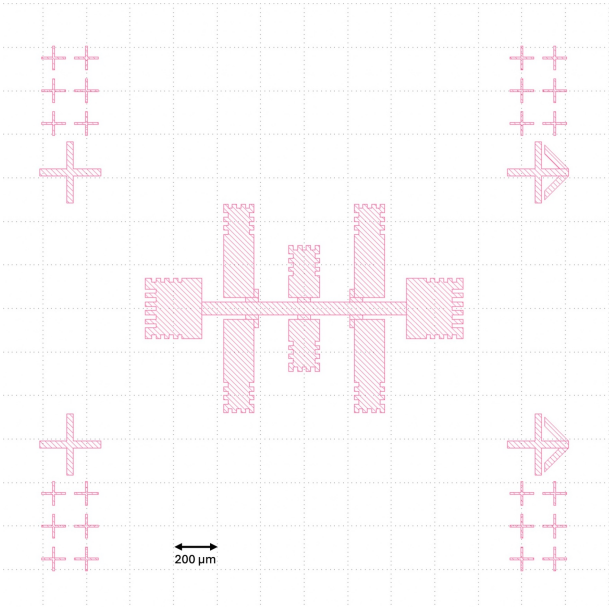


Figure 2.2: The layout file of a gated Hall bar device after only the mesa is patterned. Crosses are used as alignment marks, and arrows are used to ensure the sample remains upright.

2.3.2 Ohmic Contacts

As mentioned in Section 1.8, an ohmic contact is a metal contact on a semiconductor that can be used to apply or measure voltages and currents. Crucially, for the contact to be considered "ohmic", it must be *non-rectifying*; its current-voltage relationship must follow $V = IR$. Additionally, for use in device applications, these contacts should have low resistances [171]. We aim to achieve contacts with $R < 1$ kΩ at zero magnetic field. Practically, of course, no contact is perfect. *Hysteresis*, an asymmetry in the curve shape upon reversing the sweep direction, often appears on I-V traces due to these imperfections. At the nanoscale, imperfections can become a significant issue; contacts must be small and thin, so the interfaces and surfaces must be pristine [171].

Our group uses thermal metal evaporation, a type of physical vapour deposition (PVD), to deposit our ohmic contacts. The metal is heated to the point of evaporation until it can be directed to coat the sample evenly. Thermal deposition is less harmful to the semiconducting material than e-beam lithography, the primary alternative method, due to the potential for e-beams or x-rays to activate undesirable defect states in the semiconductor or gate dielectric. Our contacts are a 20 nm Ti and 60 nm Au bilayer deposited at a 45° angle. The Ti layer is primarily used as an adhesion layer to ensure the contacts are safely adhered throughout lift-off. It may also serve as a diffusion barrier to prevent Au atoms from diffusing into the semiconducting surface. Including a diffusion barrier increases the contacts' thermal stability, but it can introduce extra resistance [42] as Ti is more resistive than Au. Au is used for ohmic contacts due to its air stability; it does not form oxides in air. The 45° deposition angle ensures the gold sufficiently climbs the mesa sidewall.

Ohmic contacts are fabricated in four main steps: photolithography, sulphur passivation, thermal evaporation, and lift-off. The photolithography is similar to the mesa but includes a bi-layer resist recipe where both MMA EL10 and Shipley 1811 photoresists are spun, exposed, and developed. The MMA prevents etching of the surface from the developer used for the Shipley resist; the surface is now susceptible to this etchant after the previous lithography steps. Then, sulphur passivation protects the device surface against oxidation (see Section 2.3.6) in the short time it is exposed to air while being moved to a thermal evaporation chamber for metal deposition. Finally, the excess metal deposited on resist areas is removed via lift-off, which involves immersion in PG remover overnight.

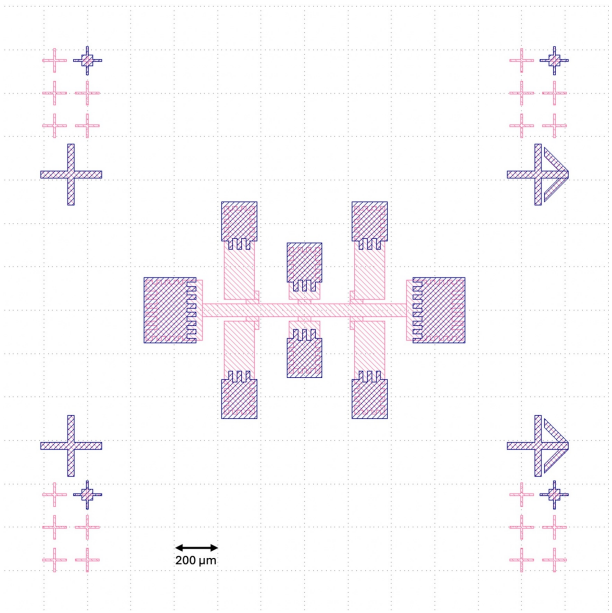


Figure 2.3: The layout file of a gated Hall bar device after the mesa and the ohmic contacts are patterned.

2.3.3 Gate Dielectric & Vias

A layer of dielectric material between prior lithography steps and the top gate is necessary. The gate dielectric prevents leakage current from flowing when a gate voltage is applied by insulating the gate from the conductive quantum well and ohmic contacts below. The dielectric layer must be thick enough to prevent leakage via tunnelling through the dielectric barrier but not so thick that it compromises the material's capacitance. The relationship between the capacitance C and the depth of an insulating layer d is

$$C = \frac{A\varepsilon_0\kappa}{d} \tag{2.3}$$

where A is the area of the electrode, ε_0 is the vacuum permittivity, and κ, or ε_r, is the characteristic relative permittivity of the dielectric. Unfortunately, the capacitance and layer thickness are inversely proportional.

There are multiple candidate materials for gate dielectrics, but SiO_2 is overwhelmingly the most common. This is partially due to ease of use in the electronics industry; it is easy to form a SiO_2 layer on a Si chip when SiO_2 is its native oxide. In the last twenty-five years, so-called "high-κ dielectrics" like Al_2O_3 and HfO_2 have been investigated as alternatives

for their ability to maintain large capacitance values at much lower thicknesses [87, 167]. As demonstrated in Chapter 4, these alternative oxides can pose issues due to their relative instability and propensity to defect formation [130].

The gate dielectric for most of our devices is deposited via atomic layer deposition (ALD). The chamber is cleaned and conditioned with 20 nm of the low-temperature oxide and corresponding precursor of choice (for SiO_2, this includes the BTBAS precursor). Then, 60 nm of the oxide is deposited on the device at 150°C. After dielectric deposition, *vias* are patterned to define an area on the ohmic contacts where the dielectric layer will be etched away. This stage is a necessary preparation for the deposition of the bond pads. The vias are patterned using a single layer of Shipley photoresist. After spin coating, the sample is placed in the Plasma asher, and profilometry confirms the resist thickness. The dielectric is then wet-etched, and the resist is stripped.

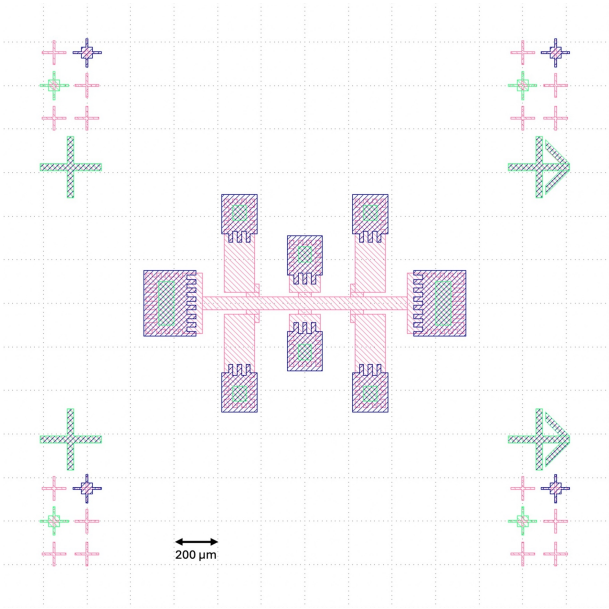


Figure 2.4: The layout file of a gated Hall bar device after the mesa, ohmic contacts, and vias are patterned.

2.3.4 Top Gate and Bond Pads

For a complete analysis of a wafer's transport properties and future applications for Majorana devices, a top gate is necessary to control the electron density (or chemical potential)

of the 2DEG. The type of gate used in our devices operates based on the *field effect*, where an externally applied electric field changes the energy level occupation at a semiconductor's surface. The conduction band is shifted up or down relative to the Fermi level depending on the sign and magnitude of the applied field. This effect can be understood by examining Poisson's equation for electrostatics [10]:

$$\nabla^2 V = -\frac{\rho}{\varepsilon} \tag{2.4}$$

where ∇^2 is the Laplacian operator, V is the electric potential, ρ is the charge density, and ε_0 is the permittivity of the medium. If a positive gate voltage $V > 0$ is applied, electrons accumulate at the surface and the 2DEG density increases; if a negative gate voltage $V < 0$ is applied, holes accumulate at the surface, and the 2DEG is *depleted* [34].

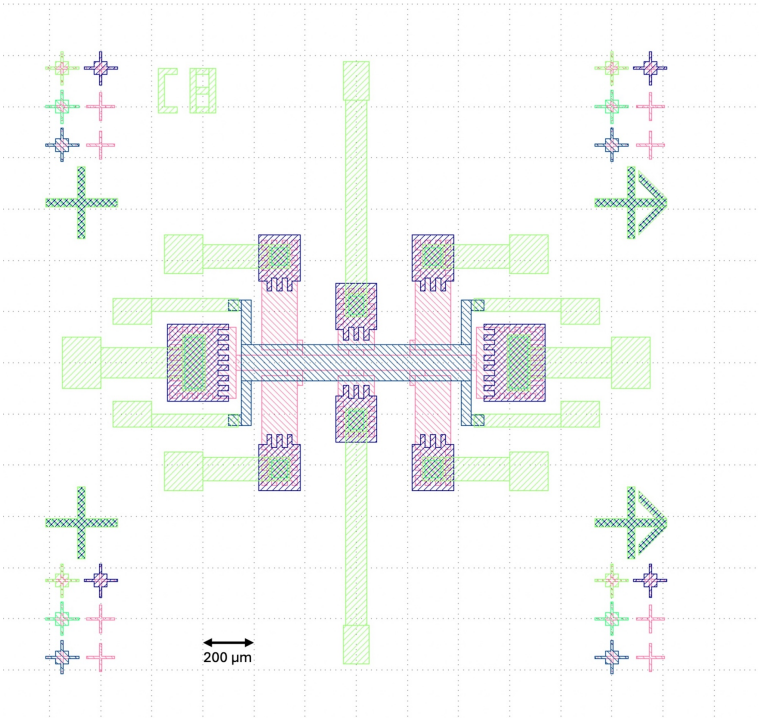


Figure 2.5: The layout file of a gated Hall bar device after the mesa, ohmic contacts, vias, top gate (black), and bond pads (light green) are patterned.

The process for patterning and depositing top gates and bond pads is very similar to that of ohmic contacts, but the sulphur passivation process is unnecessary. Instead, after

the photolithography step, the sample is plasma ashed before thermal evaporation of 45°-angled Ti/Au (20/60 nm). The resist is then stripped. The use of Ti/Au has the same advantages as its use in ohmic contacts, with the additional benefit that Au bond pads are ideal for wire bonding.

2.3.5 Superconducting Devices

Creating an SNS device still involves the optical and e-beam lithography steps described above but requires unique considerations. A mesa must be defined, in addition to optical and e-beam alignment marks to ensure good pattern alignment. The process for depositing the Nb contacts is more complex. Careful optimization of a bilayer resist method for this sputtering process is detailed in Annelise Bergeron's dissertation [20] and in the supplementary information of our most recent publication [18]; in short, a thin first PMMA layer is required to prevent the formation of undesirable Nb metal edges that climb up the edge of the resist.

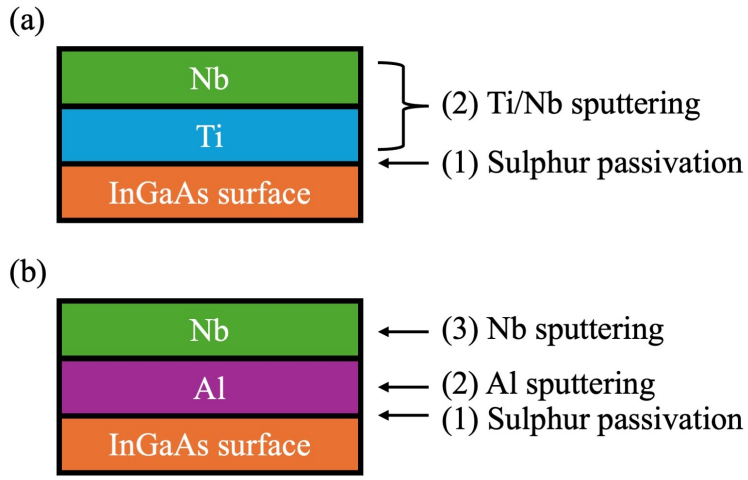


Figure 2.6: Schematic of (a) metal deposition procedure for ungated SNS devices, and (b) metal deposition procedure for future superconducting devices.

For the ungated SNS devices described in Chapter 5, the samples underwent sulphur passivation and were then quickly moved to a sputter deposition chamber for both ion milling to remove the sulphur and for Ti/Nb deposition. In the next generation of devices, we plan to entirely divorce the Nb deposition process from the sulphur deposition and switch to an Al/Nb bilayer process. The sample would be quickly moved to the deposition

chamber for Al sputtering after sulphur passivation. Then, Nb would be sputtered on top. This new process is being implemented in anticipation of future work with epitaxial aluminum, as all steps, including and after the Nb deposition, should be identical. Additionally, the Al may diffuse into the semiconductor cap layer. Diffusion is not always ideal due to the potential formation of insulating compounds, but this is not anticipated for Al on InGaAs. Instead, it may reduce the Schottky barrier between the superconductor and the InGaAs surface, thereby increasing the quality of the superconductor-semiconductor interface.

2.3.6 Sulphur Passivation

Chalcogenide passivation – sulphur passivation, in particular – is a common technique to protect the surface of a semiconductor device from oxidation when in contact with air, especially before metal deposition. If the surface is allowed to build up an oxide layer, the resulting semiconductor-metal interfaces will be of worse quality and lower transparency. Chalcogenide passivation also reduces the Schottky barrier caused by Fermi level pinning in semiconductor-superconductor heterostructures [21]. The chemical justification for this type of passivation is that dangling In and As bonds at the semiconductor surface form bonds to sulphur atoms, creating a sub-monolayer of sulphur [53]. This layer may comprise a combination of monosulfides, polysulfides, and sulphur atoms [21].

For our samples, a dilute aqueous ammonium polysulphide ($(NH_4)_2S_x$) solution is prepared, and the sample is submerged in this solution after native oxide is removed using BOE [148]. The passivation solution also etches the native oxide to some extent. To minimize the inevitable etching of the InAs by the $(NH_4)_2S_x$ solution while maintaining its passivation properties, the solution is diluted, and then excess solid sulphur is added until near saturation. Ammonium sulphide is used preferentially over sodium sulphide solutions due to the tendency for the latter to leave surface contaminants [21]. The solution is then exposed to light to initialize the oxidation-reduction process photo-electrochemically [21]. Essential considerations in developing a passivation procedure include time in the solution, light intensity, solution temperature, solution concentration, and pH. All of these decisions are optimized to ensure the solution sufficiently coats the surface without damaging the semiconducting device below.

Other methods of sulphur passivation may be explored in the future, though ours has been determined to be highly effective in creating high-transparency interfaces [20]. Non-aqueous solvents with lower dielectric constants may be more effective for sulphur passivation, perhaps due to an inversely proportional relationship between the solvent's dielectric

constant and the sulphur atoms' reactivity [80, 158]. Water is also an oxidizing agent, reducing the efficacy of oxide removal. Candidate solvents include ethanol, isopropanol, and butanol. Additionally, treatment in solution is not the only method of sulphur passivation; other methods explored for GaAs surfaces, for example, include electrochemical charging, direct deposition of GaS [158], and gas-phase passivation under UHV [21].

Chapter 3

Characterization

3.1 Measurement Apparatuses

The interesting quantum properties of many nanodevices, especially those resulting from superconductivity, only arise at exceptionally cold temperatures. Specialized equipment has been developed to facilitate magnetotransport measurements of devices at temperatures as low as 15 mK.

3.1.1 Cryostat

A *cryostat* is well-described by its name: from the Greek *kros* (icy cold) and Latin *stat* (stand), it describes a machine that maintains a very cold temperature. The Coherent Spintronics Group primarily uses a pumped ^{4}He cryostat with a base temperature of 1.6 K manufactured by Janis Research (now Lake Shore Cryotronics). Liquid ^{4}He has a base temperature of 4.2 K at 1 atm (its boiling point), but colder temperatures can be achieved by reducing pressure with vacuum pumps. Liquid nitrogen is used for shielding to increase cooling efficiency and minimize helium use.

3.1.2 Dilution Refrigerator

For publication-quality data and measurements requiring sub-1 K temperatures, a dilution refrigerator may be more suitable. The fridge used for our measurements is an Oxford

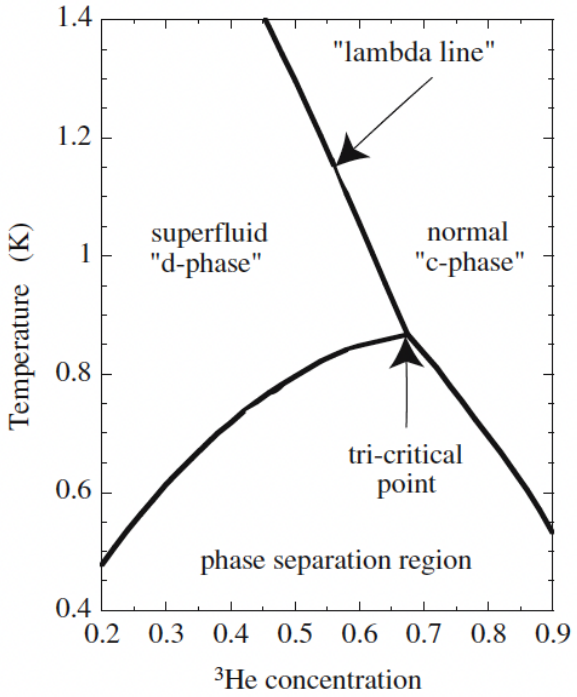


Figure 3.1: Phase diagram of a liquid helium mixture. Dilution refrigerator cooling occurs in the phase separation region. Reproduced from [76] with permission from Springer Nature.

Instruments KelvinoxTLM, which is a "wet" dilution refrigerator: the sample is directly immersed in the liquid helium bath.

The operating principle of a dilution refrigerator relies on the enthalpy of mixing of ^{3}He and ^{4}He. The phase diagram of a liquid ^{3}He-^{4}He mixture contains three distinct phases (see Fig. 3.1). Above approximately 870 mK, the mixture may either be in the normal fluid mixture or a combination of the normal liquid ^{3}He and superfluid ^{4}He. Below 870 mK, the mixture separates into two phases: a "concentrated" (^{3}He-rich) and a "dilute" (^{3}He-poor) phase. This separation induces a gradient in enthalpies ($H_{dilute} > H_{concentrated}$). Thus, the system is cooled when ^{3}He is vacuum-pumped into the dilute phase.

3.1.3 Electronic Setups

The probe containing the sample to be analyzed, inserted in the cryostat or dilution refrigerator, must be connected to electronic equipment to allow magnetotransport measurements. Before placing the sample in the probe, wires are bonded to connect the chip to its sample carrier. We use a Westbond semi-automatic wedge bonder and Al wires and connect the Ti/Au bond pads to sample carrier electrodes. In the cryostat, the sample carrier is connected to a custom-built probe and covered with a copper can to be placed in the cryostat. In the dilution refrigerator, the carrier is connected to a probe without a can and submerged directly in liquid helium.

After the probe is cooled, electrical equipment controls and measures current and voltages. We use Stanford Research Systems Model SR830 DSP Lock-In Amplifiers to measure currents and voltages, apply AC excitation, and control the measurements' reference frequencies. Stanford Research Systems Model SR560 Low-Noise Preamplifiers multiply the voltage signals by up to 50,000 times. For testing gate leakage, controlling gate voltages, and controlling the magnet's current, we use a Keithley 2401 SourceMeter source measure unit (SMU). The gate voltage may also be controlled by a Stanford Research Systems SIM928 Isolated Voltage Source or directly on the lock-in amplifier. We use an Agilent 34401 or 34410 Digital Multimeter when the DC voltage needs to be recorded. The 6 T NbTi magnet for our cryostat is powered by a Cryomagnets 4G Superconducting Magnet Power Supply, and the magnet current may also be controlled directly from this equipment. On the KelvinoxTLM fridge, the magnet is a 20 T Nb_3Sn solenoid, controlled and powered by an Oxford Instruments MercuryiPS-M.

3.2 Magnetotransport

3.2.1 Hall Effect, Mobility, and Density

The classical Hall effect describes the phenomenon where a voltage (the Hall voltage, V_H) is produced perpendicular to an applied current in the presence of an also-perpendicular magnetic field (for example, a current applied in the x direction and magnetic field in the z direction will produce a voltage in the y direction):

$$V_H = R_H I B \tag{3.1}$$

where R_H is the Hall coefficient, B is the applied magnetic field, and I is the applied current. This effect arises because charge carriers in the semiconductor are subject to

the Lorentz force once electric fields **E** and magnetic fields **B** are applied. These charge carriers get deflected by the Lorentz force in the direction of **E**×**B** [71], producing a voltage perpendicular to both.

The device geometry aptly known as the *Hall bar* (see Fig. 3.2) is ideally suited to characterize the electron mobility, density, and gating characteristics of a 2DEG wafer. This geometry comprises several Ohmic contacts (in our case, typically eight) connected to the 2DEG channel that can be used to measure the longitudinal voltage V_{xx} and transverse voltage V_{xy} and to apply a current. Though not an intrinsic part of the Hall bar design, our Hall bars typically include a top gate to facilitate the variation of bias voltage and the investigation of pinch-off characteristics.

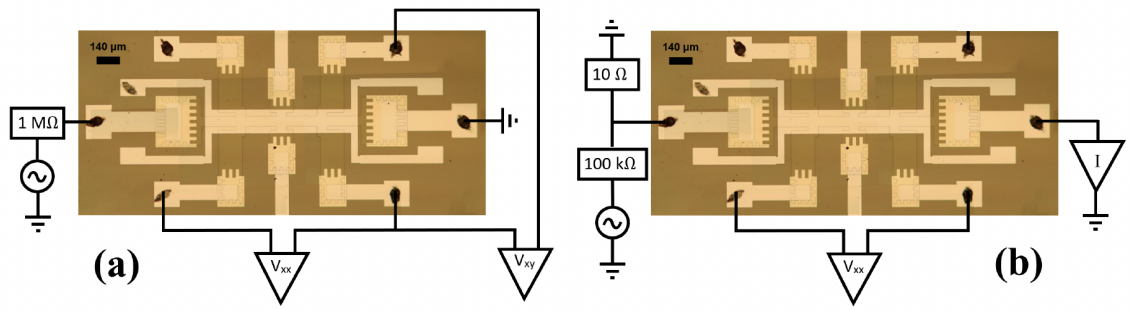


Figure 3.2: Typical measurement setups on a Hall bar geometry. The magnetic field is applied out of the plane of the images. (a) Constant current (100 nA) 4-terminal circuit setup for measuring Hall density and mobility. (b) Constant voltage (100 μV) 4-terminal circuit setup for measuring pinch-off characteristics. Triangles represent current/voltage pre-amplifiers whose voltage output is fed into an SR-830 lock-in (not shown). Reproduced from [18] with permission from AIP Publishing.

Our procedure for determining the peak mobility and corresponding 2DEG density of a gated Hall bar is as follows:

1. Set up a 2-terminal constant voltage circuit to ensure all ohmic contacts function without excess resistance.

2. Switch to a constant current 4-terminal circuit setup at zero field (see Fig. 3.2(a)) and measure V_{xx} and its corresponding phase on each longitudinal pair to evaluate the quality of the ohmic contacts. Ideally, the voltages should be the same on each side (L-R) of the device and add up to measurements across the whole device, and

the phase should be near 0°. It is easier to ascertain the "best" pair at a non-zero gate voltage, as any offset will be more pronounced.

3. At zero field, record the Hall voltage offset and its corresponding phase for each Hall pair. The "best" pair will have an offset near 0 V.

4. Measure the voltages and phases for the same pairs at +0.1 and -0.1 T. The average of these voltages will give V_H. The difference between $V_{xx,+}$ and $V_{xx,-}$ should be twice the Hall offset measured in step 3, and all V_H should be similar.

5. Steps 1-4 should have provided enough information to choose a well-working set of contacts for further measurements. Still in the constant current 4-terminal setup and non-zero magnetic field, sweep V_g over the desired range and note the initial and final V_{xy}. A safe range that does not apply a damaging voltage on the device can usually be determined by sweeping V_g until the current measurement is approximately 1% less than its value at $V_g = 0$. Repeat this three times or until the measured voltages no longer change. This is to minimize errors caused by drift and to "train" the device.

6. Record I and V_{xy} at regular V_g intervals at both +0.1 and -0.1 T. The average of both V_{xy} values will give V_H at each V_g.

7. Record I and V_{xx} at the same V_g intervals at $B = 0$ T.

8. Calculate the 2DEG density n_{2D} at each V_g:

$$n_{2D} = \frac{IB}{eV_H} \tag{3.2}$$

   where e is the elementary charge.

9. Calculate the 2DEG mobility at each V_g:

$$\mu = \frac{I\frac{L}{W}}{n_{2D}eV_{xx}} \tag{3.3}$$

   where $\frac{L}{W}$ is the number of "squares" over which V_{xx} is measured.

3.2.2 Landau Levels & the Shubnikov-de Haas Effect

When charged particles are subject to an applied magnetic field, they undergo a circular precession called *cyclotron resonance*. In a uniform magnetic field, the energies of these

orbits are quantized to discrete, degenerate *Landau levels*. The degeneracy of these levels is proportional to the sample area [3]. The derivation of the Landau quantization is made simpler by a gauge fixing known as the *Landau gauge*. The Hamiltonian for an electron in a magnetic field is

$$H = (\mathbf{p} - e\mathbf{A})^2 \tag{3.4}$$

where $\mathbf{p}$ is the particle momentum and $\mathbf{A}$ is the magnetic potential. By choosing a Landau gauge such that

$$\mathbf{A}(x, y) = \hat{\mathbf{x}}By \tag{3.5}$$

the Hamiltonian can be reduced to the one-dimensional

$$H(k) = p_y^2 + (\hbar k - eBy)^2. \tag{3.6}$$

The energy of a Landau level N is represented by

$$E_N = \hbar\omega_c \left(N + \frac{1}{2} \right). \tag{3.7}$$

The *filling factor* ν – the number of filled Landau levels at a given perpendicular magnetic field B and 2DEG density n_{2D} – can be determined from

$$\nu = \frac{n_{2D}h}{eB} \tag{3.8}$$

where ν is an integer but is not necessarily the same as N. Explaining *why* Landau level quantization occurs extends a little beyond the scope of this thesis, as it requires some complex topological treatment. A relatively accessible explanation is given in Reference [3].

Landau level quantization is closely related to the *quantum Hall effect* (QHE). At sufficiently high fields in planar devices, the relationship between the magnetic field and the Hall conductance is no longer linear and instead becomes quantized, with increasingly large ranges of magnetic fields at the same conductance. The Hall conductance at a given filling factor is

$$\sigma_H = \frac{\nu e^2}{h}. \tag{3.9}$$

This form of the effect is specifically called the *integer* QHE, in contrast to the more exotic *fractional* QHE where ν is not an integer and Hall plateaus occur at fractional values of e^2/h. Systems exhibiting the fractional QHE are also potential candidates for non-Abelian physics.

While the QHE describes the dependence of Hall conductance on the magnetic field, the longitudinal conductance is described by a different but related effect: The Shubnikov-de Haas (SdH) effect. At the transitions between Landau levels, there is a peak in longitudinal conductance that increases in magnitude with increasing filling factor. The conductance reaches zero at fields corresponding to the quantum Hall plateaus, producing an oscillating effect. The Ando equation for these oscillations in terms of the Landau level energies (Equation 3.7) is

$$\sigma_{xx} = \frac{e^2}{\pi^2\hbar}\int dE\left(-\frac{\delta f}{\delta E}\right)\sum_N\left(N+\frac{1}{2}\right)\left[1-\left(\frac{E-E_N}{\Gamma}\right)^2\right] \tag{3.10}$$

where E_N is the Landau level energy and Γ corresponds to Landau level broadening caused by disorder [102]. A Landau fan diagram (see Fig. 3.3(b)) shows how the Landau levels change when the gate voltage (the 2DEG density) is varied and the extent of level broadening.

Deviations in expected SdH behaviour often indicate the presence of multiple subbands, disorder, or both. Firstly, the SdH troughs are unlikely to reach zero conductance and may not even be visible at low fields. The visibility of oscillations is determined by

$$\frac{\hbar eB}{m^*} - \Gamma > k_B T \tag{3.11}$$

and can be used to extract the magnitude of Γ. Additionally, quantum Hall plateaus and corresponding SdH troughs will usually only appear at every other (even) filling factor at lower fields due to a lack of spin resolution, which is assumed in Equation 3.8. A similar inequality determines the visibility of spin splitting:

$$g^*\mu_B B - \Gamma > k_B T \tag{3.12}$$

where g^* is the Landé g-factor and μ_B is the Bohr magneton. Furthermore, a deviation between the Hall density (Equation 3.2) and the 2DEG density extracted from the periodicity of the SdH oscillations is an indicator of multiple subband occupation. The latter can be calculated by

$$n_{SdH} = \frac{2e}{h}\left(\frac{1}{B_{\nu+1}} - \frac{1}{B_\nu}\right)^{-1} \tag{3.13}$$

where B_ν is the magnetic field corresponding to the oscillation trough at a given Landau level. The onset of this deviation corresponds to the density at which the second (or further) subband populates the 2DEG. Section 4.2 gives an example of this numerical treatment. The Landau fan diagram may visually represent multi-subband occupation by showing the position of level crossings. A distinctive beating pattern, resulting from scattering between multiple subbands, may also be visible in the oscillations [95].

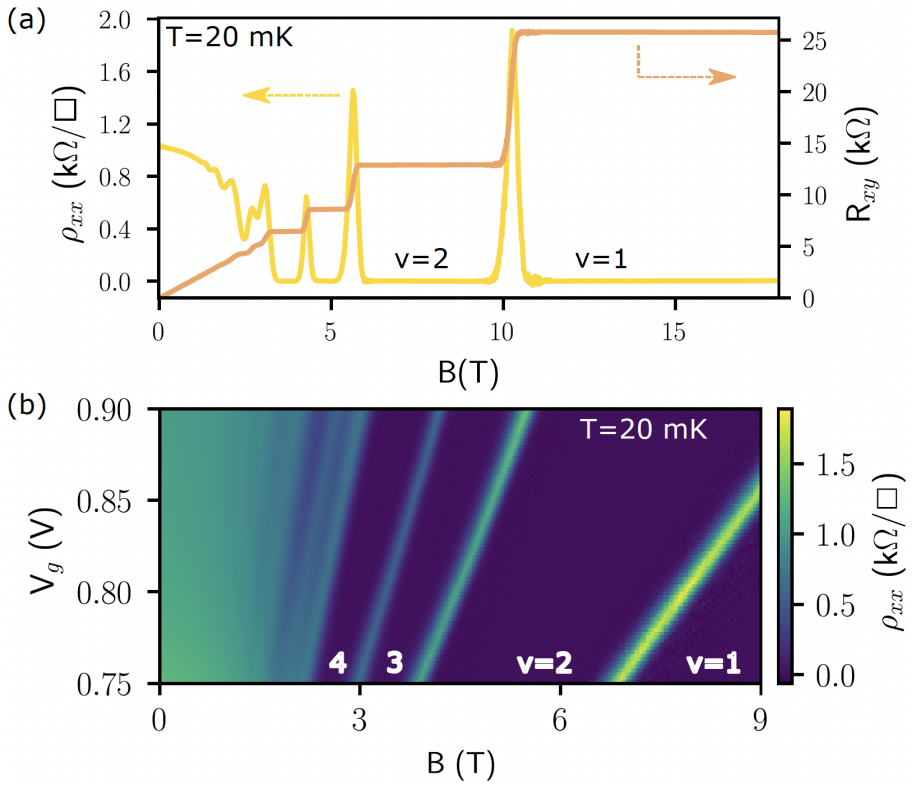


Figure 3.3: Data from our group's previous publication on InSb surface quantum wells. (a) Well-quantized Hall plateaus and clear SdH oscillations reaching zero at filling factors $\nu = 4, 3, 2, 1$ at $n_{2D} = 3.4 \times 10^{11}$ cm^{-2}. (b) Landau fan diagram: a magnetic field sweep measuring longitudinal resistivity at each gate voltage. Reproduced from [19] with permission from AIP Publishing.

3.2.3 Weak Anti-Localization

As suggested in the last subsection, all the materials we work with in the laboratory have some disorder. As a result, the movement of electrons through these devices is somewhat randomized. The Drude model of conduction describes the classical probability of a given electron's path through a material, but at very low temperatures in low-dimensional materials, experiments often find a peak in resistivity at zero field. This enhancement is called weak localization (WL) and results from constructive quantum interference between identical but time-reversed self-intersecting paths in disordered systems [133]. However, the opposite is observed in the presence of spin-orbit coupling; the resistivity is diminished

due to weak anti-localization (WAL). As discussed in Section 1.5.3, an electron's spin is coupled to its angular momentum under these conditions; therefore, the path and its time-reversed pair will see the electron spinning in opposite directions. These paths will thus interfere destructively and result in a peak in conductivity (a sharp decrease in resistivity). Therefore, the extent of the WAL is correlated to the SOC strength.

This type of data is typically presented as plots of magnetic field versus the change in longitudinal conductivity $\Delta\sigma_{xx}(B) = \sigma_{xx}(B) - \sigma_{xx}(0)$ arising from WL or WAL, where $\sigma_{xx}(B)$ is the field-dependent conductivity and $\sigma_{xx}(0)$ is the background conductivity. There are two commonly used equations to describe the change in longitudinal conductivity: the Hikami-Larkin-Nagaoka (HLN) model [68] and the related Iordanskii-Lyanda-Geller-Pikus (ILP) model [73]. The equations are as follows, respectively:

$$\begin{aligned}\Delta\sigma_{xx}(B) =& \frac{e^2}{2\pi^2\hbar}\left[\Psi\left(\frac{1}{2}+\frac{B_\phi}{B}+\frac{B_{SO}}{B}\right)+\frac{1}{2}\Psi\left(\frac{1}{2}+\frac{B_\phi}{B}+\frac{2B_{SO}}{B}\right)\right.\\ &-\frac{1}{2}\Psi\left(\frac{1}{2}+\frac{B_\phi}{B}\right)-\ln\left(\frac{B_\phi}{B}+\frac{B_{SO}}{B}\right)-\frac{1}{2}\ln\left(\frac{B_\phi}{B}+\frac{2B_{SO}}{B}\right)\\ &\left.+\frac{1}{2}\ln\left(\frac{B_\phi}{B}\right)\right]\end{aligned} \tag{3.14}$$

and

$$\begin{aligned}\Delta\sigma_{xx}(B) =& \frac{e^2}{4\pi^2\hbar}\left[\sum_{n=1}^{\infty}\left(\frac{3}{n}-\frac{3a_n^2+2a_n\frac{B_{SO}}{B}-1-2(2n+1)\frac{B_{SO}}{B}}{(a_n+\frac{B_{SO}}{B})a_{n-1}a_{n+1}-2\left(\frac{B_{SO}}{B}\right)\left((2n+1)\,a_n-1\right)}\right)\right.\\ &-\frac{1}{a_0}-\frac{2a_0+1+\frac{B_{SO}}{B}}{a_1(a_0+\frac{B_{SO}}{B})-2\frac{B_{SO}}{B}}-2\ln\left(\frac{B_\phi}{B}+\frac{B_{SO}}{B}\right)-\ln\left(\frac{B_\phi}{B}+\frac{2B_{SO}}{B}\right)\\ &\left.-3\gamma-S\left(\frac{B_\phi}{B_{SO}}\right)-\left(\Psi\left(\frac{1}{2}+\frac{B_\phi}{B}\right)-\ln\left(\frac{B_\phi}{B}\right)\right)\right]\end{aligned} \tag{3.15}$$

where

$$S(x) = \frac{8}{\sqrt{7+16x}}\left(\arctan\left(\frac{\sqrt{7+16x}}{1-2x}\right)-\pi\Theta(1-2x)\right) \tag{3.16}$$

$$a_n = n+\frac{1}{2}+\frac{B_\phi}{B}+\frac{B_{SO}}{B} \tag{3.17}$$

In the above equations, e is the elementary charge, Ψ is the Digamma function, γ is the Euler constant, Θ is the Heaviside step function, and B_ϕ and B_{SO} are fit parameters corresponding to the phase coherence and spin effective fields. Extracting these fit parameters

allows for the determination of important physical properties such as the phase coherence length l_ϕ and Rashba SOC coefficient α_{SO}:

$$\alpha_{SO} = \frac{\Delta_{SO}}{2k_F} \tag{3.18}$$

where k_F the Fermi wavevector (Equation 1.30) and the spin-orbit energy gap Δ_{SO} is

$$\Delta_{SO} = \sqrt{\frac{2\hbar^2}{\tau_D \tau_{SO}}}, \tag{3.19}$$

where the diffusion time τ_D is

$$\tau_D = \frac{m\mu_e}{e} \tag{3.20}$$

and the spin-orbit time τ_{SO} is

$$\tau_{SO} = \frac{l_{SO}}{D}, \tag{3.21}$$

where the spin-orbit length l_{SO} is

$$l_{SO} = \sqrt{\frac{\hbar}{4eB_{SO}}} \tag{3.22}$$

and the diffusion constant D is

$$D = \frac{v_F^2 \tau_D}{2}, \tag{3.23}$$

where v_F is the Fermi velocity (Equation 1.27).

3.3 Superconductivity

3.3.1 Multiple Andreev Reflections

Andreev reflection, the phenomenon responsible for the proximity effect, appears in different electrical measurements in unique ways. In SNS device architectures, resonant peaks in conductance arise from multiple Andreev reflections (MAR), analogous to the ZBCPs theorized for MBSs. These peaks appear at values of $V = 2\Delta_{MAR}/en$, where n is an integer corresponding to "the number of times that the electrons... transverse the junction before entering the leads" [115] – in other words, the number of times an electron undergoes Andreev reflection before it overcomes the energy barrier at the N-S interface. Δ_{MAR} is

the superconducting energy gap as determined from this periodic pattern. Depending on the extent of proximitization, this value may or may not match that of the parent superconductor. The appearance of these MAR peaks can hold information about transport properties such as ballistic versus diffusive behaviour [136] and interface quality.

3.3.2 Transparency

Quantifying the quality of an SNS junction can be difficult, given the multitude of phenomena at play. Interface transparency $\mathcal{T}$ is one method; a high interface transparency corresponds to a high probability of Andreev reflections and, therefore, a high-quality interface. There are two primary mathematical models used to calculate $\mathcal{T}$: the Octavion-Tinkham-Blonder-Klapwijk (OTBK) [109] and Kulik-Omelyanchuk (KO) [57] models. The former uses the MAR periodicity:

$$\frac{eI_{ex}R_N}{\Delta_{MAR}} = \frac{2(1+2Z^2)\tanh^{-1}(2\tilde{Z})}{Z\sqrt{(1+Z^2)(1+6Z^2+4Z^4)}} - \frac{4}{3} \tag{3.24}$$

$$\mathcal{T} = \sqrt{1+Z^2} \tag{3.25}$$

where $\tilde{Z} = Z\sqrt{(1+Z^2)/(1+6Z^2+4Z^4)}$, I_{ex} is the excess current, Δ_{MAR} is the superconducting gap as determined from the MAR peaks, and Z is a dimensionless scattering parameter that correlates to the barrier height at the SN interface. To find $\mathcal{T}$, the experimental data is input to Equation 3.24 to find Z, which is then input to Equation 3.25. One key assumption made by the OTBK model is that the SN interfaces are symmetric; in other words, the MAR at each interface are the same.

The KO model, on the other hand, additionally includes the temperature dependence of the critical current:

$$I_c(T,\phi,\mathcal{T}) = \frac{\pi\Delta(T)\sin\phi}{2eR_N\sqrt{1-\mathcal{T}\sin^2\left(\frac{\phi}{2}\right)}}\tanh\left(\frac{\Delta(T)\sqrt{1-\mathcal{T}\sin^2\left(\frac{\phi}{2}\right)}}{2k_BT}\right) \tag{3.26}$$

where ϕ is the superconducting phase from Andreev reflections at the SN interface and $\Delta(T) = \Delta_{MAR}\sqrt{1-(T/T_c)^2}$ is the temperature-dependent superconducting gap.

3.3.3 Hard and Soft Gaps

In proximitized semiconductors, the "hardness" of a superconducting gap refers to the proportion of quasiparticle states inside the gap; fewer quasiparticles inside means a harder

gap [131]. In practical terms, this appears as a suppression of conductance inside the gap. For applications in Majorana physics, a hard gap is more desirable; subgap conductance, characteristic of soft gaps, may contribute to the decoherence of Majorana states and prevent braiding operations [32]. Though the many mechanisms impacting superconducting gap hardness were not always clear, evidence now demonstrates that interface quality is a major factor [151].

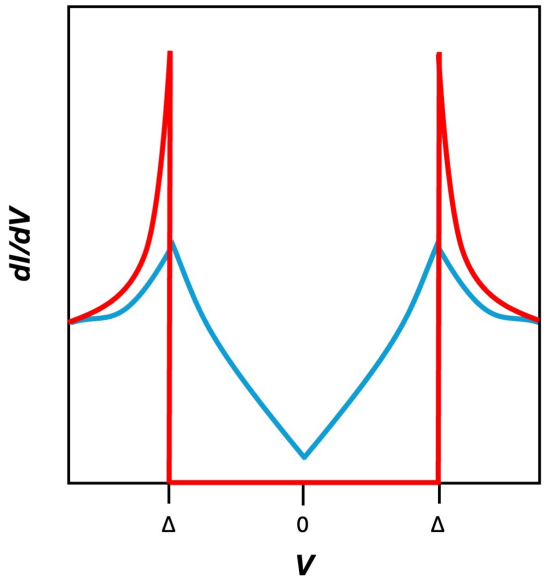


Figure 3.4: A qualitative comparison between a hard superconducting gap (red) and a soft superconducting gap (blue). Based on a figure from Reference [32] and experimental data from Reference [79].

The accepted method for distinguishing between soft and hard gaps is credited to Carlo Beenakker [14]. The theoretical formula for the minimum conductance inside the gap G_{SNS} is as follows:

$$G_{SNS} \approx \frac{G_{SN}}{2} = G_0 \frac{G_{NN}^2}{(2G_0 - G_{NN})^2} \tag{3.27}$$

where $G_0 = 2e^2/h$ is the conductance quantum and G_{NN} is the conductance outside the gap averaged over a range of V_{SD} at high bias voltages well into the normal (non-superconducting) region [41, 131]. For devices with hard gaps, the measured G_{SNS} and ratio G_{SNS}/G_{NN} should closely correspond to the values found from this formula. Qualitatively, negligible subgap conductance and easily distinguishable values of Δ suggest a hard superconducting gap, but this is not definitive.

Chapter 4

Two-dimensional electron gases in InAs/AlGaSb surface quantum wells

This chapter includes results and figures from the paper, "High transparency induced superconductivity in field effect two-dimensional electron gases in undoped InAs/AlGaSb surface quantum wells" [18] and its associated supplementary information. See the Statement of Contributions for more details.

4.1 Introduction

This work is motivated by a desire to increase the pool of materials for fabricating high-quality 2DEG devices. While surface quantum wells in In(Ga)As/$In_{0.8}Al_{0.2}As$ are well-explored for applications for topological quantum computing [138, 177], the comparatively lesser-used InAs/$Al_{0.8}Ga_{0.2}Sb$ may be more appropriate due to its better strain engineering and ability to achieve higher densities and mobilities. With these aims in mind, we fabricated gated 2DEG devices using surface quantum wells in an InAs/$Al_{0.8}Ga_{0.2}Sb$ system. Two major classes of wafers were grown: those with a 24 nm SQW and those with a 15 nm SQW.

4.2 24 nm Quantum Wells

4.2.1 Optimizing the Gate Dielectric

Three heterostructures (G743, G782, and G837) were grown using MBE. The growth layers are summarized in Table 4.1. The only difference between G743 & G782 versus G837 is the different interface characteristics.

Layer	**G743 & G782**		**G837**	
	Depth	Material	Depth	Material
Cap	6 nm	$In_{0.75}Ga_{0.25}As$	6 nm	$In_{0.75}Ga_{0.25}As$
QW	24 nm	InAs	24 nm	InAs
Interface		"AlAs-like"		"InSb-like"
Bottom Barrier	20 nm	$Al_{0.8}Ga_{0.2}Sb$	20 nm	$Al_{0.8}Ga_{0.2}Sb$
Buffer	800 nm	$Al_{0.80}Ga_{0.20}Sb_{0.93}As_{0.07}$	800 nm	$Al_{0.80}Ga_{0.20}Sb_{0.93}As_{0.07}$
Nucleation Layer	25 nm	GaSb	25 nm	GaSb
Substrate		GaSb (001)		GaSb (001)

Table 4.1: Summary of wafers with 24 nm wide InAs SQWs.

Choosing an appropriate gate dielectric is integral to creating a well-functioning device. The three most common choices for 2DEG devices aluminum oxide (Al_2O_3), silicon dioxide (SiO_2), and hafnium dioxide (HfO_2) each have their advantages. Two series of Hall bars on G743 and G782, each using either SiO_2 or HfO_2, were fabricated to investigate the relative benefits of each dielectric choice. Both devices were fabricated using atomic layer deposition (ALD) at 150°C. Al_2O_3 devices were previously manufactured, but these devices were noisy, unstable, and unable to be pinched off [20]. While both working dielectrics exhibit reproducible gating at high conductances (above 100 μS), the behaviour at lower conductances paints a different picture (see Fig. 4.1). There is noticeable hysteresis in both samples at low conductance, but the SiO_2 samples exhibit more robust reproducibility and more symmetrical behaviour in the "up" versus "down" sweeps.

Similarly, the SiO_2 devices have more predictable mobility-density correlations (see Fig. 4.2 vs. 4.3). The 2DEG density increases linearly with the gate voltage V_g in the Hall bars fabricated with SiO_2, while their HfO_2 counterparts are significantly less linear. All gated Hall bars have a peak in mobility near $n_{2D} = 2.0 \times 10^{12}$ cm^{-2}, and all but one have a peak mobility of approximately $\mu = 1.1 \times 10^4$ cm^2/Vs. The decrease in mobility below this peak is attributed to impurity scattering; above, it is likely due to interface roughness

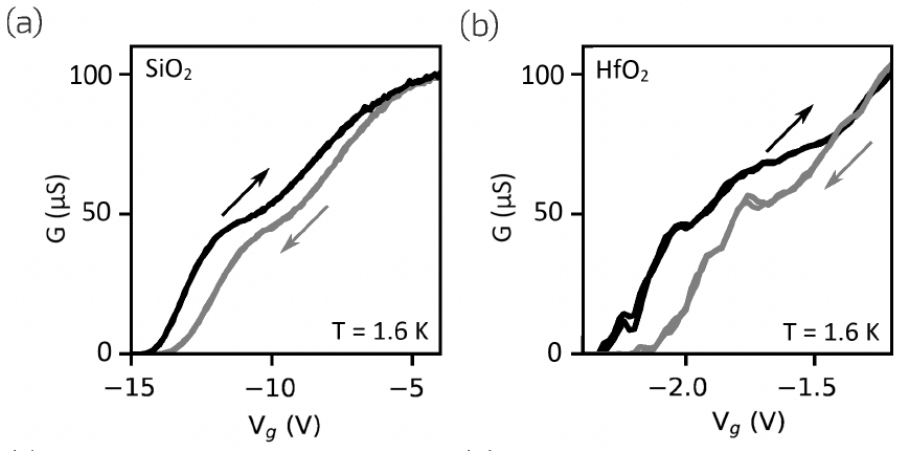


Figure 4.1: Pinch-off curves at 100 μV ac excitation for gated Hall bars with gate dielectrics (a) SiO_2 and (b) HfO_2. Four traces in each direction are shown in (a), while two in each direction are shown in (b). Reproduced from [18] with permission from AIP Publishing.

scattering or alloy scattering due to the electron wavefunction being pulled closer to the surface [8, 140].

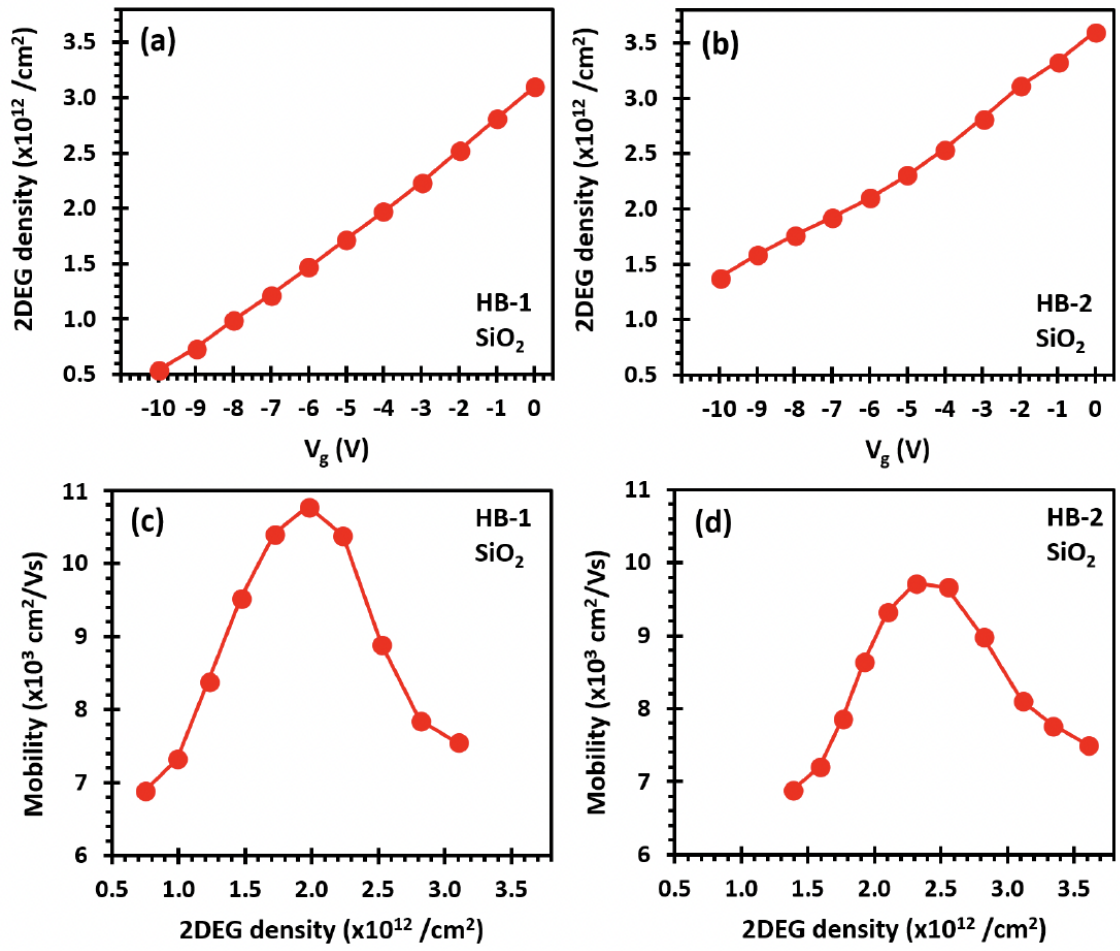


Figure 4.2: Hall density vs top gate voltage (a,b) and mobility vs 2DEG density (c,d) of devices fabricated with SiO_2. Reproduced from [18] with permission from AIP Publishing.

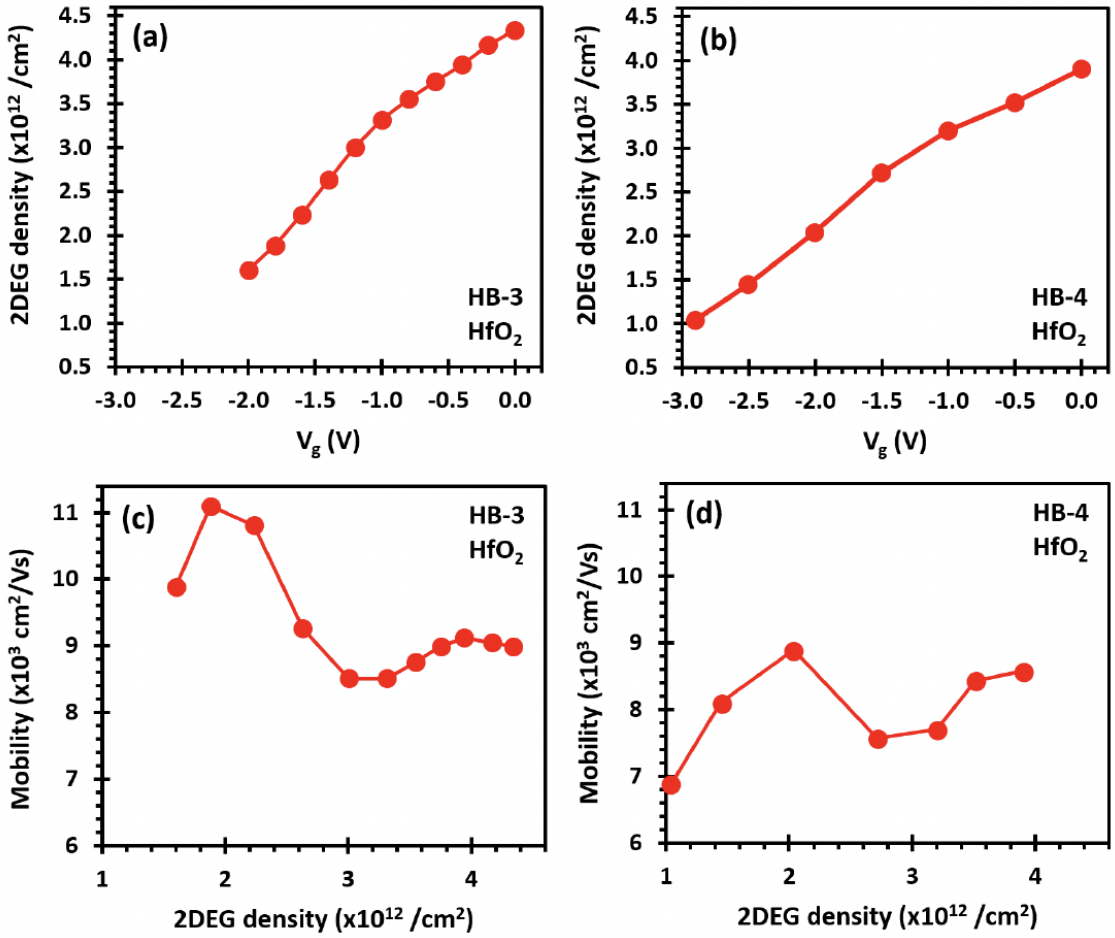


Figure 4.3: Hall density vs top gate voltage (a,b) and mobility vs 2DEG density (c,d) of devices fabricated with HfO_2. Reproduced from [18] with permission from AIP Publishing.

To further increase the number of available fabrication techniques, gated Hall bars with SiO_2 deposited using plasma-activated chemical vapour deposition (PCVD) were fabricated on wafer G837. ALD has been used historically for these devices as our nanofabrication facility's PCVD recipes involve heating to 300°C, which may damage materials containing antimonides. However, no experimental trials had been attempted by our laboratory, so we aimed to assess whether this heating process would actually decrease the efficacy of our devices. Based on our studies on G782, we might expect a slight increase in peak mobility for devices fabricated with a HfO_2 dielectric in comparison to those using SiO_2 (see Fig. 4.4(a)); the issue with the HfO_2 devices was never their mobility, but rather their lack of reproducibility and problematic I-V characteristics. However, the mobility of the G837 device with a PCVD SiO_2 dielectric is *drastically* less than its ALD HfO_2 counterpart. This difference leads us to conclude that the PCVD process introduces additional interface roughness in comparison to ALD. See Fig. 4.4 for a visual comparison of the mobility-density relationships for all four devices.

Wafer, Dielectric	μ **at** $V_g = 0$ ($\times 10^4$ cm^2/Vs)	n_{2D} ($\times 10^{12}$/cm^2)	**Peak** μ ($\times 10^4$ cm^2/Vs)	n_{2D} ($\times 10^{12}$/cm^2)
G782, ALD HfO_2	0.90	4.3	1.11	1.9
G782, ALD SiO_2	0.75	3.1	1.08	2.0
G837, ALD HfO_2	0.95	3.1	1.27	1.9
G837, PCVD SiO_2	0.79	3.8	0.89	1.6

Table 4.2: Mobilities at $V_g = 0$ V and peak mobilities for various gated Hall bars. All measurements were taken at 1.6 K.

Unfortunately, pinch-off, SdH, and Hall effect measurements further emphasize that this high-temperature deposition is likely incompatible with future device applications. While the pinch-off curves (Fig. 4.5) are well-overlapped in their respective directions, the device does not remain pinched off over time. A two-terminal current measurement at $V_g = -25$ V – below pinch-off – revealed that, after an hour, the current had increased from 0 pA to approximately 200 pA. Additionally, the SdH oscillations at $n_{2D} = 1.6 \times 10^{12}/\text{cm}^2$ are at a *very* small range of longitudinal resistivity. Hall plateaus also cannot be seen. At relatively high 2DEG densities like these, the oscillations and Hall plateaus are expected to be much better resolved. These findings suggest that the 300°C PCVD procedure does, indeed, damage the Sb-containing growth. If PCVD is hoped to be used, a recipe involving lower temperatures must be devised.

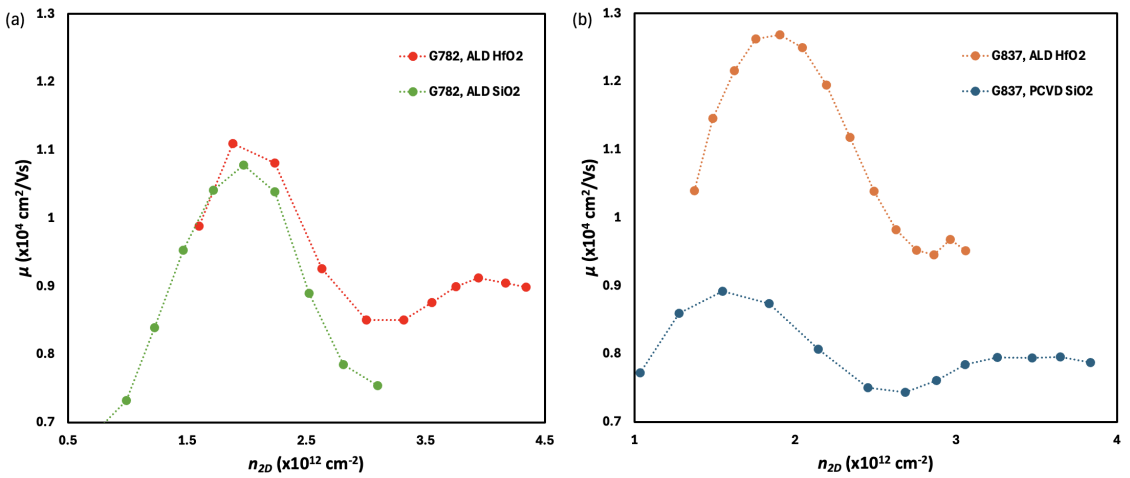


Figure 4.4: Mobility vs 2DEG density of gated Hall bars at 1.6 K on (a) G782, comparing ALD processes using HfO_2 and SiO_2 and (b) G837, comparing the ALD process using HfO_2 and the SiO_2 deposited with the PCVD process at 300°C.

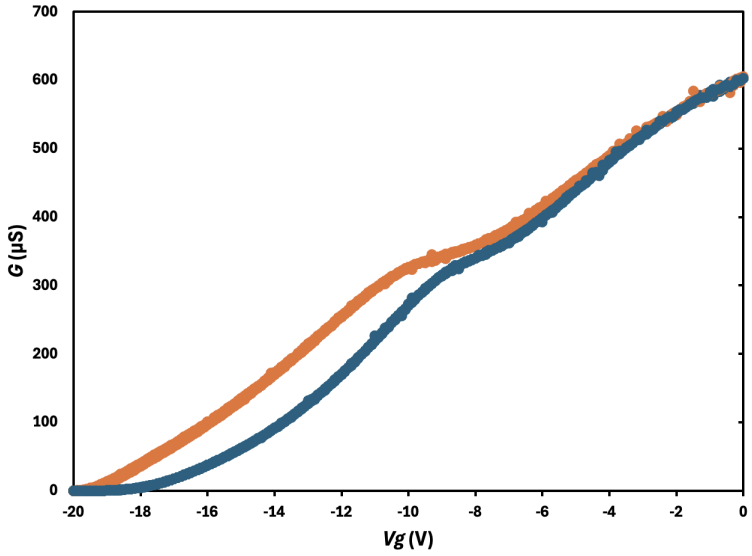


Figure 4.5: Four-terminal pinch-off curve for G837PCVDTGHBC8. Four sweeps "up" (from -20 to 0 V) are shown in orange. Four sweeps "down" (from 0 to -20 V) are shown in blue.

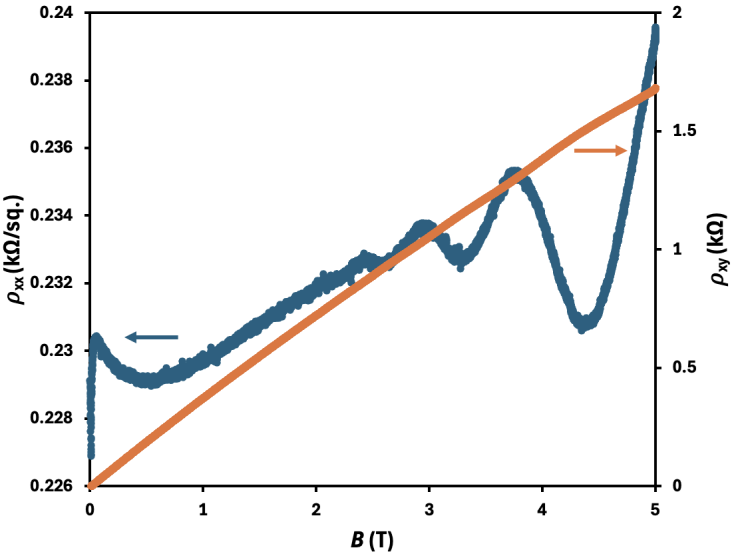


Figure 4.6: (a) SdH and quantum Hall measurements at $V_g = -10.0$ V ($n_{2D} = 1.6 \times 10^{12}$ cm^{-2}) on G837PCVDTGHBC8. Note the very small range of the oscillations (0.01 kΩ/sq.) and the lack of quantized Hall plateaus.

4.2.2 Magnetotransport of G743 & G782

Moving forward with ALD SiO_2 Hall bars, analyzing the Shubnikov-de Haas (SdH) oscillations and Hall resistance confirms the presence of a 2DEG and provides insight into the disorder and multi-subband population. Quantum Hall plateaus are seen at filling factors $\nu = 2, 4$ at $V_g = -8.0$ V, corresponding to $n_{2D} = 8.57 \times 10^{11}$ cm^{-2}. These oscillations reach $\rho_{xx} = 0$, suggesting no parallel conduction. However, there are multiple indicators of disorder associated with Landau level broadening. For example, the plateau at $\nu = 3$, corresponding to spin-splitting, is not well distinguished. Additionally, the oscillations do not appear until $B \approx 3T$. The visibility of spin-splitting and SdH oscillations are determined by Equations 3.11 and 3.12, both of which indicate a value of $\Gamma \approx 9$ meV. It is notable that the electron density at zero gate voltage in the gated Hall bar devices on G743 and G782 was much higher (2-3 times) than the electron densities of the as-grown wafers. The probable explanation is the presence of charge traps at the semiconductor-oxide interface after dielectric deposition.

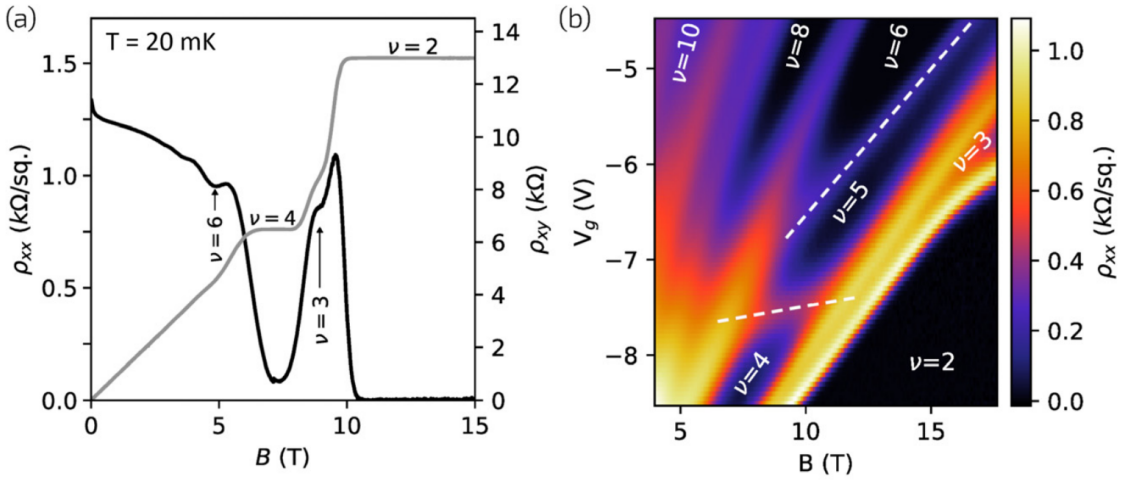


Figure 4.7: (a) SdH oscillations and quantum Hall plateaus at $V_g = -8.0$ V ($n_{2D} = 8.57 \times 10^{11}$ cm^{-2}); (b) Landau fan of SdH oscillations. The indicated filling factors were calculated from the Hall resistance. The dashed white lines indicate where the second subband populates the 2DEG. Reproduced from [18] with permission from AIP Publishing.

Unfortunately, in addition to Landau level broadening, there is significant evidence suggesting the presence of a second subband in the 2DEG. The first indicator is the "knee" in the pinch-off curve in Fig. 4.1(a), which indicates a change in the subband population.

The next is a discrepancy between the 2DEG density determined from the Hall effect versus that of the periodicity of the SdH oscillations (see Equation 3.13), with the latter being up to twice as small near $V_g = 0$. The onset of this discrepancy is at about $n_{2D} = 8 \times 10^{11}$ cm^{-2}, which suggests this is the density at which the second subband begins to populate the 2DEG. This value is in keeping with other work on 24 nm InAs/AlGaSb QWs [155, 156]. The Landau fan diagram in Fig. 4.7(b) also shows two regions of level crossing, further confirming the presence of a second subband. The presence of multiple subbands is not dire for future device applications, but does limit the operational range of gate voltages to below the onset of the second subband.

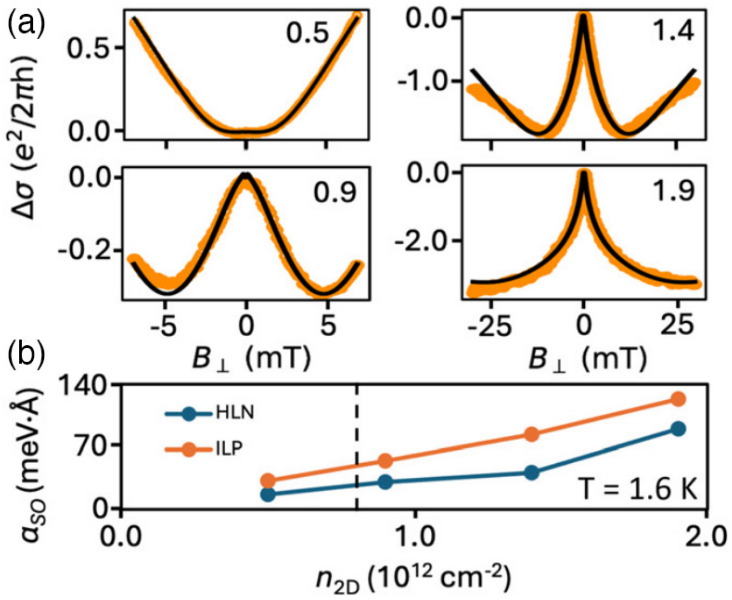


Figure 4.8: (a) Experimental WAL data (orange) fit to the ILP model (black). The 2DEG density ($\times 10^{12}$ cm^{-2}) for each plot is shown in the upper right. (b) Spin-orbit coefficient, extracted from both the HLN and ILP models, as a function of n_{2D}. The dotted line is where second-subband occupation is suspected to begin. Reproduced from [18] with permission from AIP Publishing.

WAL conductivity peaks were fit to both the HLN (Equation 3.14) and ILP (Equation 3.15) models to extract the spin-orbit coupling coefficient. The results provided values of α_{SO} ranging from 16 to 124 meV·Å – similar to values from other InAs/AlGaSb systems [31, 61, 143] – for values of n_{2D} ranging from 0.5 to 1.9 $\times 10^{12}$ cm^{-2}. While both fitting methods produce relatively linear plots, their efficacy is limited for these particular devices

(and others reported in the literature). Firstly, it is important to note that these points are not all in the single-subband regime. Most of the experimental points were obtained well beyond the onset of the second subband population, as shown in Fig. 4.8(b). Both the HLN and ILP models implicitly assume only single subband occupation, so the linearity of these fits must be viewed with some skepticism. Secondly, there is a threshold of applicability for both models; the fit is only accurate where $B < B_{tr} = \hbar/2el_e^2$, where B_{tr} is the transport field and l_e is the mean free path. The fourth WAL plot at $n_{2D} = 1.9 \times 10^{12}$ cm^{-2} requires data beyond this B_{tr} to be considered in the fitting method; therefore, the corresponding data point in the plot of α_{SO} is not necessarily accurate.

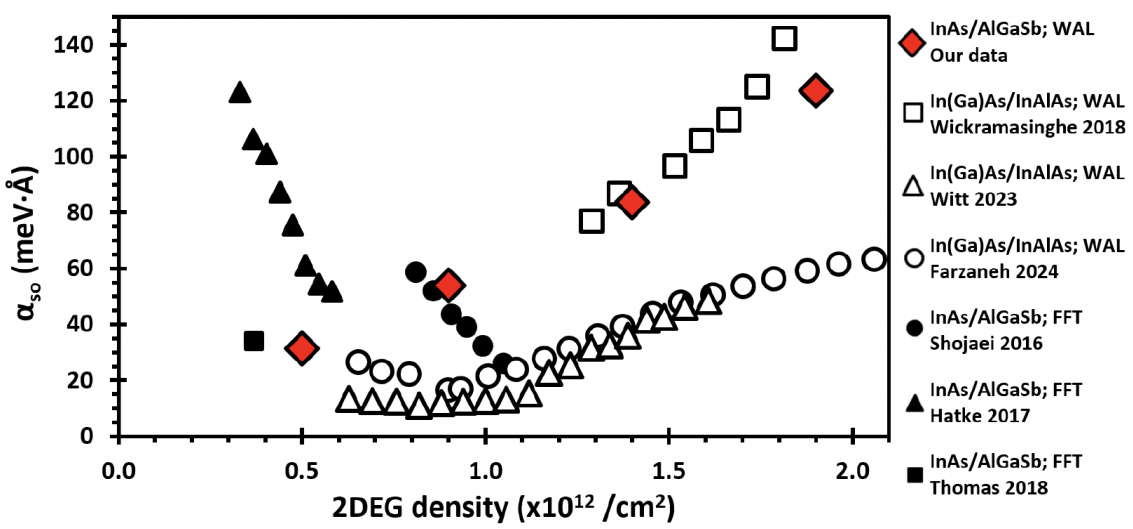


Figure 4.9: Our experimental WAL data compared to other values across the literature. Reproduced from [18] with permission from AIP Publishing.

When comparing the dependence of α_{SO} on the 2DEG density in our device and others in similar materials systems [44, 61, 143, 155, 165, 170], ours seems to contradict the trend. While InAs/AlGaSb QWs platforms tend to show an inverse relationship between α_{SO} and 2DEG density, our data more closely resembles the positive relationship seen in In(Ga)As/InAlAs systems. The discussion in Section 1.5.3 about the source of Rashba SOC – that is, structural inversion asymmetry (SIA) of the QW – leads us to our explanation of this behaviour. At densities where there is no net electric field across the QW (when $E_z = 0$), α_{SO} should be at its smallest. If one could sweep the gate voltage to an extensive range of densities, the shape of the density-versus-α_{SO} curve should be v-shaped. This phenomenon can be seen above for the data from Farzaneh et al. [44]. We hypothesize

that our $\alpha_{SO,min}$ is at a lower 2DEG density than other similar InAs/AlGaSb devices due to a different bandstructure profile due to our QWs being much closer to the surface of the device. Our data is, therefore, simply on the other side of the minimum.

4.3 15 nm Quantum Wells

A smaller InAs QW was chosen for these fabrication trials in an attempt to minimize multi-subband occupation. Two heterostructures (G1095 and G1120) with a 15 nm QW layer were grown using MBE. The growth layers are summarized in Table 4.3. Looking at the epitaxial layers, G1095 & G1120 may appear identical. However, G1120 has a smoother surface with less undulation than G1095, which can be more accurately described as "wire-like", or – colloquially – having "noodles." G1120 is thus anticipated to have higher electron mobility than its rougher G1095 counterpart. Instead of just varying the shutter sequence to create InSb-like interfaces here, the MBE team went one step further, intentionally growing one monolayer of InSb at the interface.

Layer	**G1095 & G1120**	
	Depth	Material
Cap	6 nm	$In_{0.75}Ga_{0.25}As$
QW	15 nm	InAs
Interface	0.3 nm	InSb
Bottom Barrier	20 nm	$Al_{0.8}Ga_{0.2}Sb$
Buffer	800 nm	$Al_{0.80}Ga_{0.20}Sb_{0.93}As_{0.07}$
Nucleation Layer	25 nm	GaSb
Substrate		GaSb (001)

Table 4.3: Summary of wafers with 15 nm wide InAs SQWs.

The first numerical analysis was performed on *bare*, or ungated, Hall bars. The results are summarized below in Table 4.4. Recall that the devices on G743 and G782 exhibited a two- to three-fold enhancement in electron density in the gated devices versus the ungated generation. This same effect is seen for device G1120. Comparing the bare Hall bars for G1095 and G1120, some enhancement in carrier mobility is seen; however, these two values are at drastically different Hall densities. Gated Hall bars must be used to compare these two wafers' transport characteristics rigorously. For reference, the mobility and density at $V_g = 0$ for a gated Hall bar on wafer G782 (24 nm, with an AlAs-like interface) are

also included. All the G1095 and G1120 devices have lower 2DEG densities at $V_g = 0$, perhaps because of some combination of the increased carriers donated from G782's AlAs-like interface and the lower density of states predicted for the smaller 15 nm QWs.

Hall bar ID	**Mobility** ($\times 10^4$ cm^2/Vs)	**2DEG density** ($\times 10^{12}$/cm^2)
G1095 (bare)	0.69	3.1
G1120 (bare)	0.98	1.9
G1120TG1C3	1.05	3.4
G782TG3SiO_2C2	0.75	3.1

Table 4.4: Mobilities measured on ungated Hall bars and one gated Hall bar on G1120 at $V_g = 0$. All measurements were taken at 1.6 K.

Pinch-off curves from -5 V to -9 V (after pinch-off) are shown for device G1120TG1C3 in Figure 4.10. Curves in each direction are well overlapped, though there is some hysteresis in the x (voltage) axis. This behaviour is consistent with the observations for the 24 nm devices fabricated with ALD SiO_2. It is worth noting that the voltage required to reach pinch-off (-8 to -8.5 V) is much lower than for the 24 nm QWs (approximately -14 V), which can be explained by the increased confinement in the narrower well (see Section 2.2.5).

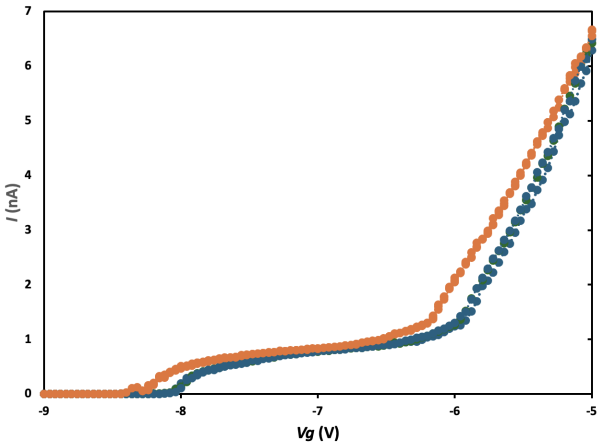


Figure 4.10: Pinch-off curve for G1120TG1C3. Three sweeps "up" (from -9 to -5 V) are shown in orange. Three sweeps "down" (from -5 to -9 V) are shown in blue.

The mobility-density relationships and gating characteristics of four different Hall bars

were measured and analyzed at 1.6 K (see Fig. 4.11). The peak electron mobilities of these devices were found between 1.72 to 1.88 $\times 10^4$ cm^2/Vs (average: 1.80×10^4 cm^2/Vs) at densities between 0.741 to 0.908 $\times$ 10^{12}/cm^2 (average: 0.818×10^{12}/cm^2) (see Table 4.5), corresponding to gate voltages between -4.1 to -4.5 V. These mobilities are a drastic ($\approx 1.6\times$) increase over previous wafers, and increased even further in the dilution refrigerator where the peak mobility of device G1120TG1C3 peaked at 2.11×10^4 cm^2/Vs. We hypothesize that this mobility increase is primarily due to the smoother surface morphology on G1120. Still, this hypothesis cannot be confirmed until a gated Hall bar on G1095 (the otherwise identical growth) can be fabricated and tested.

Hall bar ID	**Peak mobility** ($\times 10^4$ cm^2/Vs)	**2DEG density** ($\times 10^{12}$/cm^2)
G1120TG1C1	1.72	0.741
G1120TG1C2	1.88	0.766
G1120TG1C3	1.87	0.908
G1120TG1C5	1.74	0.857

Table 4.5: Peak mobilities measured on gated Hall bars at 1.6 K.

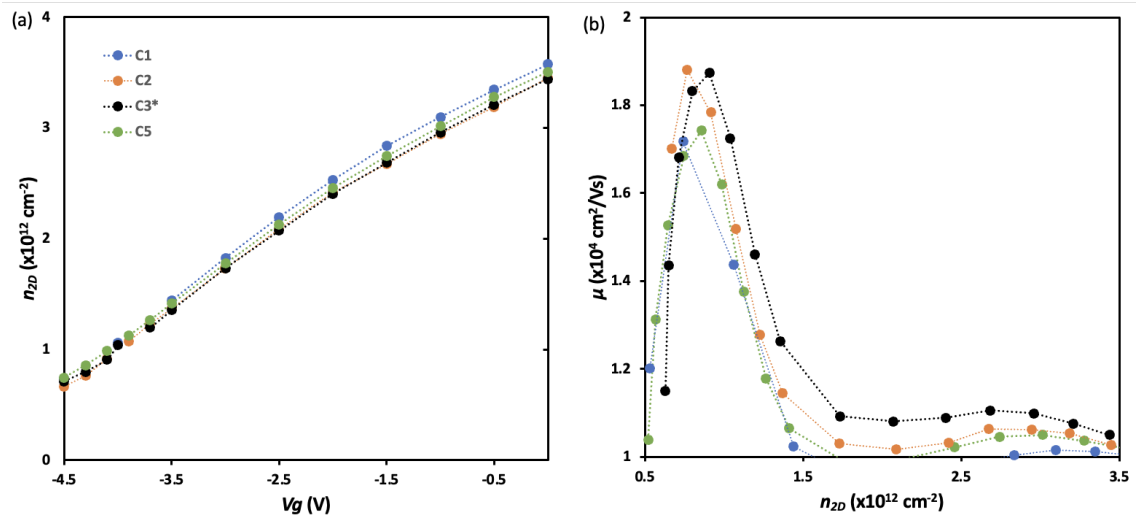


Figure 4.11: (a) Hall density vs top gate voltage and (b) mobility vs 2DEG density of all Hall bars at 1.6 K. C3 is the sample that was selected for further measurements on the dilution fridge.

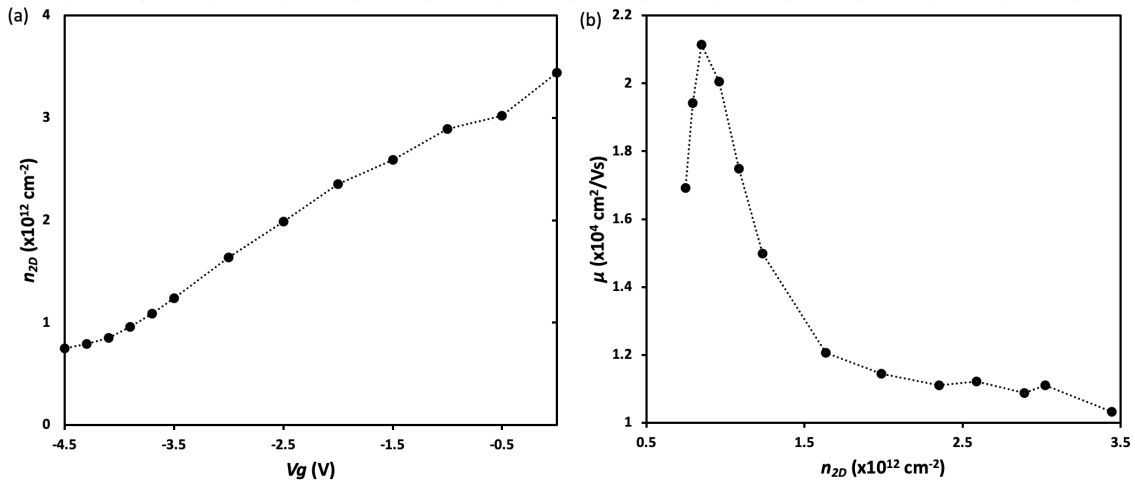


Figure 4.12: (a) Hall density vs top gate voltage and (b) mobility vs 2DEG density of device G1120TG1C3 at 22 mK. The mobility peak in (b) is 2.11×10^4 cm^2/Vs at 0.849×10^{12}/cm^2.

The SdH oscillations and quantum Hall plateaus measured on G1120 at peak mobility (Fig. 4.13) indicate that this wafer is less disordered than G743 & G782. The 2DEG density determined from the oscillations is $n_{2D} = 0.810 \times 10^{12}$/cm^2, a roughly 10% mismatch from the density determined from the Hall measurements. This difference suggests we did not drastically increase the onset of a second subband population from the 24 nm QWs. However, the first visible Hall plateau at $\rho_{xy} = 2.94$ kΩ corresponds to the *odd*-numbered filling factor $\nu = 9$. The onset of spin splitting, therefore, occurs at roughly 3.9 T, much earlier than for G743 or G782. The value of Γ, the Landau level broadening caused by disorder, is thus $\Gamma < g^*\mu_B B - k_B T \approx 3$ meV, much lower than the 9 meV for its 24 nm counterparts with rougher surfaces.

We plan to perform a full suite of transport measurements on gated Hall bars fabricated on both G1095 and G1120 to determine the cause of the increase in mobility and the impact of the smaller QW. These measurements include SdH and Hall effect measurements up to 18 T, analysis of the WAL, and detailed Landau fan diagrams.

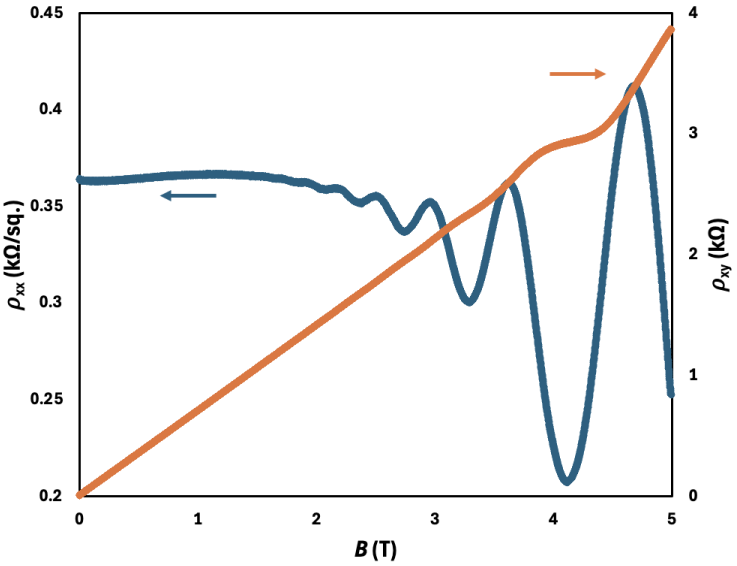


Figure 4.13: SdH oscillations and quantum Hall plateaus for device G1120TG1C3 at $Vg = -4.1$ V, corresponding to $n_{2D} = 0.908 \times 10^{12}/\text{cm}^2$. Measurements taken at 1.6 K.

Chapter 5

Proximitized superconducting devices on InAs/AlGaSb surface quantum wells

This chapter includes results and figures from the paper, "High transparency induced superconductivity in field effect two-dimensional electron gases in undoped InAs/AlGaSb surface quantum wells" [18] and its associated supplementary information. See the Statement of Contributions for more details.

5.1 Introduction

Though "epitaxial aluminum" – grown in-situ on In(Ga)As/InAlAs – is the most commonly used superconductor in semiconductor-superconductor devices, an ex-situ deposition method producing equally high-quality devices would open the door to more fabrication methods. We aimed to produce SNS devices using ex-situ Nb with comparable figures of merit to those fabricated by other groups using epitaxial Al. We used the same wafers described in the previous chapter, 24 nm surface quantum well devices in an InAs/$Al_{0.8}Ga_{0.2}Sb$ system, and created six ungated SNS devices.

5.2 Ungated SNS Devices

The six SNS devices investigated were fabricated on G743 and G782 using optical and electron beam lithography and wet-etching techniques at or below 180°C. Ohmic contact areas were Ar ion milled for 6.5 min at 50 W before the Ti/Nb (2/80 nm) contacts were deposited on the cap layer by sputtering. Before the Nb deposition, the chip underwent the sulphur passivation process described in Section 2.3.6. The dimensions of the devices are summarized below in Table 5.2. Devices with various gap lengths and widths were fabricated to encompass the short to long and diffusive to quasi-ballistic ranges (see Section 1.7). For these devices, the superconducting energy gap for niobium, with a critical temperature T_c of 8.1 K, is

$$\Delta_{Nb} = 1.76 k_b T_c = 1.23\text{meV}. \tag{5.1}$$

SNS-1 and SNS-2 are diffusive and short ($l_e < L < \xi_b$), SNS-3 and SNS-4 are quasi-ballistic and short ($L < l_e, \xi_b$), and SNS-5 and SNS-6 are diffusive and long ($L > l_e, \xi_b$). All the fabricated devices are in the dirty regime.

Wafer	n_{2D} ($\times 10^{12}$/cm^2)	μ ($\times 10^4$ cm^2/Vs)	k_F (nm^{-1})	v_F ($\times 10^6$ m/s)	l_e (nm)	ξ_b (nm)
G743	2.0	0.75	0.35	1.76	175	246
G782	1.6	1.17	0.32	1.60	244	220

Table 5.1: List of wafer properties used to determine the regimes of each device.

The four-terminal I-V traces (see setup in Fig. 5.1) for all six SNS devices confirm the presence of a superconducting gap. This gap is pictured in the lower inset of the I-V traces in Figs. 5.2 and 5.3 and is sharp and well-defined for the shorter junctions (SNS-1-4). The critical current I_c for each is noted in Table 5.2, and I_c is largest for SNS-1 and SNS-2 (the diffusive, short junctions) while it is the smallest for SNS-5 and SNS-6 (the diffusive, long junctions). The lack of hysteresis pictured in the upper insets of the I-V traces in Figs. 5.2 and 5.3 can likely be attributed to the samples and wiring being directly submerged in liquid ^{3}He/^{4}He in the dilution refrigerator, reducing the impact of local Joule heating effects [62, 163].

Examining the periodicity of multiple Andreev reflections (MAR) is the first step toward extracting figures of merit for SNS devices. Plots (Figs. 5.2(b,d,f) and 5.3(b,d,f)) of V_{dc} versus the four-terminal differential conductance $G = dI/dV$ normalized by the normal

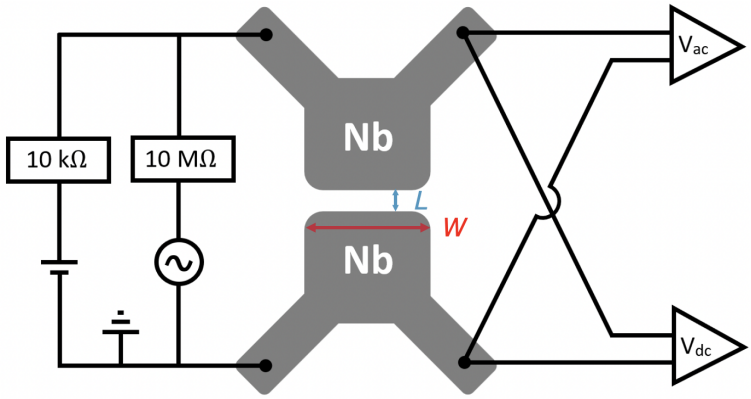


Figure 5.1: Four-terminal measurement setup for ungated SNS devices. The length L and width W are labelled. Adapted from [18] with permission from AIP Publishing.

conductance $G_N = 1/R_N$ show peaks at intervals of $eV_n = 2\Delta_{MAR}/n$ where n is an integer. As an example, the first three MAR peaks in the figure for SNS-4 (shown in more detail in Fig. 5.4) have a periodicity of $\Delta_{MAR} = 1.05$ meV; the rest are listed in Table 5.2. Only the first three peaks were included due to difficulty distinguishing later peaks closer to $V_{dc} = 0$. These values' uncertainty were determined using linear fit analysis (see Fig. 5.5). The average value of Δ_{MAR} for all six devices is 1.05 ± 0.02 meV, which compares relatively favourably to the theoretical value of $\Delta_{Nb} = 1.23$ meV. This amount of deviation is still consistent with high-quality SNS devices.

Device ID	Width (μm)	L (nm)	I_c (μA)	I_{ex} (μA)	R_N (Ω)	Δ_{MAR} (meV)	$\mathcal{T}$ (%)	Regime
SNS-1	10	200	82	158	8.8	1.13	78±5	diffusive, short, dirty
SNS-2	10	200	89	183	8.6	1.16	81±4	diffusive, short, dirty
SNS-3	3	120	29	58	30	1.13	85±2	quasi-ballistic, short, dirty
SNS-4	3	120	25	54	33	1.05	87±3	quasi-ballistic, short, dirty
SNS-5	3	400	5	24	53	0.91	82±2	diffusive, long, dirty
SNS-6	3	400	2	26	55	0.94	84±3	diffusive, long, dirty

Table 5.2: List of SNS devices, and their dimensions and measured properties. $\mathcal{T}$, the transparency, for each device was calculated using the OTBK model.

The two most commonly reported figures of merit for SNS devices are the ratio eI_cR_N/Δ_{MAR}, also known as the characteristic voltage, and the critical current density I_c/W. The product

I_cR_N can intuitively be described as the strength of the Cooper pair tunnelling across the junction [17]. The shorter junctions (SNS-1 through SNS-4) have ratios ranging from 0.64 to 0.79 and critical current densities from 8.2 to 9.6 $\mu A/\mu m$. These dramatically exceed the values typically reported for comparable planar In(Ga)As quantum wells with proximitized superconductivity from Nb: 0.02-0.15 and 0.3-1.6 $\mu A/\mu m$ [63, 111, 149]. These figures suggest very strong proximity-induced superconductivity in the devices' normal regions. Additionally, the critical current decreases in the transition from the short to long transport regime, indicating that the quality of these devices depends not only on the superconductor but also on the semiconductor in the gap region.

Base-temperature readings of SNS devices 1-6 produce transparencies, $\mathcal{T}$, between 78% to 87% (see Table 5.2) when calculated using the OTBK model (see Equations 3.24 and 3.25). Uncertainty values of the MAR periodicity are converted to uncertainty values on the transparency. These transparencies are on par with those reported using the OTBK model in epitaxial aluminum-In(Ga)As devices (between 75% to 97%) [88, 101, 66]. For thoroughness, the KO model (see Equation 3.26) with $T_c = 6.0$ K was also used to calculate the transparencies of SNS-1 and SNS-3, which produced values of $\mathcal{T} = 97.8\%$ and 99.5% respectively. These values are much higher than those of their OTBK counterparts. It is not straightforward to ascertain which method is more accurate; both are widely used and accepted models. The KO model may produce higher transparencies as it assumes no superconductivity in the "normal" regime; however, the Nb in our devices is still superconducting well into this regime. Either way, even at the most conservative estimate, these results demonstrate that using ex-situ deposited Nb is a promising avenue for creating devices with high interface transparency.

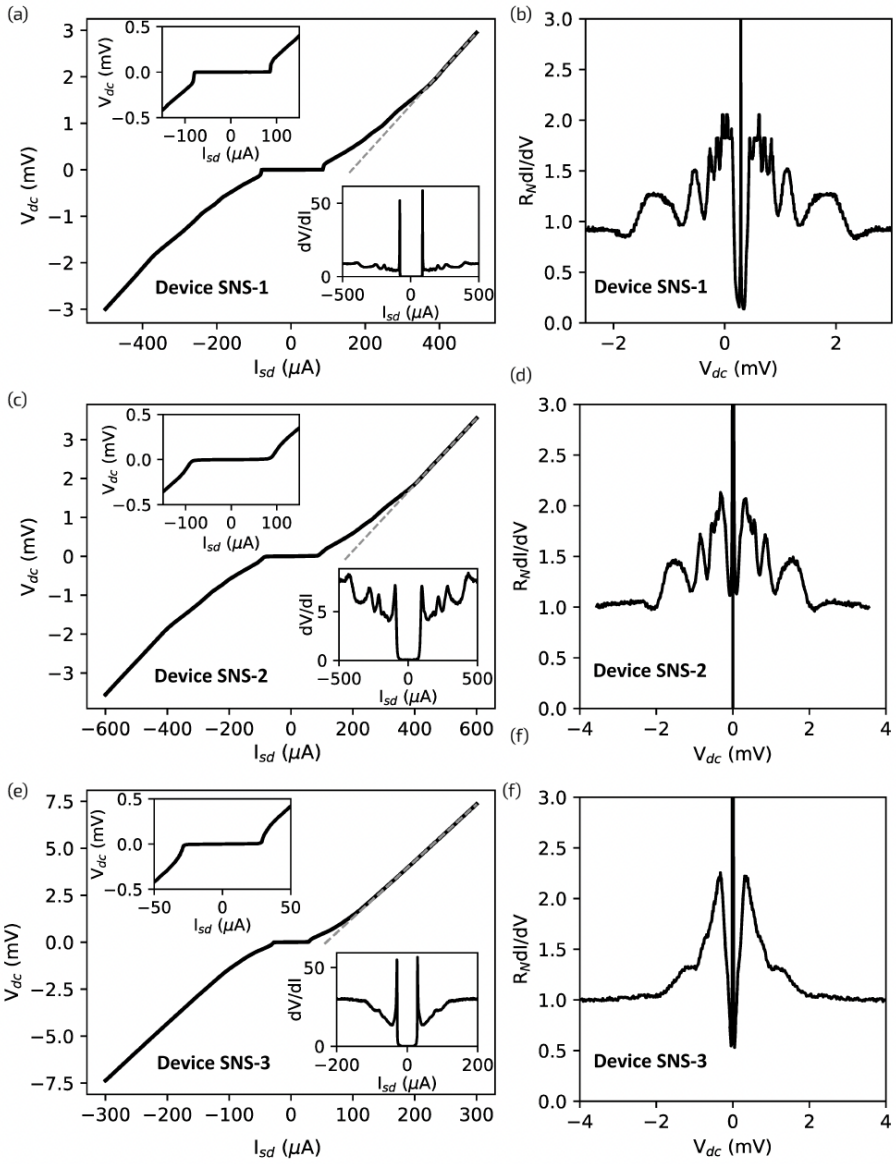


Figure 5.2: Data at 15 mK for devices: (a)-(b) SNS-1, (c)-(d) SNS-2, and (e)-(f) SNS-3. All panels on the left show DC four-terminal I-V traces of SNS junctions. All panels on the right show normalized AC four-terminal differential conductance dI/dV and MAR peaks. Reproduced from [18] with permission from AIP Publishing.

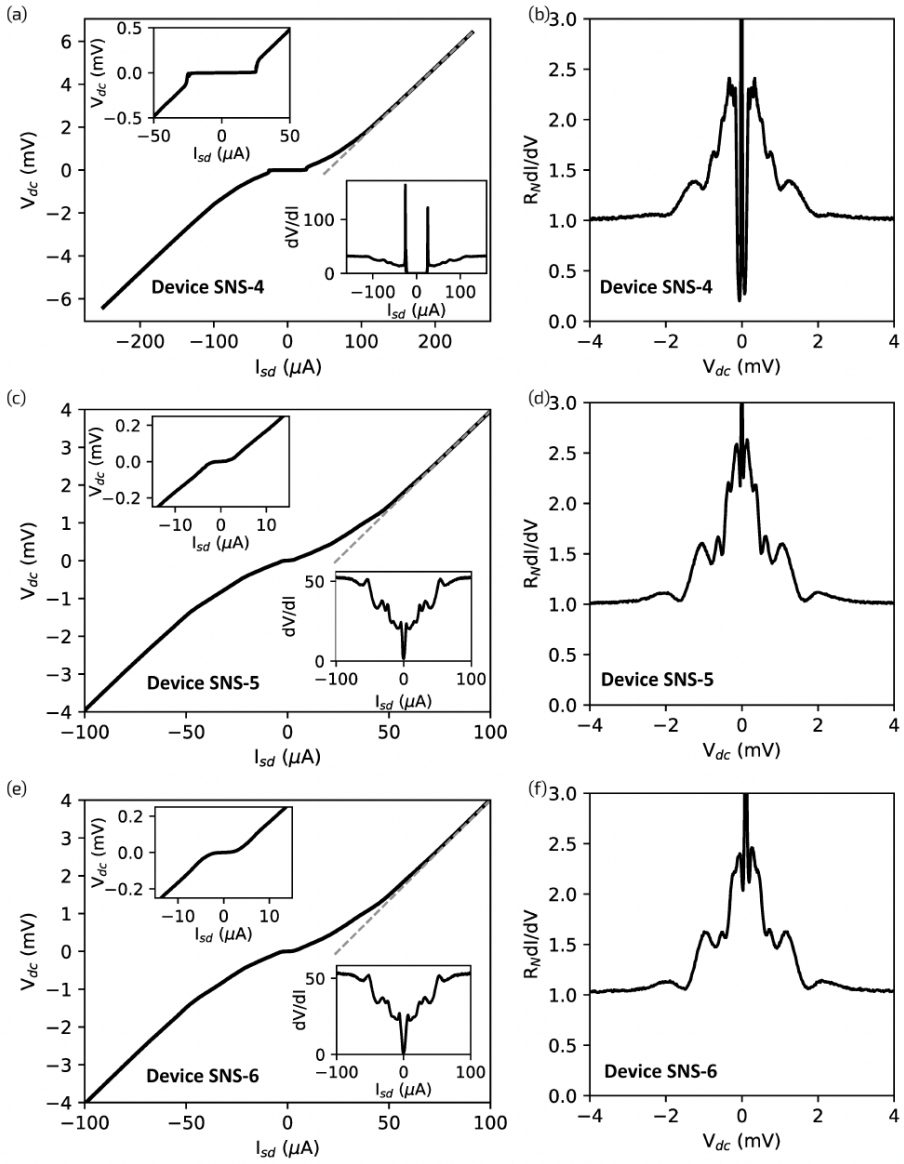


Figure 5.3: Data at 15 mK for devices: (a)-(b) SNS-4, (c)-(d) SNS-5, and (e)-(f) SNS-6. All panels on the left show DC four-terminal I-V traces of SNS junctions. All panels on the right show normalized AC four-terminal differential conductance dI/dV and MAR peaks. Reproduced from [18] with permission from AIP Publishing.

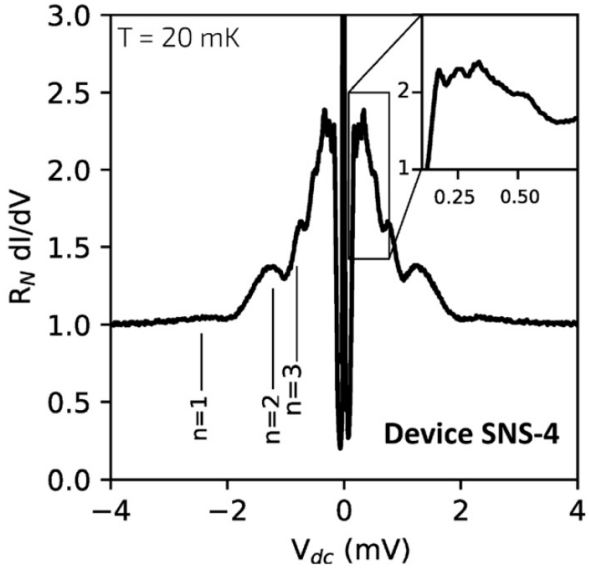


Figure 5.4: Fig. 5.3(b) with position of MAR peaks shown. Reproduced from [18] with permission from AIP Publishing.

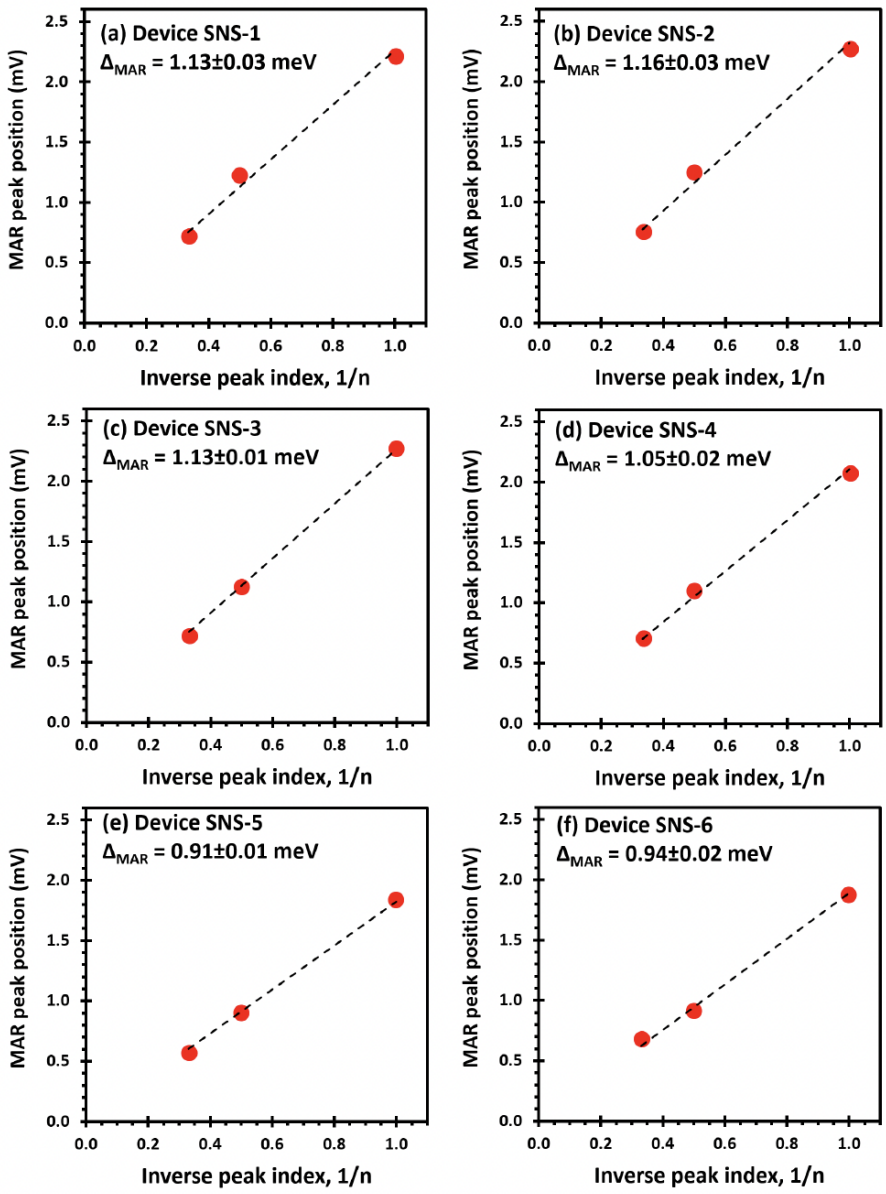


Figure 5.5: MAR peak positions (red circles) fit to $V_n = 2\Delta_{MAR}/e_n$, with individual fits (dashed lines) shown for the device: (a) SNS-1, (b) SNS-2, (c) SNS-3, (d) SNS-4, (e) SNS-5, and (f) SNS-6. The fit analysis determines the respective Δ_{MAR}. Reproduced from [18] with permission from AIP Publishing.

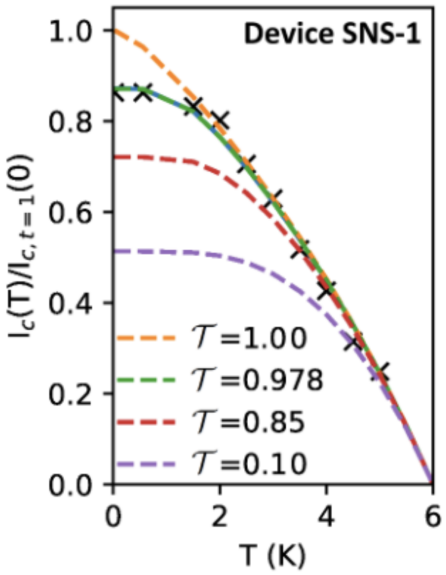


Figure 5.6: Temperature dependence of the critical current in SNS-1. The data was fit to multiple $\mathcal{T}$ (transparencies) to determine the most accurate value. Reproduced from [18] with permission from AIP Publishing.

5.3 Gated SNS Devices

For applications toward Majorana physics, field-effect gating is necessary to control the chemical potential in the device and move it into the topological regime. We therefore aim to fabricate a total of twenty-one SNS devices (seven on each of three mesas), all with width $W = 3$ μm and with lengths $L = 200$ nm (5/7 devices) and $L = 400$ nm (2/7 devices). These devices are being fabricated on wafer G837 due to its predictable gating characteristics, consistent mobility, and InSb-like interface. In the future, wafers with smooth surface morphologies like G1120 will likely be more ideal platforms.

Planned measurements include four-terminal I-V traces at multiple gate voltages and temperature and magnetic field dependence of the critical current (see Chapter 6). Our group previously analyzed the relationship between differential conductance and V_{dc} at various gate voltages for JJs fabricated on InSb SQW wafers [20]. Though these devices did not exhibit superconductivity, Andreev reflections did occur, and we could change the carrier density in the junction with field-effect gating. These results bode well for future devices and provide a valuable point of comparison.

5.4 Quantum Point Contacts

The keen-eyed reader may notice that, in Section 5.2, the superconducting gap is referred to as "sharp and well-defined," but not "hard." Devices using quantum point contacts (QPCs) as tunnel barriers can probe differential conductance, which can be used to decisively determine the hardness of the superconducting gap. These tunnel barriers can also be incorporated into future Majorana devices for a similar purpose (see Section 7.1). We plan to fabricate a total of forty QPC devices (eight on each of five mesas) with the following combination of dimensions:

Device type identifier	**Width (nm)**	**Length (nm)**
QPC1	300	250
QPC2	200	250
QPC3	300	150
QPC4	200	150

Table 5.3: Planned dimensions of QPC devices.

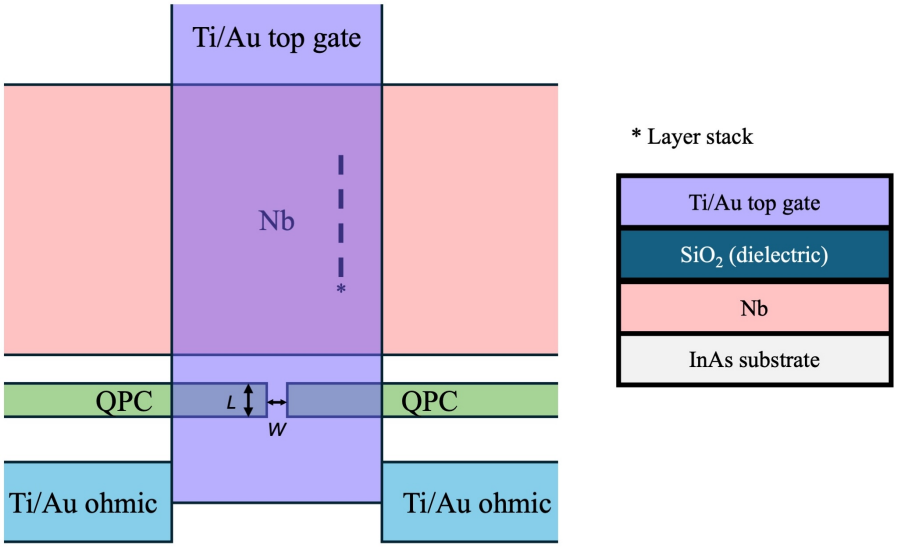


Figure 5.7: Schematic of the planned QPC devices. Not to scale. The width W and length L of the QPC are indicated in the figure.

These dimensions were chosen to maximize the chances of observing both superconductivity and quantized conductance following Equation 3.27. A key study by Markus Bttiker [26] provides a framework for predicting the limiting factors of quantized conductance in QPC devices. Between two quantum point contacts, the electrostatic potential forms a saddle shape (see Fig. 5.7), the curvatures of which are described by ω_x and ω_y. Near the saddle point and in the absence of any quantum tunnelling, the subband states $E_N < E_F$ will be occupied, where E_F is the Fermi level energy and

$$E_N = V_0 + \hbar\omega_y \left(N + \frac{1}{2} \right) \tag{5.2}$$

where $N = 0, 1, 2, 3...$ and V_0 is the electrostatic potential at the saddle (see Equation 3.7). $\hbar\omega_y$ can, therefore, be understood as describing the separation of the subbands in the potential well. $\hbar\omega_x$, on the other hand, is the width of the *transmission region* and defines the likelihood of transmission events. The study determined that clear conductance quantization occurs where $\omega_y \geq \omega_x$ (see Fig. 5.9); the separation between subband states must be larger than the transmission region.

We hope to fabricate devices in the short, quasi-ballistic regime to ensure both quantized conductance and superconductivity. This regime is also ideal for maximizing our chances of seeing a ZBCP in the future. Not all these device dimensions may function well; for

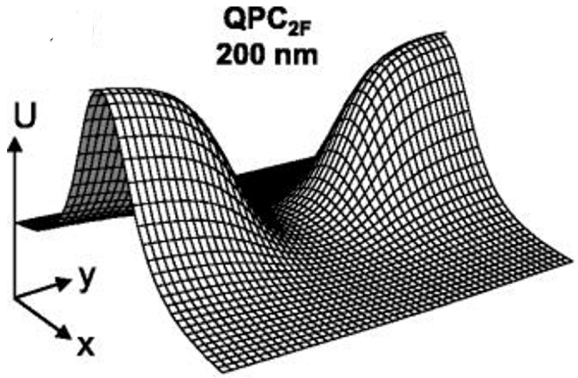


Figure 5.8: Simulation of the saddle-shape of the electrostatic potential V (here, U) in a GaAs/AlGaAs QPC with $L = 200$ nm and $W = 350$ nm. Reproduced from [74] with permission from AIP Publishing.

example, QPC4 may not exhibit quantized conductance, even if it is superconducting. Still, we are optimistic we can measure some of these devices successfully. Even if we are not in the ballistic regime, it is possible that we can still measure the normal and superconducting conductances to fulfill the requirements for superconducting hard-gap determination.

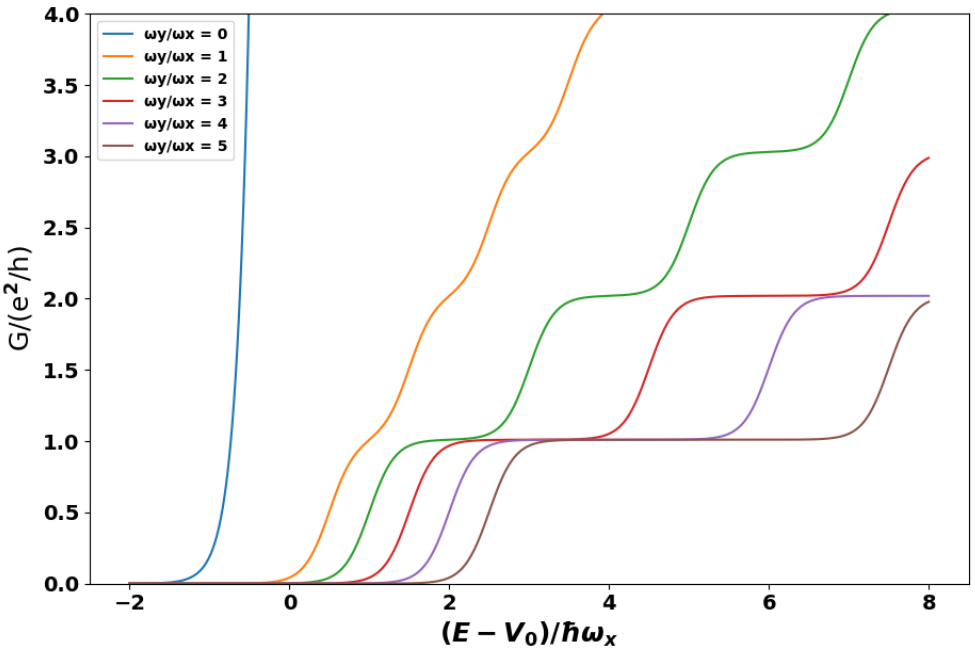


Figure 5.9: The dependence of the conductance through a QPC on $(E - V_0)/\hbar\omega_x$ at different values of ω_y/ω_x. The conductance is well-quantized at the larger values of ω_y/ω_x but decreases until there is no quantization when $\omega_y = 0$. Based on the work of Reference [26].

Chapter 6

Fraunhofer Diffraction Patterns

6.1 Introduction

The critical current I_c of a Josephson junction (JJ) depends on the applied magnetic field. Specifically, the critical current dependence takes the form of a *Fraunhofer* relation:

$$I_c = I_0 \left| \frac{\sin \pi f}{\pi f} \right| \tag{6.1}$$

where $f = \Phi/\Phi_0$ is the normalized flux, Φ_0 is the magnetic flux quantum $h/2e$, and I_0 is the total critical current of the junction when no magnetic field is applied [25]. In the case of a magnetic field with only the perpendicular component B_z ($B_x, B_y = 0$), the critical current as a function of magnetic field is:

$$I_c(B_z) = I_0 \left| \frac{\sin\left(\frac{\pi B_z A}{\Phi_0}\right)}{\frac{\pi B_z A}{\Phi_0}} \right| \tag{6.2}$$

where $A = LW$ is the area of the normal section of the SNS device, L is the "length" of the junction (from the point of view of the electrons), and W is the width.

Interestingly, the term *Fraunhofer diffraction* is typically used to describe the diffraction of plane waves when viewed in the far-field region. For a light source transmitting through a single slit, the definition of *far-field* is determined by the Fraunhofer condition, or when

$$\frac{a^2}{\lambda} \ll L \tag{6.3}$$

where a is the slit size, λ is the source wavelength, and L is the smaller of the following two distances: from source to slit or from slit to image. Below this limit, the diffraction can be described by *Fresnel* diffraction. For a single narrow slit, the intensity of the diffracted light is [125]

$$I = I_0 \left[\frac{\sin\left(\frac{\pi a}{\lambda} \sin\theta\right)}{\frac{\pi a}{\lambda} \sin\theta} \right]^2 \tag{6.4}$$

where I_0 is the incident light intensity and θ is the angle from the slit. The similarities between Equations 6.3 and 6.4 are evident when looking at a graphical comparison, where the Fraunhofer pattern in Equation 6.4 is simplified and defined as

$$F(x) = \left[\frac{\sin \pi x}{\pi x} \right]^2 \tag{6.5}$$

(see Figure 6.1).

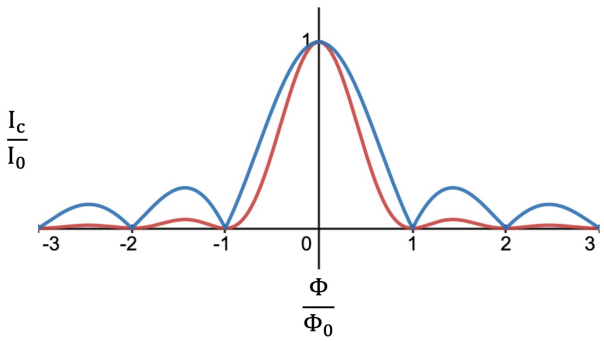


Figure 6.1: A comparison of the Fraunhofer-like JJ pattern in Equation 6.2 (blue) and the true Fraunhofer curve in Equation 6.5 (red).

To better understand this phenomenon intuitively, De Luca [38] imagines the SIS-type JJ depicted in Figure 6.2. If the net supercurrent along the path $A_1A_2B_1B_2$ is zero, the path-linked magnetic flux is

$$\Delta\Phi = \mu_0 H d \Delta y = \mu_0 H (t + \lambda_1 + \lambda_2)\Delta y \tag{6.6}$$

where $d = t + \lambda_1 + \lambda_2$ is the effective barrier thickness and λ_1 and λ_2 are the penetration depths into S_1 and S_2. The following relation arises from taking the path integral of the vector potential:

$$2\pi \frac{\Delta\Phi}{\Phi_0} = \phi(y + \Delta y) - \phi(y) \tag{6.7}$$

As Δy approaches zero,

$$\frac{2\pi}{L}\frac{\mu_0 H L d}{\Phi_0} = \frac{2\pi}{L}\frac{\Phi}{\Phi_0} = \frac{2\pi f}{L} = \frac{d\phi(y)}{dy} \tag{6.8}$$

The superconducting phase difference ϕ thus changes linearly with changes in y,

$$\phi(y) = ky + \phi_0 \tag{6.9}$$

where ϕ_0 is an unknown constant. The linear variation in phase is our first indication of Fraunhofer-like behaviour.

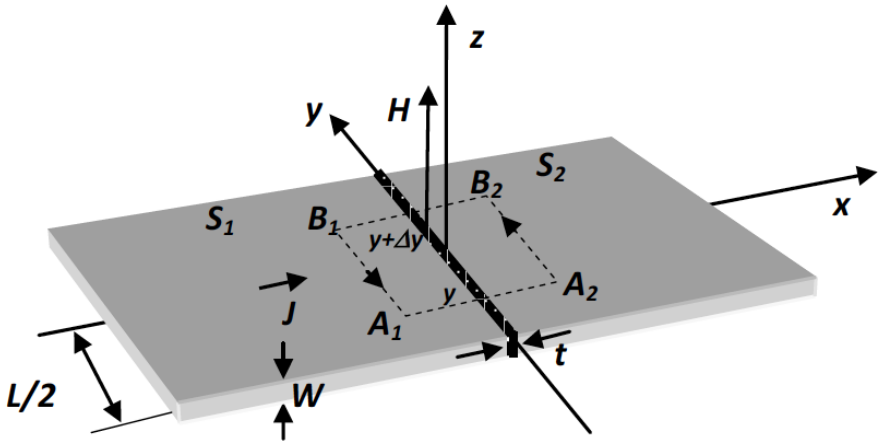


Figure 6.2: A JJ with insulating barrier of length L, width W, and thickness t. Here, the magnetic field is represented by H. Reproduced from [38] under Creative Commons license.

If the current density J is constant, the first Josephson equation $I = I_c \sin\phi$ (Equation 1.24) holds within an interval dy:

$$dI = JW \sin\phi(y)dy = JW \sin(ky + \phi_0)dy \tag{6.10}$$

Finally, integrating the above result over the junction barrier,

$$I = JWL\frac{\sin(\pi f)}{\pi f}\sin\phi_0 = I_0\frac{\sin(\pi f)}{\pi f}\sin\phi_0 \tag{6.11}$$

To find the critical current, the maximum of the above expression with respect to the superconducting phase difference ϕ_0 is:

$$I_c = I_0 \left| \frac{\sin(\pi f)}{\pi f} \right| \tag{6.12}$$

The Fraunhofer relation can also be understood in terms of a Fourier transform. The derivation below is recreated from Reference [54]. If a current

$$I = \iint J_s(y,z)dydz \tag{6.13}$$

flows through a JJ with an applied magnetic field $B_e = (0, B_y, 0)$, integration in the y-direction gives

$$i_c(z) = \int_{-W/2}^{W/2} J_c(y,z)dy. \tag{6.14}$$

The current as a function of B_y is thus

$$I(B_y) = \int_{-L/2}^{L/2} i_c(z)\sin(kz+\phi_0)dz \tag{6.15}$$

which can be written as a Fourier transform:

$$I(B_y) = \mathscr{F}\left\{ e^{i\phi_0} \int_{-\infty}^{\infty} i_c(z) e^{ikz} dz \right\} \tag{6.16}$$

the magnitude of which gives the critical current:

$$I_c(B_y) = \left| \int_{-\infty}^{\infty} i_c(z) e^{ikz} dz \right|. \tag{6.17}$$

6.2 Interpretation

Generally, the Fraunhofer diffraction pattern reflects the degree of supercurrent homogeneity. Qualitatively, it is an effective method to determine the quality of an SNS or SIS interface; a high-quality, transparent conventional JJ should have a predictable Fraunhofer pattern of the shape described above (or one involving some interference from multiple JJs). Quantitatively, the supercurrent density may be extracted from critical current measurements using the Fraunhofer-type relationship [59]. However, in cases where one or more key transport parameters are inhomogeneous, anomalous Fraunhofer patterns may arise. These unusual patterns provide insights into interesting quantum phenomena and material properties.

6.2.1 Sources of Anomalous Fraunhofer Patterns

Models predict Fraunhofer patterns with non-zero minima in systems with non-uniform magnetic susceptibility. For example, some rare earth metals such as holmium (Ho) and erbium (Er) have inhomogeneous magnetic induction when used in superconductor-ferromagnet-superconductor (SFS)-type JJs. This phenomenon is attributed to Ruderman-Kittel-Kasuya-Yosida (RKKY) coupling a mechanism whereby nuclear magnetic moments are coupled via conduction electrons being enhanced in the bulk relative to at edges, leading to increased local magnetic susceptibility [25].

One possible source of anomalous patterns is relevant to our devices: strong SOC has been demonstrated to break some fundamental Fraunhofer pattern symmetries. Typically, the critical current does not depend on the polarity of either the magnetic field or current; changes to these factors will not impact the shape of the pattern. Formally [43],

$$I_c^{\pm}(B_z) = I_c^{\pm}(-B_z) \tag{6.18}$$

$$I_c^{+}(B_z) = -I_c^{-}(B_z). \tag{6.19}$$

However, there are numerous recent reports [13, 33, 43, 175] of systems with strong Rashba SOC, Dresselhaus SOC, or both that break these symmetries, as has been previously theorized [22, 129]. The currently accepted explanation for the anomalous pattern produced by strong SOC is that the current-phase relation of ABSs at the interfaces take on a non-zero phase shift, so $I(-\phi) \neq -I(\phi)$ [33].

In the case of InAs devices, models for the impact of SOC do not tend to be rigorous enough to predict the shape of the diffraction pattern. A proposed theoretical model by Bezuglyi et al. [22] explains the collective impact of SOC and Zeeman coupling on the Josephson current. One takeaway from this model is that the effect of the SOC is likely somewhat dependent on the magnetic field orientation. More recent work suggests that the Fraunhofer pattern should remain symmetric irrespective of current polarity without an in-plane magnetic field component [13]. This is taken to be true for the analysis of simulated and experimental patterns in later sections of this chapter where only B_z is present. Unfortunately, these predictions are imperfect; for example, the potentially drastic impact of flux focusing and other microscopic properties such as disorder may "mask" any effects resulting from SOC [147]. Further research in this area is needed if a predictive model is the ultimate goal, especially as researchers continue investigating the complex interplay between SOC and Zeeman coupling contributing to the formation of MBSs.

6.2.2 In Pursuit of Majorana Bound States

Topological surface states are another one of the many explanations for anomalous Fraunhofer patterns. As a possible explanation for their asymmetrical observations, Fan et al. [43] suggest the presence of topological behaviour. If there are different Josephson currents on either side of the JJ due to the presence of topological surface states, this could break these same mirror symmetries. Unfortunately, it is difficult to distinguish between these possible causes, as topological asymmetry occurs in systems with strong SOC.

Similarly, Ghatak et al. [52] observed anomalous patterns in SIS-type JJs with inhomogeneous supercurrents on the topological insulator's surface. Over the entire range of gate voltages, the researchers found missing and suppressed Fraunhofer peaks not previously predicted, in addition to small periods (smaller-than-anticipated ΔB_{avg}). Originally, anomalous periodicity in comparable JJs made from topological insulators was tentatively hypothesized to be caused by Majorana bound states themselves [168]; however, Ghatak et al. provide alternative explanations. Instead, they attribute the periodicity to a two-dimensional superfluid in the aluminum electrodes in combination with the flux-focusing effect: a distortion in the magnetic field near the superconducting electrodes. The missing and suppressed maxima in the Fraunhofer pattern are theorized to result from inhomogeneous supercurrent distribution rather than non-sinusoidal current-phase relations caused by MBSs.

Pribiag et al. [126] provide a more complete picture of the behaviour of two-dimensional topological insulators compared to conventional SNS junctions. The researchers analyzed the behaviour of InAs/GaSb devices and found that conventional SNS junctions produced Fraunhofer-like results, incorporating a topological insulator that induced different results. If the Fermi level is in the bulk bands, the behaviour is Fraunhofer-like. If it is in the topological gap and crosses the helical edge modes produced on the TI, the SQI measurement produces a function more closely resembling that of a SQUID (see Figure 6.3). Finally, the measurement more closely resembles the Fraunhofer pattern when the Fermi level enters the valence band. This result clarifies the understanding of the tuning of bulk and edge-mode superconductivity and provides more insight into how the Fraunhofer pattern can be used to understand JJ behaviour. At the end of the paper, when faced with an interesting $2\Phi_0$ periodicity over a specific gate range, the authors theorize it could be caused by MBSs causing the fractional Josephson effect, where lone electrons rather than Cooper pairs tunnel across the junction. However, they acknowledge the need for future research in this area and do not claim this phenomenon as a definite signature of topological behaviour.

These discussions echo many others in Majorana physics: How do we know if we have found a MBS? So far, anomalous Fraunhofer patterns have not provided an answer to this

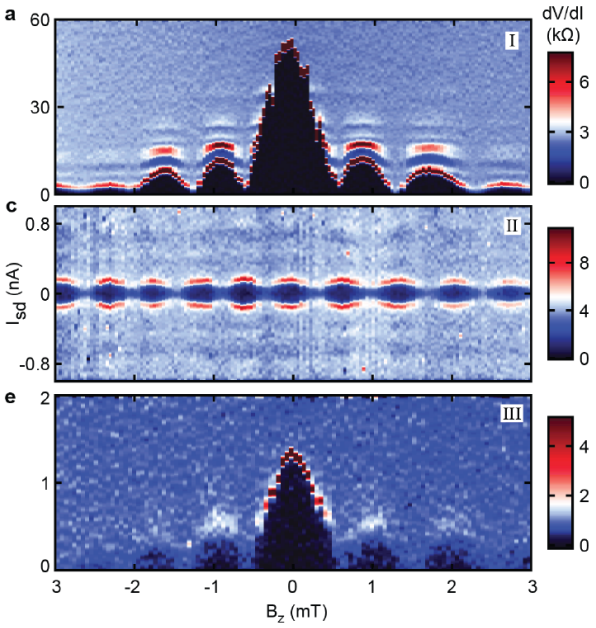


Figure 6.3: Superconducting quantum interference (SQI) measurements where (a) the Fermi level is in one of the bulk bands, (c) the Fermi level is in the topological gap, and (e) the Fermi level is in the valence band. Reproduced from [126] with permission from Springer Nature.

question and do not qualify as a Majorana signature. However, high-quality JJs are often a necessary experimental step in research dedicated to finding MBSs. Given newer research into SOC and its influence on Fraunhofer patterns and the predictability of these patterns in more conventional systems, analysis of critical current and its magnetic field dependence is a powerful experimental tool in this area.

6.3 Simulations

Analyzing critical current relationships may help determine the quality of the SNS devices described in Chapter 5. The first step towards this goal is producing graphs representing the expected Fraunhofer diffraction patterns from junctions of different sizes using Equation 6.5. However, several complex factors impact the effective normal area depending on the superconductors used. Firstly, Equation 6.6 defines the length of a junction as

$$d = t + \lambda_1 + \lambda_2 \tag{6.20}$$

where $\lambda_{1,2}$ are the London penetration depths (how far the magnetic field penetrates the superconductor) of the superconducting areas. This conventional definition can be simplified to $d = L + 2\lambda$ for the symmetrical JJ pictured in Figs. 5.1 and 6.4. Assouline et al. [11] propose what may be a more accurate definition for λ in the case of a perpendicular magnetic field and a device with flux focusing, dubbed λ_z:

$$\lambda_z = \lambda_{eff} \coth\left(\frac{d}{\lambda_{eff}}\right) \tag{6.21}$$

where d is the superconducting layer thickness and

$$\lambda_{eff} = \lambda_L \sqrt{1 + \frac{\xi}{l}} \tag{6.22}$$

where l is the mean free path of the superconducting layer and ξ, the coherence length of the bulk superconductor, is [147]

$$\xi = \frac{h\nu_F}{\pi\Delta} \tag{6.23}$$

where the superconducting gap $\Delta_{Nb} = 1.23$ meV. For best accuracy, this value should be the coherence length in the thin film limit [147],

$$\xi_{thin} = \xi_{bulk} \frac{T_{c,bulk}}{T_{c,thin}}. \tag{6.24}$$

Relevant values for the Nb used in our system are summarized in Table 6.1. Note that the mean free path of the superconducting layer is thickness-dependent; this value is for 80 nm of Nb, as in our devices.

The same paper additionally accounts for flux focusing by introducing a A_{eff} term (see Figure 6.4):

$$I_c(B_z) = I_0 \left| \frac{\sin\left(\frac{\pi B_z A_{eff}}{\Phi_0}\right)}{\frac{\pi B_z A_{eff}}{\Phi_0}} \right| \tag{6.25}$$

where $A_{eff} = A + A_{foc}$ and

$$A_{foc} = 2\left(\frac{W}{2} - \lambda_z\right)^2. \tag{6.26}$$

This formula is mathematically equivalent to the model devised by Gu et al. for niobium electrodes [56] if L is taken to be the actual (not effective) junction length. Following

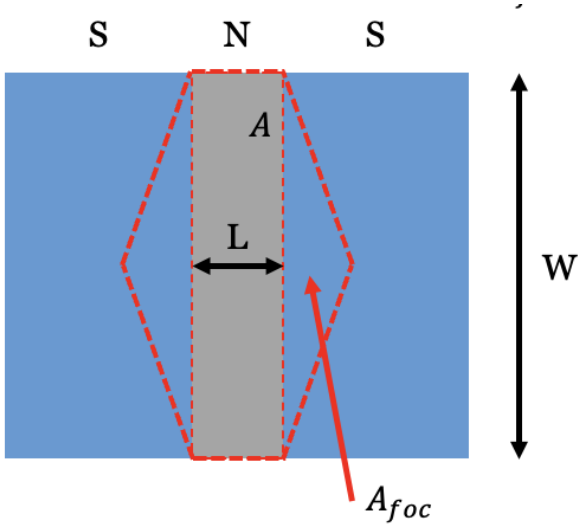


Figure 6.4: The SNS device with a correction to the effective magnetic field, or effective area of the normal region. The red dotted area represents the flux-focusing correction proposed in Reference [11].

Reference [58], which studied diffusive Nb/n-InAs/Nb SNS junctions, the magnetic field term B_{app} is corrected to the effective field B_{eff},

$$B_{eff} = \alpha \left(\frac{2W}{L}\right)^{\frac{2}{3}} B_{app} \tag{6.27}$$

where the prefactor α can be adjusted to produce a better fit; in the paper cited, they used a value of $\alpha = 0.66$. This model was used in this reference for devices with $W_{Nb} = 12$ μm and $L = 220$ nm to 700 nm, nearly encompassing the range of our devices.

Simulations using Python (code included in Appendix A) were performed for junctions with the dimensions fabricated in Chapter 5. To compare different methods to account for flux focusing effects, three plots were generated for devices of each dimension: (1) with $d = L + 2\lambda$; (2) with $d = L + 2\lambda_z$; and (3) with $A = A_{eff}$. For adjustment (3), α was assumed to be 1. The period of each pattern under each set of adjustments, ΔB_{1-3}, is summarized in Table 6.2.

It is immediately apparent that the impact of the junction width is disproportionately large for the adjustment methods in Equations 6.26 or 6.27. In the case of SNS-1 and SNS-2, with $W = 10$ μm, the magnetic field enhancement $\gamma = \alpha \left(\frac{2W}{L}\right)^{(2/3)}$ is 21.54 if $\alpha = 1$; this implies an enormous impact of flux focusing on the critical current. The effect

Variable	Definition	Value used
λ_L	London penetration depth of bulk superconductor	39 nm
l	Mean free path of superconducting layer	9 nm
T_c	Critical temperature of the superconductor	9 K
v_F	Fermi velocity	1.37×10^6 m/s
d	Superconducting layer thickness	80 nm
λ_{eff}	Effective penetration depth for electrodes	89 nm
ξ	Coherence length of bulk superconductor	38 nm
λ_z	Overall penetration depth (from flux focusing)	125 nm

Table 6.1: Constants used for Fraunhofer simulations. Values sourced from [124] (rows 1-4) or calculated (rows 5-8).

Device	ΔB_1 (mT)	ΔB_2 (mT)	ΔB_3 (mT)
SNS-1 & SNS-2 $L = 200$ nm, $W = 10$ μm	0.75	0.46	0.04
SNS-3 & SNS-4 $L = 120$ nm, $W = 3$ μm	3.48	1.87	0.50
SNS-5 & SNS-6 $L = 400$ nm, $W = 3$ μm	1.44	1.06	0.42

Table 6.2: Periodicity of the Fraunhofer pattern for each device geometry under each adjustment; accurate to two decimal places.

appears more reasonable for devices with smaller widths. Of course, α need not be unity; other studies using Nb and InAs devices [58, 108] use $\alpha \approx 0.7$ and find more well-matching periodicities. For measurements on our devices, α must be determined experimentally. Future research in this area will hopefully clarify the physical phenomena that impact the magnitude of α.

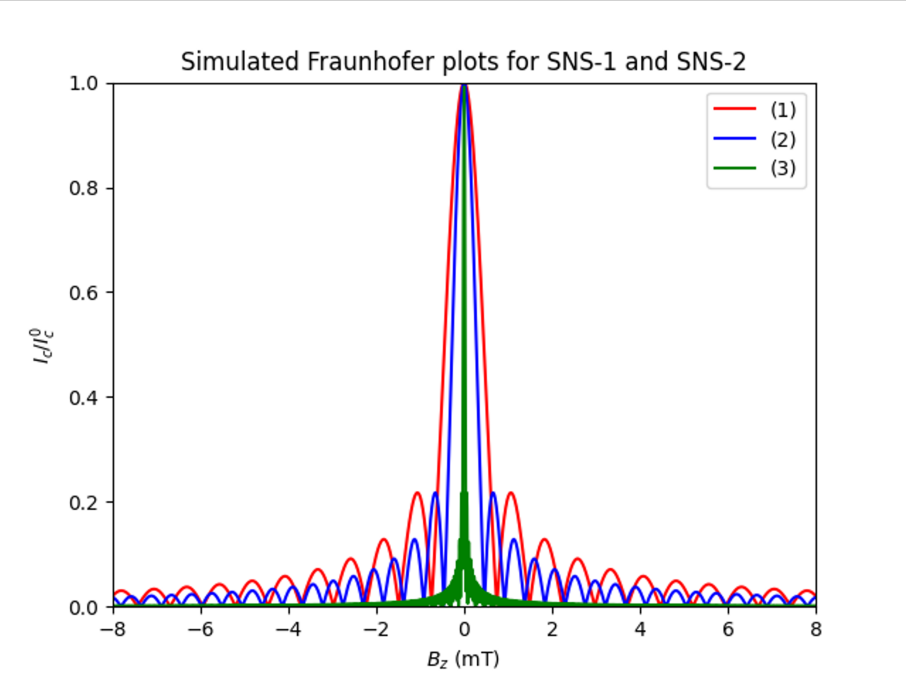


Figure 6.5: Simulation of the Fraunhofer diffraction pattern for SNS-1 and SNS-2 with various adjustments: (1) with $d = L + 2\lambda$; (2) with $d = L + 2\lambda_z$; and (3) with $A = A_{eff}$.

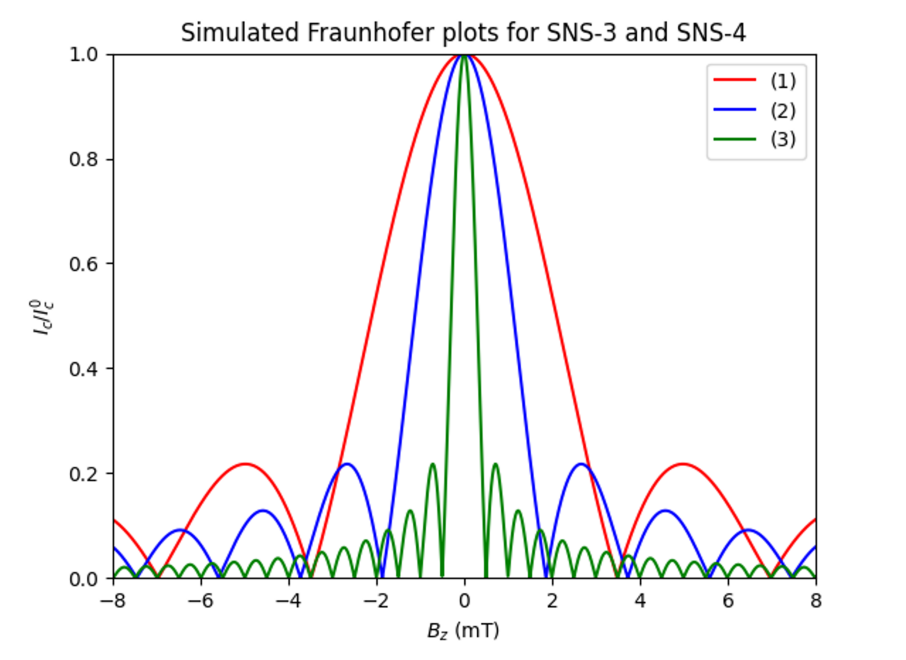


Figure 6.6: Simulation of the Fraunhofer diffraction pattern for SNS-3 and SNS-4 with various adjustments: (1) with $d = L + 2\lambda$; (2) with $d = L + 2\lambda_z$; and (3) with $A = A_{eff}$.

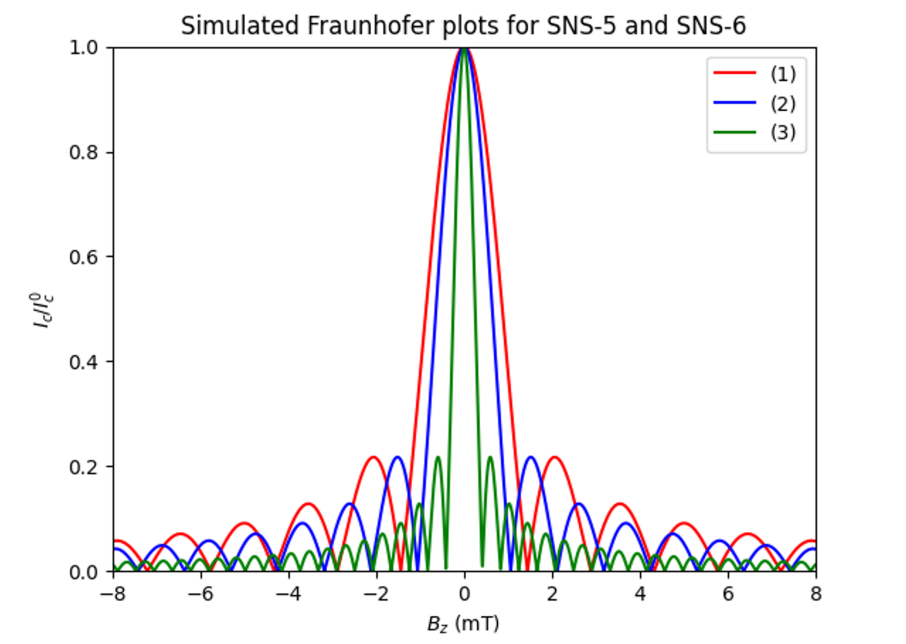


Figure 6.7: Simulation of the Fraunhofer diffraction pattern for SNS-5 and SNS-6 with various adjustments: (1) with $d = L + 2\lambda$; (2) with $d = L + 2\lambda_z$; and (3) with $A = A_{eff}$.

6.4 Measurements

Unfortunately, our ability to measure the critical current at such small magnetic fields is severely limited by our equipment. The Nb_3Sn magnet on the dilution refrigerator is too noisy at $B \approx 0$ to do detailed Fraunhofer experiments at the small fields required. On the other hand, the superconductivity of our devices tends to be weaker on our cryostat (1.6 K) than on the much colder dilution refrigerator. Due to the much lower experimental time overhead for the cryostat, we decided to begin there, attempting a measurement on SNS-1 (see Section 5.2). A coarse first sweep resulted in the plot in Figure 6.8. We did attempt a finer sweep on this device and increased the range of V_{sd} to ensure we captured the entire central antinode, but the device, unfortunately, did not recover its previous behaviour. The quality of these experimental results can likely be improved by increasing the measurement resolution and using a magnet and magnet power source with less noise near zero field.

Extracting quantitative data from Figure 6.8 is unrealistic, but some qualitative information can be gained. The first is that there are approximately five or six nodes visible on each side of the central antinode on this plot from $B = -8$ mT to $B = 8$ mT, which would give a very rough periodicity of $\Delta B_{avg} = 1.5$ mT. This number is drastically higher than even the simulation that did not account for flux focusing (Curve 1), suggesting there is some factor at play to *decrease* the effective magnetic field. This phenomenon is as of yet unexplained but is likely just a result of the coarseness of our measurement. The calculated critical current at zero field, I_c°, compares more favourably. If the central antinode is very roughly extrapolated to reach its maximum at $V_{sd} = 120$ mV, this would correspond to $I_c^\circ = 120mV/10k\Omega = 12\mu$A. This value is somewhat larger than I-V curves taken during the same cool-down would seem to indicate ($I_c^\circ \approx 6\mu$A), but that can again presumably be explained by the lack of precision of this particular Fraunhofer measurement run. Ultimately, future work on this project should and will investigate this effect further. We plan to attempt more detailed measurements of the upcoming generation of gated SNS devices, incorporating the improvements to resolution and magnet choice as discussed.

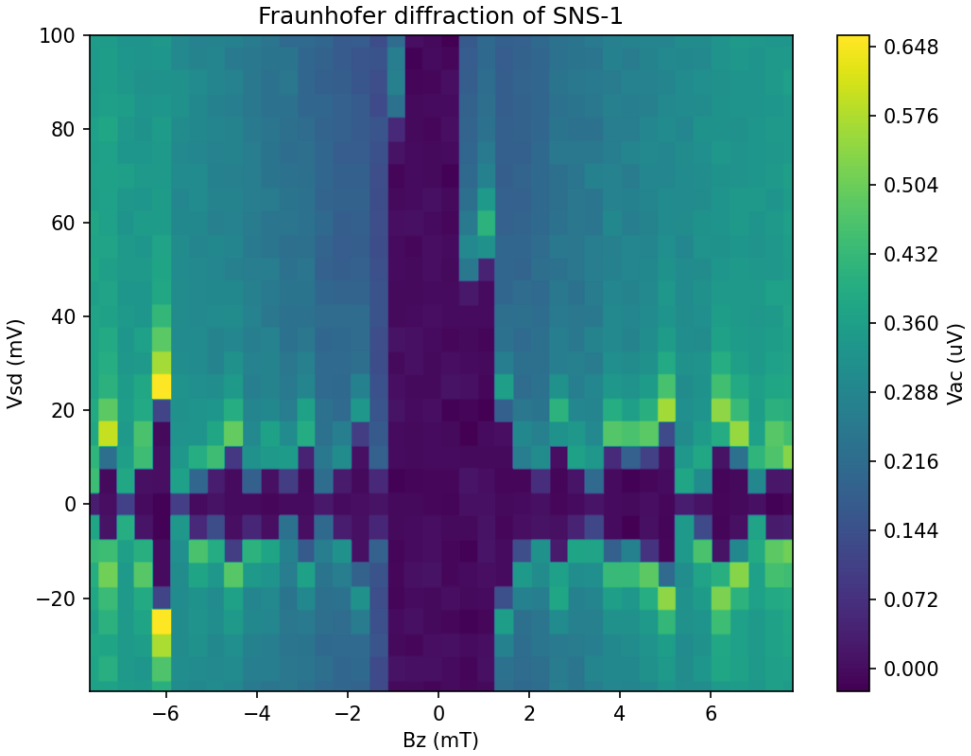


Figure 6.8: Measured dependence of V_{sd} versus V_{ac} on magnetic field.

Chapter 7

Outlook & Conclusion

7.1 Majorana Devices

All the work performed in the leadup to writing this thesis has one common goal: to develop and improve the materials systems and devices that form integral parts of a future Majorana device. Our proposed design for a first attempt at observing Majorana physics is described in Section 1.5.4. One advantage of this device is its compatibility with the topological gap protocol (TGP). The TGP is an experimental and statistical process developed by Microsoft Quantum to determine whether a ZBCP at the end of a 1D channel will likely be in the topological phase. The first stage, where local conductance measurements are performed at RF, finds where the ZBCPs are observed at both ends of the 1D channel and groups these ZBCPs into regions of interest. The second stage involves calculating the full conductance matrix:

$$G = \begin{pmatrix} G_{RR} & G_{RL} \\ G_{LR} & G_{LL} \end{pmatrix} = \begin{pmatrix} dI_R/dV_R & dI_R/dV_L \\ dI_L/dV_R & dI_L/dV_L \end{pmatrix} \tag{7.1}$$

at DC frequencies, determining which regions of interest are likely caused by topological phenomena.

The efficacy of this protocol is still a matter of some debate. Sergey Frolov and Vincent Mourik, some of the earliest experimentalists researching MBSs and additionally notable for their role in exposing fraudulent research practices in the field [50], expressed concern about the original preprint article and also suggest that gap reopening and closing is insufficient to prove the presence of MBSs [49]. Additionally, other leading researchers, Richard Hess et al. [67], demonstrated that there are circumstances under which trivial

phenomena may pass the TGP. I argue that this protocol must be applied more widely and across a more extensive range of device types to determine its potential utility, and our device design is a compatible candidate for this critical future work on reproducibility.

7.2 Other Applications

Though the possibility of a Majorana device is the driving force behind this project, the research done along the way has other potential device applications. Field-effect transistors (FETs) have long been the basis of the semiconductor industry and rely on the same physical principles as our top-gated 2DEG devices. The idea of using an InAs SNS device to create a superconducting FET is not new [89]. However, at the time of these innovations, the Fermi level pinning in InAs posed significant challenges to effective gating [150], and metal-insulator-semiconductor field-effect transistors (MISFETs) and metal-oxide-semiconductor field-effect transistors (MOSFETs) became the leading technologies instead. More recently, now that researchers better understand the interplay between the field and proximity effects [120], the possibility of Josephson junction (JJ)-FETs has come back into focus [117]. Our devices, with their excellent interface transparencies, may be ideal candidates for this application.

Braiding operations are also not the only way these devices may apply to quantum computing. Those same JJ-FETs [117] or similar device architectures [27, 146] may be useful as *gatemon* qubits, a variation of charge qubit that can be controlled by gates. These technologies will likely be developed in tandem with topological quantum computing applications and may find their own commercial use.

7.3 Conclusions

This thesis represents the most recent in a series of essential innovations in materials science and device design on the path to topological quantum computing. Thorough assessments of indium arsenide surface quantum well (SQW) wafer properties clarified the importance of gate dielectric materials, interface properties, and surface morphology. 24 nm surface quantum wells with high mobilities of approximately 1.2×10^4 cm^2/Vs and 15 nm devices with even higher mobilities up to 2.1×10^4 cm^2/Vs were fabricated and analyzed, with both series of devices exhibiting the quantum Hall effect and reliable I-V and gating characteristics. The 24 nm quantum well devices were also found to have large spin-orbit coupling

coefficients up to 124 meV·Å. These wafers are an excellent foundation for more complex future steps.

In our proximitized superconducting superconductor-normal-superconductor (SNS) devices, our group demonstrated – for the first time – that ex-situ deposited niobium can be an equally effective parent superconductor as epitaxial aluminum, with interface transparencies on par with the current state-of-the-art devices (between 78%-99.5%). These six devices all conducted supercurrents, a testament to the reproducibility of our results, and the smaller four have deep, well-defined superconducting gaps. Other figures of merit for our devices are also much higher than all previously reported In(Ga)As SNS devices using niobium. Early stages of measurements investigating the critical current dependence on magnetic field are an exciting opportunity to probe the complicated relationships between the fundamental requirements for our proposed method of creating Majorana bound states: superconductivity, spin-orbit coupling, and applied Zeeman fields. Right now, in the nanofabrication facility, we are adding top gates to these same devices and developing quantum point contacts (QPCs) to enrich our understanding of the superconducting properties at play. I anticipate that the work described in this thesis and our group's future research will accelerate the field's progress toward its ultimate goals: braiding experiments, topological qubits, and inherently fault-tolerant quantum computing.

Letters of Copyright Permission

License Number	5814070255685
License date	Jun 22, 2024

Printable Details

Licensed Content

Licensed Content Publisher	Springer Nature
Licensed Content Publication	Nature Physics
Licensed Content Title	Observation of a one-dimensional spin–orbit gap in a quantum wire
Licensed Content Author	C. H. L. Quay et al
Licensed Content Date	Mar 21, 2010

Order Details

Type of Use	Thesis/Dissertation
Requestor type	academic/university or research institute
Format	print and electronic
Portion	figures/tables/illustrations
Number of figures/tables/illustrations	1
Would you like a high resolution image with your order?	no
Will you be translating?	no
Circulation/distribution	1 - 29
Author of this Springer Nature content	no

About Your Work

Title of new work	Proximity superconductivity in two-dimensional electron gas devices: A step towards scalable topological quantum computing
Institution name	University of Waterloo
Expected presentation date	Aug 2024

Additional Data

Portions	Figure 1 a-c
The Requesting Person / Organization to Appear on the License	Fiona Thompson

Requestor Location

Requestor Location	University of Waterloo 200 University Ave Waterloo, ON N2L 3G1 Canada Attn: Fiona Thompson

Tax Details

Reuse permission for Fig. 1.7.

License Number	5814931226192
License date	Jun 23, 2024

Printable Details

Licensed Content

Licensed Content Publisher	Springer Nature
Licensed Content Publication	Nature Reviews Materials
Licensed Content Title	Bandgap engineering in semiconductor alloy nanomaterials with widely tunable compositions
Licensed Content Author	Cun-Zheng Ning et al
Licensed Content Date	Oct 31, 2017

Order Details

Type of Use	Thesis/Dissertation
Requestor type	academic/university or research institute
Format	print and electronic
Portion	figures/tables/illustrations
Number of figures/tables/illustrations	1
Would you like a high resolution image with your order?	no
Will you be translating?	no
Circulation/distribution	1 - 29
Author of this Springer Nature content	no

About Your Work

Title of new work	Proximity superconductivity in two-dimensional electron gas devices: A step towards scalable topological quantum computing
Institution name	University of Waterloo
Expected presentation date	Aug 2024

Additional Data

Portions	Figure 1
The Requesting Person / Organization to Appear on the License	Fiona Thompson

Requestor Location

Requestor Location	University of Waterloo 200 University Ave Waterloo, ON N2L 3G1 Canada Attn: University of Waterloo

Tax Details

Reuse permission for Fig. 1.10.

License Number	5846571152258
License date	Aug 12, 2024

Printable Details

Licensed Content

Licensed Content Publisher	Springer Nature
Licensed Content Publication	Journal of Low Temperature Physics
Licensed Content Title	New Measurements of Wetting by Helium Mixtures
Licensed Content Author	Ryosuke Ishiguro et al
Licensed Content Date	Dec 31, 1969

Order Details

Type of Use	Thesis/Dissertation
Requestor type	academic/university or research institute
Format	print and electronic
Portion	figures/tables/illustrations
Number of figures/tables/ illustrations	1
Will you be translating?	no
Circulation/distribution	1 - 29
Author of this Springer Nature content	no

About Your Work

Title of new work	Proximity Superconductivity in Indium Arsenide Two-Dimensional Electron Gas Devices
Institution name	University of Waterloo
Expected presentation date	Aug 2024

Additional Data

Portions	Figure 12
The Requesting Person / Organization to Appear on the License	Fiona Thompson

Requestor Location

Requestor Location	University of Waterloo 200 University Ave W Waterloo, ON N2L 3G1 Canada Attn: University of Waterloo

Tax Details

Reuse permission for Fig. 3.1.

Licensed Content

Licensed Content Publisher	AIP Publishing
Licensed Content Publication	Applied Physics Letters
Licensed Content Title	High transparency induced superconductivity in field effect two-dimensional electron gases in undoped InAs/AlGaSb surface quantum wells
Licensed Content Author	Bergeron, E. Annelise; Sfigakis, F.
Licensed Content Date	May 29, 2024
Licensed Content Volume	124
Licensed Content Issue	22

Order Details

Type of Use	Thesis/Dissertation
Requestor type	Author (original article)
Format	Print and electronic
Portion	Figure/Table
Number of figures/tables	4
Will you be translating?	No

About Your Work

Title of new work	Proximity superconductivity in two-dimensional electron gas devices: A step towards scalable topological quantum computing
Institution name	University of Waterloo
Expected presentation date	Aug 2024

Additional Data

Portions	All figures and tables
The Requesting Person / Organization to Appear on the License	Fiona Thompson

Requestor Location

Requestor Location	University of Waterloo 181 King St S Unit 1806 Waterloo, ON N2J 0E7 Canada Attn: University of Waterloo

Tax Details

Reuse permission for Figs. 3.2, 4.1, 4.2, 4.3, 4.7, 4.8, 4.9, 5.1, 5.2, 5.3, 5.4, 5.5, & 5.6.

License Number	5846250478006
License date	Aug 11, 2024

Printable Details

Licensed Content

Licensed Content Publisher	AIP Publishing
Licensed Content Publication	Journal of Applied Physics
Licensed Content Title	Split-gate quantum point contacts with tunable channel length
Licensed Content Author	Iqbal, M. J.; de. Jong, J. P.
Licensed Content Date	Jan 10, 2013
Licensed Content Volume	113
Licensed Content Issue	2

Order Details

Type of Use	Thesis/Dissertation
Requestor type	Student
Format	Print and electronic
Portion	Figure/Table
Number of figures/tables	1
Will you be translating?	No

About Your Work

Title of new work	Proximity Superconductivity in Indium Arsenide Two-Dimensional Electron Gas Devices
Institution name	University of Waterloo
Expected presentation date	Aug 2024

Additional Data

Portions	Figure 2(a)
The Requesting Person / Organization to Appear on the License	Fiona Thompson

Requestor Location

Requestor Location	University of Waterloo 200 University Ave W Waterloo, ON N2L 3G1 Canada Attn: University of Waterloo

Tax Details

Reuse permission for Fig. 5.7.

License Number	5846590900000
License date	Aug 12, 2024

Printable Details

Licensed Content

Licensed Content Publisher	Springer Nature
Licensed Content Publication	Nature Nanotechnology
Licensed Content Title	Edge-mode superconductivity in a two-dimensional topological insulator
Licensed Content Author	Vlad S. Pribiag et al
Licensed Content Date	May 11, 2015

Order Details

Type of Use	Thesis/Dissertation
Requestor type	academic/university or research institute
Format	print and electronic
Portion	figures/tables/illustrations
Number of figures/tables/illustrations	1
Would you like a high resolution image with your order?	no
Will you be translating?	no
Circulation/distribution	1 - 29
Author of this Springer Nature content	no

About Your Work

Title of new work	Proximity Superconductivity in Indium Arsenide Two-Dimensional Electron Gas Devices
Institution name	University of Waterloo
Expected presentation date	Aug 2024

Additional Data

Portions	Fig. 4 a,c,e
The Requesting Person / Organization to Appear on the License	Fiona Thompson

Requestor Location

Requestor Location	University of Waterloo 200 University Ave W Waterloo, ON N2L 3G1 Canada Attn: Fiona Thompson

Tax Details

Reuse permission for Fig. 6.3.

References

[1] Alfred R. Adams. Strained-Layer Quantum-Well Lasers. *IEEE Journal of Selected Topics in Quantum Electronics*, 17(5):1364–1373, September 2011.

[2] R Ainsworth and J K Slingerland. Topological qubit design and leakage. *New Journal of Physics*, 13(6):065030, June 2011.

[3] Anton Akhmerov, Jay Sau, Bernard van Heck, Sebastian Rubbert, Rafa Skolasiski, Bas Nijholt, Irfan Muhammad, and Tmas rn Rosdahl. Online course on topology in condensed matter. https://topocondmat.org/index.html, 2021.

[4] S. M. Albrecht, A. P. Higginbotham, M. Madsen, F. Kuemmeth, T. S. Jespersen, J. Nygrd, P. Krogstrup, and C. M. Marcus. Exponential Protection of Zero Modes in Majorana Islands. *Nature*, March 2016.

[5] Jason Alicea. Majorana fermions in a tunable semiconductor device. *Physical Review B - Condensed Matter and Materials Physics*, 81(12), March 2010.

[6] Robert Alicki, Michał Horodecki, Alejandro Jenkins, Marcin Łobejko, and Gerardo Suarez. The josephson junction as a quantum engine. *New Journal of Physics*, oct 2023.

[7] Carl D. Anderson. The Positive Electron. *Physical Review*, 43(6):491–494, March 1933.

[8] Tsuneya Ando, Alan B. Fowler, and Frank Stern. Electronic properties of two-dimensional systems. *Rev. Mod. Phys.*, 54:437–672, Apr 1982.

[9] G. Anton, I. Badhrees, P.S. Barbeau, D. Beck, V. Belov, T. Bhatta, M. Breidenbach, T. Brunner, G.F. Cao, W.R. Cen, C. Chambers, B. Cleveland, M. Coon, A. Craycraft, T. Daniels, M. Danilov, L. Darroch, S.J. Daugherty, J. Davis, S. Delaquis, A. Der

Mesrobian-Kabakian, R. DeVoe, J. Dilling, A. Dolgolenko, M.J. Dolinski, J. Echevers, W. Fairbank, D. Fairbank, J. Farine, S. Feyzbakhsh, P. Fierlinger, D. Fudenberg, P. Gautam, R. Gornea, G. Gratta, C. Hall, E.V. Hansen, J. Hoessl, P. Hufschmidt, M. Hughes, A. Iverson, A. Jamil, C. Jessiman, M.J. Jewell, A. Johnson, A. Karelin, L.J. Kaufman, T. Koffas, R. Krcken, A. Kuchenkov, K.S. Kumar, Y. Lan, A. Larson, B.G. Lenardo, D.S. Leonard, G.S. Li, S. Li, Z. Li, C. Licciardi, Y.H. Lin, R. MacLellan, T. McElroy, T. Michel, B. Mong, D.C. Moore, K. Murray, O. Njoya, O. Nusair, A. Odian, I. Ostrovskiy, A. Piepke, A. Pocar, F. Retire, A.L. Robinson, P.C. Rowson, D. Ruddell, J. Runge, S. Schmidt, D. Sinclair, A.K. Soma, V. Stekhanov, M. Tarka, J. Todd, T. Tolba, T.I. Totev, B. Veenstra, V. Veeraraghavan, P. Vogel, J.-L. Vuilleumier, M. Wagenpfeil, J. Watkins, M. Weber, L.J. Wen, U. Wichoski, G. Wrede, S.X. Wu, Q. Xia, D.R. Yahne, L. Yang, Y.-R. Yen, O.Ya. Zeldovich, T. Ziegler, and EXO-200 Collaboration. Search for Neutrinoless Double-β Decay with the Complete EXO-200 Dataset. *Physical Review Letters*, 123(16):161802, October 2019.

[10] George B. Arfken, Hans J. Weber, and Frank E. Harris. Vector Analysis. In *Mathematical Methods for Physicists*, pages 123–203. Elsevier, 2013.

[11] Alexandre Assouline, Cheryl Feuillet-Palma, Nicolas Bergeal, Tianzhen Zhang, Alireza Mottaghizadeh, Alexandre Zimmers, Emmanuel Lhuillier, Mahmoud Eddrie, Paola Atkinson, Marco Aprili, and Herv Aubin. Spin-Orbit induced phase-shift in Bi2Se3 Josephson junctions. *Nature Communications*, 10(1):126, January 2019.

[12] R. Balian and N. R. Werthamer. Superconductivity with Pairs in a Relative p Wave. *Physical Review*, 131(4):1553–1564, August 1963.

[13] Christian Baumgartner, Lorenz Fuchs, Andreas Costa, Simon Reinhardt, Sergei Gronin, Geoffrey C. Gardner, Tyler Lindemann, Michael J. Manfra, Paulo E. Faria Junior, Denis Kochan, Jaroslav Fabian, Nicola Paradiso, and Christoph Strunk. Supercurrent rectification and magnetochiral effects in symmetric Josephson junctions. *Nature Nanotechnology*, 17(1):39–44, January 2022.

[14] C. W. J. Beenakker. Quantum transport in semiconductor-superconductor microjunctions. *Phys. Rev. B*, 46:12841–12844, Nov 1992.

[15] C. W. J. Beenakker. Annihilation of Colliding Bogoliubov Quasiparticles Reveals their Majorana Nature. *Physical Review Letters*, 112(7):070604, February 2014.

[16] C. W. J. Beenakker. Search for non-Abelian Majorana braiding statistics in superconductors. *SciPost Physics Lecture Notes*, page 15, August 2020.

[17] M. Belogolovskii, E. Zhitlukhina, V. Lacquaniti, N. De Leo, M. Fretto, and A. Sosso. Intrinsically shunted Josephson junctions for electronics applications. *Low Temperature Physics*, 43(7):756–765, July 2017.

[18] E. Annelise Bergeron, F. Sfigakis, A. Elbaroudy, A. W. M. Jordan, F. Thompson, George Nichols, Y. Shi, Man Chun Tam, Z. R. Wasilewski, and J. Baugh. High transparency induced superconductivity in field effect two-dimensional electron gases in undoped InAs/AlGaSb surface quantum wells. *Applied Physics Letters*, 124(22):222103, May 2024.

[19] E. Annelise Bergeron, F. Sfigakis, Y. Shi, George Nichols, P. C. Klipstein, A. Elbaroudy, Sean M. Walker, Z. R. Wasilewski, and J. Baugh. Field effect two-dimensional electron gases in modulation-doped InSb surface quantum wells. *Applied Physics Letters*, 122(1):012103, January 2023.

[20] Emma Annelise Bergeron. *Development of III-V Semiconductor Surface Quantum Wells for Hybrid Superconducting Device Applications*. PhD thesis, University of Waterloo, 2023.

[21] V. N. Bessolov and M. V. Lebedev. Chalcogenide passivation of IIIV semiconductor surfaces. *Semiconductors*, 32(11):1141–1156, November 1998.

[22] E. V. Bezuglyi, A. S. Rozhavsky, I. D. Vagner, and P. Wyder. Combined effect of Zeeman splitting and spin-orbit interaction on the Josephson current in a superconductortwo-dimensional electron gassuperconductor structure. *Physical Review B*, 66(5):052508, August 2002.

[23] N. N. Bogoljubov. On a new method in the theory of superconductivity. *Il Nuovo Cimento*, 7(6):794–805, March 1958.

[24] Parsa Bonderson, Michael Freedman, and Chetan Nayak. Measurement-Only Topological Quantum Computation. *Physical Review Letters*, 101(1):010501, June 2008. arXiv:0802.0279 [cond-mat, physics:hep-th, physics:quant-ph].

[25] B. Brcsk, S. Komori, A. I. Buzdin, and J. W. A. Robinson. Fraunhofer patterns in magnetic Josephson junctions with non-uniform magnetic susceptibility. *Scientific Reports*, 9(1):5616, April 2019.

[26] M. Bttiker. Quantized transmission of a saddle-point constriction. *Physical Review B*, 41(11):7906–7909, April 1990.

[27] Lucas Casparis, Malcolm R. Connolly, Morten Kjaergaard, Natalie J. Pearson, Anders Kringhj, Thorvald W. Larsen, Ferdinand Kuemmeth, Tiantian Wang, Candice Thomas, Sergei Gronin, Geoffrey C. Gardner, Michael J. Manfra, Charles M. Marcus, and Karl D. Petersson. Superconducting gatemon qubit based on a proximitized two-dimensional electron gas. *Nature Nanotechnology*, 13(10):915–919, October 2018.

[28] W. Chang, S. M. Albrecht, T. S. Jespersen, F. Kuemmeth, P. Krogstrup, J. Nygrd, and C. M. Marcus. Hard gap in epitaxial semiconductor-superconductor nanowires. *Nature Nanotechnology*, November 2014.

[29] J. Chen, B. D. Woods, P. Yu, M. Hocevar, D. Car, S. R. Plissard, E. P. A. M. Bakkers, T. D. Stanescu, and S. M. Frolov. Ubiquitous non-majorana zero-bias conductance peaks in nanowire devices. *Phys. Rev. Lett.*, 123:107703, Sep 2019.

[30] A. Chrestin, T. Matsuyama, and U. Merkt. Evidence for a proximity-induced energy gap in Nb/InAs/Nb junctions. *Physical Review B*, 55(13):8457–8465, April 1997.

[31] Yoon Jang Chung, K. A. Villegas Rosales, K. W. Baldwin, P. T. Madathil, K. W. West, M. Shayegan, and L. N. Pfeiffer. Ultra-high-quality two-dimensional electron systems. *Nature Materials*, 20(5):632–637, May 2021.

[32] William S. Cole, S. Das Sarma, and Tudor D. Stanescu. Effects of large induced superconducting gap on semiconductor majorana nanowires. *Phys. Rev. B*, 92:174511, Nov 2015.

[33] A. Costa, C. Baumgartner, S. Reinhardt, J. Berger, S. Gronin, G. C. Gardner, T. Lindemann, M. J. Manfra, J. Fabian, D. Kochan, N. Paradiso, and C. Strunk. Sign reversal of the Josephson inductance magnetochiral anisotropy and 0pi-like transitions in supercurrent diodes. *Nature Nanotechnology*, 18(11):1266–1272, November 2023.

[34] Van-Truong Dai, Sheng-Di Lin, Shih-Wei Lin, Yi-Shan Lee, Yin-Jie Zhang, Liang-Chen Li, and Chien-Ping Lee. High-quality planar light emitting diode formed by induced two-dimensional electron and hole gases. *Optics Express*, 22(4):3811, February 2014.

[35] Anindya Das, Yuval Ronen, Yonatan Most, Yuval Oreg, Moty Heiblum, and Hadas Shtrikman. Zero-bias peaks and splitting in an AlInAs nanowire topological superconductor as a signature of Majorana fermions. *Nature Physics*, 8(12):887–895, December 2012.

[36] Sankar Das Sarma, Michael Freedman, and Chetan Nayak. Majorana zero modes and topological quantum computation. *npj Quantum Information*, 1(1):15001, October 2015.

[37] Sankar Das Sarma, Jay D. Sau, and Tudor D. Stanescu. Splitting of the zero-bias conductance peak as smoking gun evidence for the existence of the Majorana mode in a superconductor-semiconductor nanowire. *Physical Review B*, 86(22):220506, December 2012.

[38] Roberto de Luca. Quantum Interference in Josephson Junctions. *Journal of Modern Physics*, 06(05):526–535, 2015.

[39] Michiel W A De Moor, Jouri D S Bommer, Di Xu, Georg W Winkler, Andrey E Antipov, Arno Bargerbos, Guanzhong Wang, Nick Van Loo, Roy L M Op Het Veld, Sasa Gazibegovic, Diana Car, John A Logan, Mihir Pendharkar, Joon Sue Lee, Erik P A M Bakkers, Chris J Palmstrm, Roman M Lutchyn, Leo P Kouwenhoven, and Hao Zhang. Electric field tunable superconductor-semiconductor coupling in Majorana nanowires. *New Journal of Physics*, 20(10):103049, October 2018.

[40] Paul Adrien Maurice Dirac and Ralph Howard Fowler. The quantum theory of the electron. *Proceedings of the Royal Society of London. Series A, Containing Papers of a Mathematical and Physical Character*, 117(778):610–624, 1928. _eprint: https://royalsocietypublishing.org/doi/pdf/10.1098/rspa.1928.0023.

[41] A. C. C. Drachmann, H. J. Suominen, M. Kjaergaard, B. Shojaei, C. J. Palmstrm, C. M. Marcus, and F. Nichele. Proximity Effect Transfer from NbTi into a Semiconductor Heterostructure via Epitaxial Aluminum. *NanoLetters*, November 2016.

[42] E. V. Erofeev, S. V. Ishutkin, V. A. Kagadei, and K. S. Nosaeva. Multilayer low-resistance ge/au/ni/ti/au based ohmic contact to n-gaas. In *The 5th European Microwave Integrated Circuits Conference*, pages 290–293, 2010.

[43] Juewen Fan, Bingyan Jiang, Jiaji Zhao, Ran Bi, Jiadong Zhou, Zheng Liu, Guang Yang, Jie Shen, Fanming Qu, Li Lu, Ning Kang, and Xiaosong Wu. Asymmetric Fraunhofer pattern in Josephson junctions from heterodimensional superlattice V $_5$ S $_8$. *Chinese Physics B*, 31(5):057402, May 2022.

[44] S. M. Farzaneh, Mehdi Hatefipour, William F. Schiela, Neda Lotfizadeh, Peng Yu, Bassel Heiba Elfeky, William M. Strickland, Alex Matos-Abiague, and Javad Shabani. Observing magnetoanisotropic weak antilocalization in near-surface quantum wells. *Physical Review Research*, 6(1):013039, January 2024.

[45] Mark Fox and Radu Ispasoiu. Quantum Wells, Superlattices, and Band-Gap Engineering. In Safa Kasap and Peter Capper, editors, *Springer Handbook of Electronic and Photonic Materials*, pages 1021–1040. Springer US, Boston, MA, 2006.

[46] Secondo Franchi. Chapter 1 - Molecular beam epitaxy: fundamentals, historical background and future prospects. In Mohamed Henini, editor, *Molecular Beam Epitaxy*, pages 1–46. Elsevier, Oxford, 2013.

[47] Sergey Frolov. Quantum transport, lecture 10: Spin-orbit interaction. https://youtu.be/b8mW753flqI?si=KjQwkEJ_e4-4Mml5, Feb. 2013.

[48] Sergey Frolov. Majorana fireside chats: Vincent mourik and sergey frolov (april 2021). https://youtu.be/d1OLudwLfMk?si=1PeQJALo6JQxrdFn, April 2021.

[49] Sergey Frolov. Majorana fireside podcast, episode 1: The microsoft tgp paper live review. https://youtu.be/RnYghkDaHH0?si=OSjn632CJCVJGd16, July 2022.

[50] Sergey Frolov and Vincent Mourik. Data manipulation and omission in 'Quantized Majorana conductance', Zhang et al, Nature 2018. *Zenodo*, March 2021. Publisher: Zenodo.

[51] Liang Fu and C. L. Kane. Superconducting proximity effect and majorana fermions at the surface of a topological insulator. *Physical Review Letters*, 100(9), March 2008.

[52] Subhamoy Ghatak, Oliver Breunig, Fan Yang, Zhiwei Wang, Alexey A. Taskin, and Yoichi Ando. Anomalous Fraunhofer Patterns in Gated Josephson Junctions Based on the Bulk-Insulating Topological Insulator BiSbTeSe2. *Nano Letters*, 18(8):5124–5131, August 2018. Publisher: American Chemical Society.

[53] X.Y. Gong, T. Yamaguchi, H. Kan, T. Makino, K. Ohshimo, M. Aoyama, M. Kumagawa, N.L. Rowell, and R. Rinfret. Sulphur passivation of InAs(Sb). *Applied Surface Science*, 113-114:388–392, April 1997.

[54] R. Gross, A. Marx, F. Deppe, and K. Federov. Physics of josephson junctions: The zero voltage state.

[55] M. Grundmann. Quantum devices of reduced dimensionality. In F. Bassani, G. L. Liedl, and P. Wyder, editors, *Encyclopedia of Condensed Matter Physics*, pages 17–22. Academic Press, 2005.

[56] Jyongsil Gu, Wongoon Cha, Kenji Gamo, and Susumu Namba. Properties of niobium superconducting bridges prepared by electron-beam lithography and ion implantation. *Journal of Applied Physics*, 50(10):6437–6442, October 1979.

[57] W. Haberkorn, H. Knauer, and J. Richter. A theoretical study of the current-phase relation in Josephson contacts. *Physica Status Solidi (a)*, 47(2):K161–K164, June 1978.

[58] Y. Harada, S. Jensen, T. Akazaki, and H. Takayanagi. Anomalous magnetic flux periodicity of supercurrent in mesoscopic SNS Josephson junctions. *Physica C: Superconductivity*, 367(1-4):229–233, February 2002.

[59] Sean Hart, Hechen Ren, Timo Wagner, Philipp Leubner, Mathias Mhlbauer, Christoph Brne, Hartmut Buhmann, Laurens W. Molenkamp, and Amir Yacoby. Induced superconductivity in the quantum spin Hall edge. *Nature Physics*, 10(9):638–643, September 2014.

[60] M. Z. Hasan and C. L. Kane. *Colloquium* : Topological insulators. *Reviews of Modern Physics*, 82(4):3045–3067, November 2010.

[61] A. T. Hatke, T. Wang, C. Thomas, G. C. Gardner, and M. J. Manfra. Mobility in excess of 106 cm2/V s in InAs quantum wells grown on lattice mismatched InP substrates. *Applied Physics Letters*, 111(14):142106, October 2017.

[62] Dibyendu Hazra, Ltitia M. A. Pascal, Herv Courtois, and Anjan K. Gupta. Hysteresis in superconducting short weak links and μ-SQUIDs. *Physical Review B*, 82(18):184530, November 2010.

[63] J. P. Heida, B. J. Van Wees, T. M. Klapwijk, and G. Borghs. Nonlocal supercurrent in mesoscopic Josephson junctions. *Physical Review B*, 57(10):R5618–R5621, March 1998.

[64] Werner Heisenberg. Interview of Werner Heisenberg by Thomas S. Kuhn and John L. Heilbron. Niels Bohr Library & Archives, American Institute of Physics, College Park, MD USA, 1963. www.aip.org/history-programs/niels-bohr-library/oral-histories/4661-12.

[65] Michael Hell, Martin Leijnse, and Karsten Flensberg. Two-Dimensional Platform for Networks of Majorana Bound States. *Physical Review Letters*, 118(10):107701, March 2017.

[66] A. Hertel, L.O. Andersen, D.M.T. van Zanten, M. Eichinger, P. Scarlino, S. Yadav, J. Karthik, S. Gronin, G.C. Gardner, M.J. Manfra, C.M. Marcus, and K.D. Petersson. Electrical properties of selective-area-grown superconductor-semiconductor hybrid structures on silicon. *Phys. Rev. Appl.*, 16:044015, Oct 2021.

[67] Richard Hess, Henry F. Legg, Daniel Loss, and Jelena Klinovaja. Trivial Andreev Band Mimicking Topological Bulk Gap Reopening in the Nonlocal Conductance of Long Rashba Nanowires. *Physical Review Letters*, 130(20):207001, May 2023.

[68] S. Hikami, A. I. Larkin, and Y. Nagaoka. Spin-Orbit Interaction and Magnetoresistance in the Two Dimensional Random System. *Progress of Theoretical Physics*, 63(2):707–710, February 1980.

[69] R. Holm and W. Meissner. Messungen mit Hilfe von flssigem Helium. XIII. *Zeitschrift fr Physik*, 74(11):715–735, November 1932.

[70] T. Hyart, B. van Heck, I. C. Fulga, M. Burrello, A. R. Akhmerov, and C. W. J. Beenakker. Flux-controlled quantum computation with Majorana fermions. *Physical Review B*, 88(3):035121, July 2013.

[71] Jun-ichiro Inoue. GMR, TMR and BMR. In *Nanomagnetism and Spintronics*, pages 15–92. Elsevier, 2009.

[72] Ioffe Institute. Insb - indium antimonide. https://www.ioffe.ru/SVA/NSM/Semicond/InSb/bandstr.html, 2001.

[73] S. V. Iordanskii, Yu. B. Lyanda-Geller, and G. E. Pikus. Weak localization in quantum wells with spin-orbit interaction. *ZhETF Pisma Redaktsiiu*, 60:199, August 1994. ADS Bibcode: 1994ZhPmR..60..199I.

[74] M. J. Iqbal, J. P. De. Jong, D. Reuter, A. D. Wieck, and C. H. Van Der Wal. Split-gate quantum point contacts with tunable channel length. *Journal of Applied Physics*, 113(2):024507, January 2013.

[75] Mohsin Iqbal, Nathanan Tantivasadakarn, Ruben Verresen, Sara L. Campbell, Joan M. Dreiling, Caroline Figgatt, John P. Gaebler, Jacob Johansen, Michael Mills, Steven A. Moses, Juan M. Pino, Anthony Ransford, Mary Rowe, Peter Siegfried, Russell P. Stutz, Michael Foss-Feig, Ashvin Vishwanath, and Henrik Dreyer. Non-Abelian topological order and anyons on a trapped-ion processor. *Nature*, 626(7999):505–511, February 2024.

[76] Ryosuke Ishiguro and Sbastien Balibar. New Measurements of Wetting by Helium Mixtures. *Journal of Low Temperature Physics*, 140(1):29–49, July 2005.

[77] S. C. Jain and M. Willander. Chapter 3 - Mechanism of Strain Relaxation. In *Silicon-Germanium Strained Layers and Heterostructures*, volume 74 of *Semiconductors and Semimetals*, pages 41–60. Elsevier, 2003. ISSN: 0080-8784.

[78] Akira Kakuta, Yuji Furukawa, and Nobuyuki Moronuki. The Effect of Substrate Crystal Orientations on Surface Properties of SiC Thin Layer Grown by MBE. *Journal of Advanced Mechanical Design, Systems, and Manufacturing*, 2(4):824–832, 2008.

[79] Anand Kamlapure, Tanmay Das, Somesh Chandra Ganguli, Jayesh B. Parmar, Somnath Bhattacharyya, and Pratap Raychaudhuri. Emergence of nanoscale inhomogeneity in the superconducting state of a homogeneously disordered conventional superconductor. *Scientific Reports*, 3(1):2979, October 2013.

[80] Min-Gu Kang and Hyung-Ho Park. Effect of prepared GaAs surface on the sulfidation with (NH4)2Sx solution. *Journal of Vacuum Science & Technology A: Vacuum, Surfaces, and Films*, 17(1):88–92, January 1999.

[81] Torsten Karzig, William S. Cole, and Dmitry I. Pikulin. Quasiparticle Poisoning of Majorana Qubits. *Physical Review Letters*, 126(5):057702, February 2021.

[82] Y. Kasahara, T. Ohnishi, Y. Mizukami, O. Tanaka, Sixiao Ma, K. Sugii, N. Kurita, H. Tanaka, J. Nasu, Y. Motome, T. Shibauchi, and Y. Matsuda. Majorana quantization and half-integer thermal quantum Hall effect in a Kitaev spin liquid. *Nature*, 559(7713):227–231, July 2018.

[83] G. Kells, D. Meidan, and P. W. Brouwer. Near-zero-energy end states in topologically trivial spin-orbit coupled superconducting nanowires with a smooth confinement. *Physical Review B*, 86(10):100503, September 2012.

[84] Nico Kirchner, Darragh Millar, Babatunde M. Ayeni, Adam Smith, Joost K. Slingerland, and Frank Pollmann. Numerical simulation of non-abelian anyons. *Phys. Rev. B*, 107:195129, May 2023.

[85] Alexei Kitaev. Quantum computations: algorithms and error correction. *Russian Mathematical Surveys*, 52(6):1191–1249, December 1997.

[86] Alexei Kitaev. Unpaired Majorana fermions in quantum wires. *Physics-Uspekhi*, 44(10S):131–136, October 2001. arXiv:cond-mat/0010440.

[87] J.A. Kittl, K. Opsomer, M. Popovici, N. Menou, B. Kaczer, X.P. Wang, C. Adelmann, M.A. Pawlak, K. Tomida, A. Rothschild, B. Govoreanu, R. Degraeve, M. Schaekers, M. Zahid, A. Delabie, J. Meersschaut, W. Polspoel, S. Clima, G. Pourtois, W. Knaepen, C. Detavernier, V.V. Afanasev, T. Blomberg, D. Pierreux, J. Swerts, P. Fischer, J.W. Maes, D. Manger, W. Vandervorst, T. Conard, A. Franquet, P. Favia, H. Bender, B. Brijs, S. Van Elshocht, M. Jurczak, J. Van Houdt, and D.J. Wouters. High-k dielectrics for future generation memory devices (Invited Paper). *Microelectronic Engineering*, 86(7-9):1789–1795, July 2009.

[88] M. Kjaergaard, H. J. Suominen, M. P. Nowak, A. R. Akhmerov, J. Shabani, C. J. Palmstrøm, F. Nichele, and C. M. Marcus. Transparent semiconductor-superconductor interface and induced gap in an epitaxial heterostructure josephson junction. *Phys. Rev. Appl.*, 7:034029, Mar 2017.

[89] A. W. Kleinsasser and T. N. Jackson. Superconductivity and Field Effect Transistors. *Japanese Journal of Applied Physics*, 26(S3-2):1545, January 1987.

[90] K. W. Kolanski. Thermodynamics and Kinetics of Adsorption and Desorption. In *Surface Science*, pages 185–228. Wiley, April 2012.

[91] J. Konopka. Conduction electron spin resonance in InAs. *Physics Letters A*, 26(1):29–31, December 1967.

[92] Christina V. Kraus, P. Zoller, and Mikhail A. Baranov. Braiding of Atomic Majorana Fermions in Wire Networks and Implementation of the Deutsch-Jozsa Algorithm. *Physical Review Letters*, 111(20):203001, November 2013.

[93] Yi-Hua Lai, Sankar Das Sarma, and Jay D. Sau. Quality factor for zero-bias conductance peaks in Majorana nanowire. *Physical Review B*, 106(9):094504, September 2022. arXiv:2111.01178 [cond-mat].

[94] Eduardo J. H. Lee, Xiaocheng Jiang, Manuel Houzet, Ramn Aguado, Charles M. Lieber, and Silvano De Franceschi. Spin-resolved Andreev levels and parity crossings in hybrid superconductorsemiconductor nanostructures. *Nature Nanotechnology*, 9(1):79–84, January 2014.

[95] Joon Sue Lee, Borzoyeh Shojaei, Mihir Pendharkar, Mayer Feldman, Kunal Mukherjee, and Chris J. Palmstrm. Contribution of top barrier materials to high mobility in

near-surface InAs quantum wells grown on GaSb(001). *Physical Review Materials*, 3(1):014603, January 2019.

[96] Stephen R. Lee, Peter A. Sharma, Ana L. Lima-Sharma, Wei Pan, and Tina M. Nenoff. Topological Quantum Materials for Realizing Majorana Quasiparticles. *Chemistry of Materials*, 31(1):26–51, January 2019.

[97] Yuri D. Lensky, Kostyantyn Kechedzhi, Igor Aleiner, and Eun-Ah Kim. Graph gauge theory of mobile non-Abelian anyons in a qubit stabilizer code. *Annals of Physics*, 452:169286, 2023.

[98] Roman M. Lutchyn, Jay D. Sau, and Sankar Das Sarma. Majorana fermions and a topological phase transition in semiconductor-superconductor heterostructures. *Physical Review Letters*, 105(7), August 2010.

[99] Ettore Majorana. Teoria simmetrica dellelettrone e del positrone. *Il Nuovo Cimento*, 14:171–183, 1937.

[100] S. Majumdar, H.S. Majumdar, R. sterbacka, and E. McCarthy. Organic spintronics. In *Reference Module in Materials Science and Materials Engineering*. Elsevier, 2016.

[101] William Mayer, William F. Schiela, Joseph Yuan, Mehdi Hatefipour, Wendy L. Sarney, Stefan P. Svensson, Asher C. Leff, Tiago Campos, Kaushini S. Wickramasinghe, Matthieu C. Dartiailh, Igor uti, and Javad Shabani. Superconducting Proximity Effect in InAsSb Surface Quantum Wells with In Situ Al Contacts. *ACS Applied Electronic Materials*, 2(8):2351–2356, 2020. _eprint: https://doi.org/10.1021/acsaelm.0c00269.

[102] N. Miura. Magneto-Spectroscopy of Semiconductors. In *Comprehensive Semiconductor Science and Technology*, pages 256–342. Elsevier, 2011.

[103] V. Mourik, K. Zuo, S. M. Frolov, S. R. Plissard, E. P. A. M. Bakkers, and L. P. Kouwenhoven. Signatures of majorana fermions in hybrid superconductor-semiconductor nanowire devices. *Science*, 336(6084):1003–1007, May 2012. Publisher: American Association for the Advancement of Science.

[104] Sebastian Nagies, Botao Wang, Adam C. Knapp, Andr Eckardt, and Nathan L. Harshman. Beyond braid statistics: Constructing a lattice model for anyons with exchange statistics intrinsic to one dimension. *SciPost Phys.*, 16:086, 2024.

[105] J. Nakamura, S. Liang, G. C. Gardner, and M. J. Manfra. Direct observation of anyonic braiding statistics. *Nature Physics*, 16(9):931–936, September 2020.

[106] Wodzimierz Nakwaski. Effective masses of electrons and heavy holes in GaAs, InAs, A1As and their ternary compounds. *Physica B: Condensed Matter*, 210(1):1–25, April 1995.

[107] Marek Naroniak, Matthieu C. Dartiailh, Jonathan P. Dowling, Javad Shabani, and Tim Byrnes. Quantum gates for Majoranas zero modes in topological superconductors in one-dimensional geometry. *Physical Review B*, 103(20):205429, May 2021.

[108] K. Neurohr, Th. Schpers, J. Malindretos, S. Lachenmann, A. I. Braginski, H. Lth, M. Behet, G. Borghs, and A. A. Golubov. Local suppression of Josephson currents in niobium/two-dimensional electron gas/niobium structures by an injection current. *Physical Review B*, 59(17):11197–11200, May 1999.

[109] Gabriel Niebler, Gianaurelio Cuniberti, and Tomas Novotny. Analytical calculation of the excess current in the OTBK theory. *Superconductor Science and Technology*, 22(8):085016, August 2009. arXiv:0905.4852 [cond-mat].

[110] Cun-Zheng Ning, Letian Dou, and Peidong Yang. Bandgap engineering in semiconductor alloy nanomaterials with widely tunable compositions. *Nature Reviews Materials*, 2(12):17070, December 2017.

[111] Junsaku Nitta, Tatsushi Akazaki, Hideaki Takayanagi, and Kunihiro Arai. Transport properties in an InAs-inserted-channel In 0.52 Al 0.48 As/ In 0.53 Ga 0.47 As heterostructure coupled superconducting junction. *Physical Review B*, 46(21):14286–14289, December 1992.

[112] Junsaku Nitta, Tatsushi Akazaki, Hideaki Takayanagi, and Takatomo Enoki. Gate control of spinorbit interaction in an InAs-inserted In0.53Ga0.47As/In0.52Al0.48As heterostructure. *Physica E: Low-dimensional Systems and Nanostructures*, 2(1-4):527–531, July 1998.

[113] Jiho Noh, Thomas Schuster, Thomas Iadecola, Sheng Huang, Mohan Wang, Kevin P. Chen, Claudio Chamon, and Mikael C. Rechtsman. Braiding photonic topological zero modes. *Nature Physics*, 16(9):989–993, September 2020.

[114] E. C. T. O'Farrell, A. C. C. Drachmann, M. Hell, A. Fornieri, A. M. Whiticar, E. B. Hansen, S. Gronin, G. C. Gardener, C. Thomas, M. J. Manfra, K. Flensberg,

C. M. Marcus, and F. Nichele. Hybridization of sub-gap states in one-dimensional superconductor/semiconductor Coulomb islands. *Physics Review Letters*, April 2018.

[115] Linde A. B. Olde Olthof, Stijn R. De Wit, Shu-Ichiro Suzuki, Inanc Adagideli, Jason W. A. Robinson, and Alexander Brinkman. Multiple Andreev reflections in topological Josephson junctions with chiral Majorana modes. *Physical Review B*, 107(18):184510, May 2023.

[116] Yuval Oreg, Gil Refael, and Felix Von Oppen. Helical liquids and Majorana bound states in quantum wires. *Physical Review Letters*, 105(17), October 2010.

[117] Joseph OConnell Yuan, Kaushini S. Wickramasinghe, William M. Strickland, Matthieu C. Dartiailh, Kasra Sardashti, Mehdi Hatefipour, and Javad Shabani. Epitaxial superconductor-semiconductor two-dimensional systems for superconducting quantum circuits. *Journal of Vacuum Science & Technology A: Vacuum, Surfaces, and Films*, 39(3):033407, May 2021.

[118] P Marra, D Inotani, and M Nitta. Braiding with Majorana lattices: Groundstate degeneracy and supersymmetry.

[119] Haining Pan and Sankar Das Sarma. Physical mechanisms for zero-bias conductance peaks in Majorana nanowires. *Physical Review Research*, 2(1):013377, March 2020.

[120] Federico Paolucci, Giorgio De Simoni, Elia Strambini, Paolo Solinas, and Francesco Giazotto. Ultra-Efficient Superconducting Dayem Bridge Field-Effect Transistor. *Nano Letters*, 18(7):4195–4199, July 2018.

[121] Douglas J. Paul. Misfit dislocations. https://userweb.eng.gla.ac.uk/douglas.paul/SiGe/misfit.html, 2022.

[122] Falko Pientka, Anna Keselman, Erez Berg, Amir Yacoby, Ady Stern, and Bertrand I. Halperin. Topological Superconductivity in a Planar Josephson Junction. *Physical Review X*, 7(2):021032, May 2017.

[123] Dmitry I. Pikulin, Bernard van Heck, Torsten Karzig, Esteban A. Martinez, Bas Nijholt, Tom Laeven, Georg W. Winkler, John D. Watson, Sebastian Heedt, Mine Temurhan, Vicky Svidenko, Roman M. Lutchyn, Mason Thomas, Gijs de Lange, Lucas Casparis, and Chetan Nayak. Protocol to identify a topological superconducting phase in a three-terminal device. *arXiv*, 2021. Publisher: arXiv Version Number: 1.

[124] Nicola Pinto, S. Javad Rezvani, Andrea Perali, Luca Flammia, Milorad V. Milosevi, Matteo Fretto, Cristina Cassiago, and Natascia De Leo. Dimensional crossover and incipient quantum size effects in superconducting niobium nanofilms. *Scientific Reports*, 8(1):4710, March 2018.

[125] Dmitri Pogosyan. Lecture 35: Diffraction: Single slit. https://sites.ualberta.ca/~pogosyan/teaching/PHYS_130/FALL_2010/lectures/lect35/lecture35.html, 2010.

[126] Vlad S. Pribiag, Arjan J. A. Beukman, Fanming Qu, Maja C. Cassidy, Christophe Charpentier, Werner Wegscheider, and Leo P. Kouwenhoven. Edge-mode superconductivity in a two-dimensional topological insulator. *Nature Nanotechnology*, 10(7):593–597, July 2015.

[127] Fanming Qu, Jasper Van Veen, Folkert K. De Vries, Arjan J. A. Beukman, Michael Wimmer, Wei Yi, Andrey A. Kiselev, Binh-Minh Nguyen, Marko Sokolich, Michael J. Manfra, Fabrizio Nichele, Charles M. Marcus, and Leo P. Kouwenhoven. Quantized Conductance and Large g -Factor Anisotropy in InSb Quantum Point Contacts. *Nano Letters*, 16(12):7509–7513, December 2016.

[128] C. H. L. Quay, T. L. Hughes, J. A. Sulpizio, L. N. Pfeiffer, K. W. Baldwin, K. W. West, D. Goldhaber-Gordon, and R. de Picciotto. Observation of a one-dimensional spinorbit gap in a quantum wire. *Nature Physics*, 6(5):336–339, May 2010.

[129] Asbjrn Rasmussen, Jeroen Danon, Henri Suominen, Fabrizio Nichele, Morten Kjaergaard, and Karsten Flensberg. Effects of spin-orbit coupling and spatial symmetries on the Josephson current in SNS junctions. *Phys. Rev. B*, 93(15):155406, April 2016. Publisher: American Physical Society.

[130] G. Ribes, J. Mitard, M. Denais, S. Bruyere, F. Monsieur, C. Parthasarathy, E. Vincent, and G. Ghibaudo. Review on high-k dielectrics reliability issues. *IEEE Transactions on Device and Materials Reliability*, 5(1):5–19, March 2005.

[131] Joost Ridderbos, Matthias Brauns, Folkert K. de Vries, Jie Shen, Ang Li, Sebastian Klling, Marcel A. Verheijen, Alexander Brinkman, Wilfred G. van der Wiel, Erik P. A. M. Bakkers, and Floris A. Zwanenburg. Hard Superconducting Gap and Diffusion-Induced Superconductors in GeSi Nanowires. *Nano Letters*, 20(1):122–130, January 2020. Publisher: American Chemical Society.

[132] Joschka Roffe. Quantum error correction: an introductory guide. *Contemporary Physics*, 60(3):226–245, July 2019.

[133] Yusuff Adeyemi Salawu, Jae Hyun Yun, Jong-Soo Rhyee, Minoru Sasaki, and Heon-Jung Kim. Weak antilocalization, spinorbit interaction, and phase coherence length of a Dirac semimetal Bi0.97Sb0.03. *Scientific Reports*, 12(1):2845, February 2022.

[134] Jay D. Sau, Roman M. Lutchyn, Sumanta Tewari, and Sankar Das Sarma. Generic new platform for topological quantum computation using semiconductor heterostructures. *Physical Review Letters*, 104(4), January 2010.

[135] I. Sadi, S. Ben Radhia, and K. Boujdaria. Band parameters of gaas, inas, inp, and insb in the 40-band k·p model. *Journal of Applied Physics*, 107(4):043701, February 2010. _eprint: https://pubs.aip.org/aip/jap/article-pdf/doi/10.1063/1.3295900/13298149/043701_1_online.pdf.

[136] Tobias W Schmitt, Benedikt Frohn, Wilhelm Wittl, Abdur R Jalil, Michael Schleenvoigt, Erik Zimmermann, Anne Schmidt, Thomas Schpers, Juan Carlos Cuevas, Alexander Brinkman, Detlev Grtzmacher, and Peter Schffelgen. Anomalous temperature dependence of multiple Andreev reflections in a topological insulator Josephson junction. *Superconductor Science and Technology*, 36(2):024002, February 2023.

[137] T. Senthil and Matthew P. A. Fisher. Quasiparticle localization in superconductors with spin-orbit scattering. *Physical Review B*, 61(14):9690–9698, April 2000.

[138] J. Shabani, M. Kjaergaard, H. J. Suominen, Younghyun Kim, F. Nichele, K. Pakrouski, T. Stankevic, R. M. Lutchyn, P. Krogstrup, R. Feidenhans'l, S. Kraemer, C. Nayak, M. Troyer, C. M. Marcus, and C. J. Palmstrøm. Two-dimensional epitaxial superconductor-semiconductor heterostructures: A platform for topological superconducting networks. *Phys. Rev. B*, 93:155402, Apr 2016.

[139] Nathan Shettell, William J Munro, Damian Markham, and Kae Nemoto. Practical limits of error correction for quantum metrology. *New Journal of Physics*, 23(4):043038, April 2021.

[140] A. Shetty, F. Sfigakis, W. Y. Mak, K. Das Gupta, B. Buonacorsi, M. C. Tam, H. S. Kim, I. Farrer, A. F. Croxall, H. E. Beere, A. R. Hamilton, M. Pepper, D. G. Austing, S. A. Studenikin, A. Sachrajda, M. E. Reimer, Z. R. Wasilewski, D. A. Ritchie, and J. Baugh. Effects of biased and unbiased illuminations on dopant-free gaas/algaas 2degs, 2021.

[141] Y. Shi, D. Gosselink, K. Gharavi, J. Baugh, and Z.R. Wasilewski. Optimization of metamorphic buffers for MBE growth of high quality AlInSb/InSb quantum struc-

tures: Suppression of hillock formation. *Journal of Crystal Growth*, 477:7–11, November 2017.

[142] Yinqiu (Peyton) Shi. *Molecular beam epitaxial growth of InSb quantum well heterostructures for applications in topological quantum computing*. PhD thesis, University of Waterloo, 2021.

[143] B. Shojaei, P. J. J. O'Malley, J. Shabani, P. Roushan, B. D. Schultz, R. M. Lutchyn, C. Nayak, J. M. Martinis, and C. J. Palmstrm. Demonstration of gate control of spin splitting in a high-mobility InAs/AlSb two-dimensional electron gas. *Physical Review B*, 93(7):075302, February 2016.

[144] Peter W. Shor. Scheme for reducing decoherence in quantum computer memory. *Physical Review A*, 52(4):R2493–R2496, October 1995.

[145] Tudor D. Stanescu, Roman M. Lutchyn, and S. Das Sarma. Majorana fermions in semiconductor nanowires. *Physical Review B*, 84(14):144522, October 2011.

[146] William M. Strickland, Lukas J. Baker, Jaewoo Lee, Krishna Dindial, Bassel Heiba Elfeky, Patrick J. Strohbeen, Mehdi Hatefipour, Peng Yu, Ido Levy, Jacob Issokson, Vladimir E. Manucharyan, and Javad Shabani. Characterizing losses in InAs two-dimensional electron gas-based gatemon qubits. *Physical Review Research*, 6(2):023094, April 2024.

[147] H. J. Suominen, J. Danon, M. Kjaergaard, K. Flensberg, J. Shabani, C. J. Palmstrm, F. Nichele, and C. M. Marcus. Anomalous Fraunhofer interference in epitaxial superconductor-semiconductor Josephson junctions. *Physical Review B*, 95(3):035307, January 2017.

[148] D B Suyatin, C Thelander, M T Bjrk, I Maximov, and L Samuelson. Sulfur passivation for ohmic contact formation to InAs nanowires. *Nanotechnology*, 18(10):105307, March 2007.

[149] Hideaki Takayanagi and Tatsushi Akazaki. Temperature dependence of the critical current in a clean-limit superconductor-2DEG-superconductor junction. *Solid State Communications*, 96(11):815–819, December 1995.

[150] Hideaki Takayanagi and Tsuyoshi Kawakami. Superconducting Proximity Effect in the Native Inversion Layer on InAs. *Physical Review Letters*, 54(22):2449–2452, June 1985.

[151] So Takei, Benjamin M. Fregoso, Hoi-Yin Hui, Alejandro M. Lobos, and S. Das Sarma. Soft Superconducting Gap in Semiconductor Majorana Nanowires. *Physical Review Letters*, 110(18):186803, April 2013.

[152] E. F. Talantsev, K. Iida, T. Ohmura, T. Matsumoto, W. P. Crump, N. M. Strickland, S. C. Wimbush, and H. Ikuta. p-wave superconductivity in iron-based superconductors. *Scientific Reports*, 9(1):14245, December 2019.

[153] Jeffrey C. Y. Teo and C. L. Kane. Majorana Fermions and Non-Abelian Statistics in Three Dimensions. *Physical Review Letters*, 104(4):046401, January 2010. arXiv:0909.4741 [cond-mat].

[154] Sumanta Tewari, Sankar Das Sarma, Chetan Nayak, Chuanwei Zhang, and P. Zoller. Quantum Computation using Vortices and Majorana Zero Modes of a p x + i p y Superfluid of Fermionic Cold Atoms. *Physical Review Letters*, 98(1):010506, January 2007.

[155] C. Thomas, A. T. Hatke, A. Tuaz, R. Kallaher, T. Wu, T. Wang, R. E. Diaz, G. C. Gardner, M. A. Capano, and M. J. Manfra. High-mobility InAs 2DEGs on GaSb substrates: A platform for mesoscopic quantum transport. *Physical Review Materials*, 2(10):104602, October 2018.

[156] T. Tschirky, S. Mueller, Ch. A. Lehner, S. Flt, T. Ihn, K. Ensslin, and W. Wegscheider. Scattering mechanisms of highest-mobility InAs / AlxGa1-xSb quantum wells. *Physical Review B*, 95(11):115304, March 2017.

[157] Gary Tuttle, Herbert Kroemer, and John H. English. Effects of interface layer sequencing on the transport properties of InAs/AlSb quantum wells: Evidence for antisite donors at the InAs/AlSb interface. *Journal of Applied Physics*, 67(6):3032–3037, March 1990.

[158] Pawan Tyagi. New value of old knowledge: sulphur-based GaAs surface passivation and potential GaAs application in molecular electronics and spintronics. *Materials Research Express*, 10(4):042003, April 2023.

[159] Dirk van Delft and Peter Kes. The discovery of superconductivity. *Europhysics News*, 42(1):21–25, 2011.

[160] Nick Van Loo, Grzegorz P. Mazur, Tom Dvir, Guanzhong Wang, Robin C. Dekker, Ji-Yin Wang, Mathilde Lemang, Cristina Sfiligoj, Alberto Bordin, David Van Driel,

Ghada Badawy, Sasa Gazibegovic, Erik P. A. M. Bakkers, and Leo P. Kouwenhoven. Electrostatic control of the proximity effect in the bulk of semiconductor-superconductor hybrids. *Nature Communications*, 14(1):3325, June 2023.

[161] V.V. Vershinin. Braids, their Properties and Generalizations. In *Handbook of Algebra*, volume 4, pages 427–465. Elsevier, 2006.

[162] Kristijonas Vizbaras, Alexander Bachmann, Shamsul Arafin, Kai Saller, Stefan Sprengel, Gerhard Boehm, Ralf Meyer, and Markus-Christian Amann. Mbe growth of low threshold gasb-based lasers with emission wavelengths in the range of 2.52.7um. *Journal of Crystal Growth*, 323:446–449, 2011.

[163] D. Yu. Vodolazov and F. M. Peeters. Origin of the hysteresis of the current voltage characteristics of superconducting microbridges near the critical temperature. *Physical Review B*, 84(9):094511, September 2011.

[164] Roger E. Welser, Stephen J. Polly, Mitsul Kacharia, Anastasiia Fedorenko, Ashok K. Sood, and Seth M. Hubbard. Design and Demonstration of High-Efficiency Quantum Well Solar Cells Employing Thin Strained Superlattices. *Scientific Reports*, 9(1):13955, September 2019.

[165] Kaushini S. Wickramasinghe, William Mayer, Joseph Yuan, Tri Nguyen, Lucy Jiao, Vladimir Manucharyan, and Javad Shabani. Transport properties of near surface InAs two-dimensional heterostructures. *Applied Physics Letters*, 113(26):262104, December 2018.

[166] Frank Wilczek. Majorana returns. *Nature Physics*, 5(9):614–618, 2009. Publisher: Nature Publishing Group.

[167] G. D. Wilk, R. M. Wallace, and J. M. Anthony. High-k gate dielectrics: Current status and materials properties considerations. *Journal of Applied Physics*, 89(10):5243–5275, May 2001.

[168] J. R. Williams, A. J. Bestwick, P. Gallagher, Seung Sae Hong, Y. Cui, Andrew S. Bleich, J. G. Analytis, I. R. Fisher, and D. Goldhaber-Gordon. Unconventional Josephson Effect in Hybrid Superconductor-Topological Insulator Devices. *Phys. Rev. Lett.*, 109(5):056803, July 2012. Publisher: American Physical Society.

[169] Roland Winkler. 6.3 SIA Spin Splitting. In *SpinOrbit Coupling Effects in Two-Dimensional Electron and Hole Systems*. Springer, 2003.

[170] J. D. S. Witt, S. J. Pauka, G. C. Gardner, S. Gronin, T. Wang, C. Thomas, M. J. Manfra, D. J. Reilly, and M. C. Cassidy. Spin-relaxation mechanisms in InAs quantum well heterostructures. *Applied Physics Letters*, 122(8):083101, February 2023.

[171] Hei Wong, Jieqiong Zhang, and Jun Liu. Contacts at the Nanoscale and for Nanomaterials. *Nanomaterials*, 14(4):386, February 2024.

[172] Yijia Wu, Jie Liu, and XinCheng Xie. Recent progress on non-Abelian anyons: from Majorana zero modes to topological Dirac fermionic modes. *Science China Physics, Mechanics & Astronomy*, 66(6):267004, April 2023.

[173] Zheng-Yuan Xue. Measurement based controlled not gate for topological qubits in a Majorana fermion and quantum-dot hybrid system. *The European Physical Journal D*, 67(4):89, April 2013.

[174] Chuan-Zhe Yao and Wei-Min Zhang. The differential conductance tunnel spectroscopy in an analytical solvable two-terminal Majorana device. *New Journal of Physics*, 24(7):073015, July 2022.

[175] Tomohiro Yokoyama, Mikio Eto, and Yuli V. Nazarov. Anomalous Josephson effect induced by spin-orbit interaction and Zeeman effect in semiconductor nanowires. *Physical Review B*, 89(19):195407, May 2014.

[176] Ye-Min Zhan, Yu-Ge Chen, Bin Chen, Ziqiang Wang, Yue Yu, and Xi Luo. Universal topological quantum computation with strongly correlated Majorana edge modes. *New Journal of Physics*, 24(4):043009, April 2022.

[177] Teng Zhang, Tyler Lindemann, Geoffrey C. Gardner, Sergei Gronin, Tailung Wu, and Michael J. Manfra. Mobility exceeding 100 000 cm^2/V s in modulation-doped shallow inas quantum wells coupled to epitaxial aluminum. *Phys. Rev. Mater.*, 7:056201, May 2023.

[178] Zhi-Feng Zhang, Qing-Rui Wang, and Peng Ye. Non-abelian fusion, shrinking, and quantum dimensions of abelian gauge fluxes. *Phys. Rev. B*, 107:165117, Apr 2023.

APPENDICES

Appendix A

Code

A.1 Weak anti-localization fits

A.1.1 HLN model

```
from itertools import repeat
import math
import numpy as np
import matplotlib.pyplot as plt
from scipy.optimize import curve_fit
from scipy.special import psi
from matplotlib import rcParams

# Mathematical constants and terms
e = 1.60217663 * 10**-19
pi = math.pi
hbar = 1.054571817 * 10**-34
h = 1.054571817 * 10**-34 * 2 * pi

# HLN function
def hln(x, A, C):
    return (2 * pi * h / e**2) * (e**2 / (2 * pi**2 * hbar)) * (psi(1/2 +
                                    A/x + C/x) + 1/2 * psi(1/2 + A/
                                   x + 2 * C/x) - 1/2 * psi(1/2 + A
                                   /x) - np.log(A/x + C/x) - 1/2 *
                                   np.log((A + 2 * C) / x) + 1/2 *
                                   np.log(A/x))
```

```
# To plot for both - and + B
def mirrored(x, A, C):
    if x == 0:
        return 0
    if x < 0:
        return hln(-x, A, C)
    else:
        return hln(x, A, C)

# Load data from a file (assuming two columns: x and y)
def load_data(file_name):
    data = np.loadtxt(file_name)
    x = data[:, 0]
    y = data[:, 1]
    return data, x, y

# Fit the data to the linear function
def fit_data_to_linear(x, y):
    popt, pcov = curve_fit(hln, x, y, p0 = [10**-10, 10**-5], maxfev =
                                        5000)
    return popt

# For mT
def scale(x):
    return x*1000

# Formatting stuff
SMALL_SIZE = 8
MEDIUM_SIZE = 10
BIGGER_SIZE = 20
rcParams['font.weight'] = 'bold'

# Plot the original data and the fitted line
def plot_data_and_fit(x, y, A, C):
    plt.scatter(list (map (scale, x)), y, color='orange', linewidth = 5)
    plt.plot(list (map (scale, x)), list (map (mirrored, x, repeat(A),
                                        repeat(C))), color='black',
                                        linewidth = 5)
    plt.xlabel('B (mT)', size = BIGGER_SIZE)
    plt.ylabel(u'Delta*sigma*(e^2/2*pi*h)', size = BIGGER_SIZE)
    plt.locator_params(axis = 'y', nbins = 3)
    plt.locator_params(axis = 'x', nbins = 3)
    plt.tick_params(axis = 'both', which = 'major', labelsize = 20)
    plt.show()
```

```
# Main function
def main():
    file_name = input("Enter the name of the file containing the data: ")
    pairs, x, y = load_data(file_name)
    pos = pairs[pairs[:, 0] > 0]
    A, C = fit_data_to_linear(pos[:, 0], pos[:, 1])
    print("Fitted parameters:", A, C)
    plot_data_and_fit(x, y, A, C)

if __name__ == "__main__":
    main()
```

A.1.2 ILP model

```
    from itertools import repeat
import math
import numpy as np
import matplotlib.pyplot as plt
from scipy.optimize import curve_fit
from scipy.special import psi
from matplotlib import rcParams

# Mathematical constants and terms
e = 1.60217663 * 10**-19
pi = math.pi
hbar = 1.054571817 * 10**-34
h = hbar * 2 * pi
coeff = (e**2 / (2 * pi**2 * hbar))
C = np.euler_gamma

# ILP function
def ilp(x, A, D):
    def a(n):
        return n + 1/2 + A/x + D/x

    def S(b):
        return ((8) / (np.sqrt(7 + 16 * b)) * (np.arctan((np.sqrt(7 + 16
                                                * b)) / (1 - 2 * b)) - pi *
                                                np.heaviside(1 - 2 * b, 0.5)
                                                ))

    def sum(x, n_max):
        result = 0
```

```
        for n in range(1, n_max + 1):
            result += 3 / n - ((3 * a(n) ** 2 + 2 * a(n) * (D / x) - 1 -
                                2 * (2 * n + 1) * (D / x
                                )) / ((a(n) + (D / x)) *
                                 a(n - 1) * a(n + 1) - 2
                                 * (D / x) * ((2 * n + 1
                                ) * a(n) - 1)))
        return result

    return ((2 * pi * h / e**2) * coeff / 2 * (sum(x, 10000) - 1 / a(0) -
                                 (2 * a(0) + 1 + (D/x)) / (a(1)
                                * (a(0) + (D/x)) - 2 * (D/x)) -
                                2 * np.log(A/x + D/x) - np.log(A
                                /x + 2 * D/x) - 3 * C - S(A/D) -
                                 (psi(1/2 + A/x) - np.log(A/x)))
                                )

# To plot for both - and + B
def mirrored(x, A, C):
    if x == 0:
        return 0
    if x < 0:
        return ilp(-x, A, C)
    else:
        return ilp(x, A, C)

# Load data from a file (assuming two columns: x and y)
def load_data(file_name):
    data = np.loadtxt(file_name)
    x = data[:, 0]
    y = data[:, 1]
    return data, x, y

# Fit the data to the linear function
def fit_data_to_linear(x, y):
    popt, pcov = curve_fit(ilp, x, y, p0 = [0.0001, 0.001], maxfev = 5000
                                )
    return popt

# For mT
def scale(x):
    return x * 1000

# Formatting stuff
SMALL_SIZE = 8
```

```
MEDIUM_SIZE = 10
BIGGER_SIZE = 20
rcParams['font.weight'] = 'bold'

# Plot the original data and the fitted line
def plot_data_and_fit(x, y, A, C):
    plt.scatter(list(map(scale, x)), y, color='darkorange', linewidth = 5
                                        )
    plt.plot(list(map(scale, x)), list(map(mirrored, x, repeat(A), repeat
                                        (C))), color='black', linewidth
                                        = 5)
    plt.xlabel('B (mT)', size = BIGGER_SIZE)
    plt.ylabel(u'Delta*sigma(e^2/2*pi*h)', size = BIGGER_SIZE)
    plt.locator_params(axis = 'y', nbins = 3)
    plt.locator_params(axis = 'x', nbins = 3)
    plt.tick_params(axis = 'both', which = 'major', labelsize = 20)
    plt.show()

# Main function
def main():
    file_name = input("Enter the name of the file containing the data: ")
    pairs, x, y = load_data(file_name)
    pos = pairs[pairs[:, 0] > 0]
    A, C = fit_data_to_linear(pos[:, 0], pos[:, 1])
    print("Fitted parameters:", A, C)
    plot_data_and_fit(x, y, A, C)

if __name__ == "__main__":
    main()
```

A.2 Fraunhofer simulations

```
import matplotlib.pyplot as plt
import numpy as np
import math

# Define variables, depending on device geometry
L = 400*10**(-9)
W = 3*10**(-6)

# Constants for 80 nm Nb
phi = 2.067833848*10**(-15)
lam = 39*10**(-9)
z = 125*10**(-9)
Afoc = 2*(W/2-z)**2

# Effective junction lengths
d1 = L + 2*lam
d2 = L + 2*z
d3 = L

# Effective junction areas
A1 = W*d1
A2 = W*d2
A3 = W*d3 + Afoc

# Fraunhofer with d = L + 2lambda
def plot1(x):
    return abs((math.sin(math.pi*x*A1/phi))/((math.pi*x*A1)/phi))
plot1vec = np.vectorize(plot1)

# Fraunhofer with d = L + 2lambda_z
def plot2(x):
    return abs((math.sin(math.pi*x*A2/phi))/((math.pi*x*A2)/phi))
plot2vec = np.vectorize(plot2)

# Fraunhofer with Afoc
def plot3(x):
    return abs((math.sin(math.pi*x*A3/phi))/((math.pi*x*A3)/phi))
plot3vec = np.vectorize(plot3)

# Generating x values
x = np.linspace(-0.03, 0.05, 10000)

# Calculate y-values for all functions
```

```
y1 = plot1vec(x)
y2 = plot2vec(x)
y3 = plot3vec(x)

# Plot all on the same graph
fig, ax = plt.subplots()
ax.plot(x*1000, y1, color="red", label="(1)")
ax.plot(x*1000, y2, color="blue", label="(2)")
ax.plot(x*1000, y3, color="green", label="(3)")

ax.set_title('Simulated Fraunhofer plots for SNS-5 and SNS-6') # Change
                                        this depending on device geometry
ax.set_xlabel('$B_z$ (mT)')
ax.set_ylabel('$I_c/I_c^0$')
ax.set_ylim(0, 1)
ax.set_xlim(-8, 8)
leg = ax.legend(loc=1)
plt.show()
```